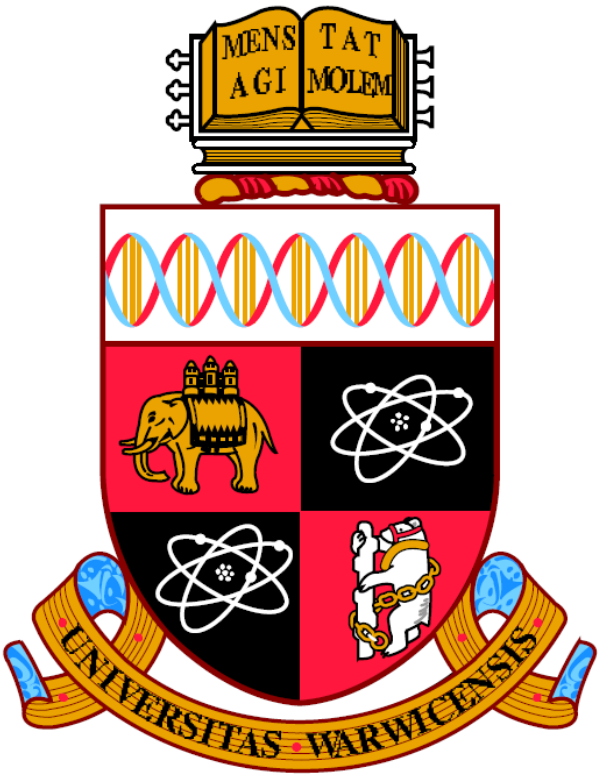

A Multiscale Approach for Fluid Flow Effect on Microstructure and Segregation

by

Arunava SenGupta

Submitted in partial fulfilment of the requirements for the degree of Doctor of Philosophy in Engineering

Warwick Manufacturing Group
University of Warwick
March 2020

WMG
THE UNIVERSITY OF WARWICK

TABLE OF CONTENTS

LIST OF TABLES

LIST OF FIGURES

ACKNOWLEDGEMENTS

Sailing through the journey of doctoral life has been a challenging yet fruitful one and the people who contributed in different phases of the journey deserve special mention. At first, I would like to thank my academic supervisors Dr Michael Auinger and Professor Sridhar Seetharaman for giving me the opportunity to take up this doctoral research with the Steel Processing Research Group at Warwick Manufacturing Group (WMG). I would like to express my sincere gratitude to Dr Michael Auinger for his constant technical advice, endless support and encouragement right from day one till the end of the PhD journey. I took up the challenge of being involved in this research with practically having nil knowledge of modelling. Being new to numerical modelling arena, his continuous guidance in discretizing the bigger problems into smaller ones has been enormous. It is because of him I have developed a sense of confidence in dealing with complex differential equations. His constant guidance in improving the quality of technical publications, thesis and preparing technical presentations has been immense. My sincere thanks to my industrial supervisor Dr Begoña Santillana for her continuous support and guidance in carrying out the experimental investigation during the internship periods I had at Tata Steel Research & Development in IJmuiden, The Netherlands. Her continuous technical advice throughout the journey has been immense. I would like to convey my sincere gratitude to Professor Sridhar Seetharaman (a full time Professor at Colorado School of Mines, USA) for giving his time (through skype-meetings, teleconferencing and email discussions) in providing critical technical advice, immense support and encouragement especially in writing the technical publications. I would like to thank my academic supervisor Professor Peter J. Thomas of School of Engineering for scientific discussions during the final stage of the research and allowing me to attend lectures on fundamentals of fluid mechanics module. I would also like to thank Dr Yongmann Chung of School of Engineering for allowing me to attend lectures on computational fluid dynamics module. I would like to gratefully acknowledge the use of High Performance Computing Cluster available with the Centre for Scientific Computing (CSC) at University of Warwick.

I would like to thank Tata Steel UK Limited and University of Warwick for funding my PhD project. Thanks to Olaf de Ruyter and Sarah Koelman of Tata Steel in

IJmuiden, The Netherlands for helping with all the important administrative formalities related to the internship periods that I had at the IJmuiden Technology Centre (IJTC). I am also thankful to Menno Effern for carrying out the wedge mould casting experiments. I would like to thank Ergun Dogan, Wouter de Bruijn, and Tu Phan-Tran for their help in preparing the samples for metallographic examination, in using the microscopy lab and for the etching experiments. Thanks to Dr Kateryna Hechu for help with the etching experiments and optical microscopy of the samples. I am grateful to Marco Rijnders for carrying out the line scanning measurements of steel slab and wedge mould samples. My sincere thanks to Dr Daniel van Odyck for the modelling related discussions we had and help in retrieving the fluid flow profile data from previous works done at IJTC. I would like to extend my sincere gratitude to Ir Dirk van der Plas in providing critical fluid flow related technical input. Thanks to Dr Rudi Kalter for visit to the Direct Sheet Plant (DSP) and water modelling lab facilities at IJmuiden. Thanks to Dr Stephen Carless and Frank Schrama for the help in getting the process parameters of the collected steel slab samples. Thanks to rest of the colleagues of Steelmaking and Casting Research Group as well as the Process Modelling and Fluid Dynamics Research Group at IJTC for making my stay a memorable one during the internship periods.

I would like to thank Dr Shiv Kumar Choudhary of Steelmaking and Casting Research Group of Research & Development Division of Tata Steel Ltd., Jamshedpur, India in providing a hands-on experience with the metallurgical research work during the initial few years of my career that helped in creating the platform to undertake this doctoral degree. I would also like to thank Dr Suvankar Ganguly and my colleagues of Steelmaking and Casting Research Group in motivating me to undertake this doctoral research. I would like to thank Dr Debashish Bhattacharjee, Suresh Dutt Tripathi, Dr Sanjay Chandra, rest of the study leave committee members and the Human Resource team of Tata Steel Ltd., for the help in the approval of my study leave application which allowed me to undertake the doctoral programme while being an employee of the organisation.

A big thanks to Dr Carl Slater, Dr Stephen Spooner, Will Jacobs, Antonia Betzou, Jack Isaacs, James Whiston and rest of my colleagues of the Steel Processing Research Group, WMG for all the discussions we had during these four years and making my journey a memorable one at the university.

Keeping myself engaged in sporting activities has been an inherent quality from childhood. Nothing has changed in this part of the journey. Sporting activities helped me to focus on the research with renewed vigour. Thanks to the excellent facilities provided by the Warwick Sports Centre at the university that kept me engaged in various sporting activities. A big thanks to Nithin Madhav and Romeo Malik with whom I initially started playing badminton in October 2015. Thanks to Anand Mohan, Dr Ashwin Rajan, Sumit Sinha, James Mathew, Dr Anup Barai, Upender Rao Koleti, Dr Prakash Srirangam, Muinuddin Maharun, Joko Triwibowo, Rakesh Murali for all the fun we had in the badminton sessions. Thanks to Christopher Wood, Dean Mcllwraith, Ilyas Chatta and rest of the members of the ITS Cricket Club and the University Staff & Post Graduate team with whom I played a number of cricket matches over the summer. Thanks to Graeme Knowles for allowing me to represent WMG in inter departmental tournament every year and winning the tri-series cup in 2018 for WMG has been a real privilege. A big thanks to James Mathew for introducing me to Joe Taylor of Claverdon Cricket Club. Thanks to all the members of Claverdon Cricket Club for selecting me to play for the 1st XI team of the club at the Cotswold Hills League 4th Division Level. Playing cricket in English summer in these four years had been a lifetime experience for me. This will be in my memories to cherish for years to come. I would also like to thank Yashraj Tripathy, Anubhav Singh, Dr Arnab Palit, Dr Abhishek Das, Jayendra Bhalodiya, Manoj Babu, Sisir Dhara, Sanghamitra Moharana and Bharath Bandi for all the fun we had during our out of office hour's meetings, birthday celebrations and making me feel at home away from home. Numerous trips with Romeo Malik, James Mathew and Dr Ashwin Rajan allowed me to enjoy the beautiful landscapes across various parts of the country.

Lastly, I would like to thank my family members, who has always been supportive of me. Special thanks to my parents – maa (Zinnia SenGupta) and baba (Dr Amitava SenGupta, who left for the heavenly abode on 15th December 2018) for the unconditional sacrifices and tireless struggle they made throughout their life in nurturing me. It has always been their wish that I pursue higher studies from abroad. Their continued support, love and constant encouragement motivated me in converting their wish into reality. My deepest gratitude to my grandmother Kalpana DuttaGupta and to my uncles, aunties, cousins. All, thank you so much!

DECLARATION

I, Arunava SenGupta, hereby confirm that the work presented in this thesis has been solely undertaken by me, except where otherwise stated. This thesis has been written and compiled by myself. It has not been submitted elsewhere in support of a degree at another university. The presentation of the thesis has been done in accordance with the regulations of the University of Warwick.

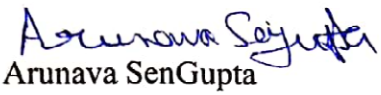

Arunava SenGupta

March 2020.

PUBLISHED WORK

[1] A. SenGupta, B. Santillana, S. Sridhar, M. Auinger, Dendrite growth direction measurements: understanding the solute advancement in continuous casting of steel, IOP Conf. Series: Materials Science and Engineering 529 (2019) 012065, doi:10.1088/1757-899X/529/1/012065.

[2] A. SenGupta, B. Santillana, S. Sridhar, M. Auinger, Transient Effect of Fluid Flow on Dendrite Growth Direction in Binary Fe-C Alloys Using Phase Field in OpenFOAM, JOM, Vol. 71, No. 11 (2019), 3876 – 3884, https://doi.org/10.1007/s11837-019-03730-2.

CONFERENCE PROCEEDINGS

[1] A. SenGupta, S. Sridhar, M. Auinger, Phase-Field Based Solidification Model For Binary Alloy In OpenFOAM in 9th European Continuous Casting Conference Proceedings – ECCC 2017.

ABSTRACT

Maintaining competitiveness in steel manufacturing requires improving process efficiency and production volume whilst enhancing product quality and performance. This is particularly demanding for producing value-added advanced steel grades. In today's world of high quality steels, cast in near net shape where the ability to control microstructure through thermo-mechanical processes is limited, understanding of the dependence of the solidification structure on the process parameters like fluid flow is of technical importance. Variations of phase evolution across different length scales during solidification resulting from a continuous casting process define the macrosegregation (at the scale of casting) and hence the final properties of the solid steel. Macro scale (10^{0} to 10^{-3} m) fluid flow during continuous casting washes away the rejected solute ahead of the micro scale (10^{-6} to 10^{-5} m) solid/liquid interface giving rise to different undercooling levels at different positions of the moving solidification front. With the progress of solidification, the intensity of the washing effect will decrease and the influence of diffusion will come into play, thereby contributing to the macro scale solute profile. Understanding the competition between the crystallographic growth direction and solute transport with casting parameters during the progress of casting will provide an important perspective towards reducing the macrosegregation in the cast product. Stringent quality requirements for the present generation steel grades for automotive applications demand more information into the growing micro scale solute profile mechanism and how it relates to the phenomenon occurring at the macro scale. In order to address the translation of micro scale information into the macro scale, a combined theoretical and experimental approach had been undertaken.

Starting with a single component system, open source phase-field method based solidification model coupled with fluid flow have been developed. Quantitative validation of the solidification model for single component system with experimental results in literature have been done. The developed micro scale model in presence of fluid flow gives an account of the preferred solid/liquid interface growth direction. At different degrees of undercooling, the model predicts the transient nature of the evolving solute profile. The effects of flow velocity and dendrite growth speed on the interface growth direction were separated. Improved theoretical formulations for estimation of the bending angle (defined as deviation from the original growth direction of primary dendrite in absence of fluid flow) were put forward which extends the current knowledge available from literature.

On the experimental part, dendrite bending angle measurements were made in the industrial steel slab samples from a conventional slab caster at Tata Steel in IJmuiden, The Netherlands. The dendrites were found to undergo a change in the growth direction indicating the transition in the fluid flow profile occurring within the mould. Also, the magnitude of the bending angle was found to decrease away from the slab surface. Through the proposed approach of micro-macro coupling an attempt was made to correlate the macro scale fluid flow profile within the continuous casting mould with that of the developed micro scale bending angle formulation. The proposed formulation based on the anisotropy in solid/liquid interface energy was found to fit the experimental deflection angles better than the few available empirical correlations in literature. Line scanning measurements were performed to determine the composition profile of industrial slab samples proving the influence of fluid flow on macrosegregation.

NOMENCLATURE

Symbols	Definition
θ	Deflection angle, *degrees*
$\vec{V}$	Liquid velocity, ms^{-1}
$v_{solidification}$	Solidification rate, cms^{-1}
Fe-C	Iron-Carbon
T_m	Melting point, *K*
σ	Interface energy, Jm^{-2}
C_0	Nominal/initial composition, *mole fraction*
T_L	Liquidus temperature, *K*
$C_S{}^*$ *or* C_S	Solid-phase composition at the interface, *mole fraction*
$C_L{}^*$ *or* C_L	Liquid-phase composition at the interface, *mole fraction*
k^{eq}	Equilibrium distribution/partitioning coefficient
δ	Boundary layer thickness, *m*
k_{effec}	Effective distribution/partitioning coefficient
G_L	Thermal gradient, Kcm^{-1}
v_{tip}	Interface growth speed, ms^{-1}
δ_ε	Anisotropy constant
t_f	Local solidification time, *seconds or minutes*
Mn	Manganese
C_{max}	Maximum concentration
C_{min}	Minimum concentration
ρ	Density, kgm^{-3}
η	Dynamic viscosity, $kgm^{-1}s^{-1}$
P	Pressure, Nm^{-2}
t	Time, *seconds or minutes*
ϕ	Phase-field variable
2λ	Interface thickness, *m*
ε	Gradient energy coefficient, $J^{-1/2}m^{-1/2}$
M	Phase field mobility, $m^3s^{-1}J^{-1}$
C	Composition, *mole fraction*

T	Temperature, *K*
W	Excess free energy at the interface, Jm^{-3}
D_T	Thermal diffusivity, m^2s^{-1}
ΔH_m	Latent heat of melting per unit volume, Jm^{-3}
C_p	Material specific heat, $Jm^{-3}K^{-1}$
D_S	Solute diffusivity in solid, m^2s^{-1}
D_L	Solute diffusivity in liquid, m^2s^{-1}
C_S^{eq}	Equilibrium solute compositions of the solid
C_L^{eq}	Equilibrium solute compositions of the liquid
μ	Linear kinetic coefficient, $ms^{-1}K^{-1}$
V_m	Molar volume, m^3mole^{-1}
R	Universal gas constant, $Jmole^{-1}\ K^{-1}$
ν	Kinematic viscosity of liquid steel, m^2s^{-1}
Ni	Nickel
Δt	Time step, *seconds*
Δx	Grid spacing in *x* direction, *m*
S	Solidified steel shell thickness, *mm*
z	Vertical distance from the meniscus along the casting direction, *mm*
v_c	Casting speed, $mmin^{-1}$
k	Solidification coefficient, $mmmin^{-0.5}$

LIST OF ABBREVIATIONS

Abbreviations	Definition
S/L	Solid/Liquid
MICRESS	MICRostructure Evolution Simulation Software
CFD	Computational Fluid Dynamics
OpenFOAM	Open Field Operation and Manipulation
SEN	Submerged Entry Nozzle
CR	Cooling Rate
PDAS	Primary Dendrite Arm Spacing
SDAS	Secondary Dendrite Arm Spacing
EMBR	Electromagnetic Brake
WDS	Wavelength-Dispersive Spectroscopy
SEM	Scanning Electron Microscope
EPMA	Electron Probe Microanalysis
CV	Control Volume
FDM	Finite Difference Method
FVM	Finite Volume Method
LD	Longitudinal Direction
TD	Transverse Direction

CHAPTER 1: INTRODUCTION

In today's world, steel is one of the most widely used materials because of its high strength to weight ratio. Nowadays industrially, it is manufactured through the continuous casting route [1]. Currently, approximately 20 billion tonnes of steel are being used in a wide variety of products [2]. As per the word steel association data, about 86 million tonnes of steel were used for motor vehicles in 2018. Advent of different grades of advanced high strength steels containing wide variety of alloying elements in different proportions enable the auto makers to produce stronger and lighter vehicles with reduced emissions. Continuous casting of steel is a phase transformation process where liquid steel transforms into solid phase in a continuous manner due to cooling. The structure (distribution and morphology of different phases) resulting from continuous casting, including heterogeneities in the steel microstructure, macrosegregation (at the scale of casting) and precipitation of non-metallic particles are important for downstream processes and final product quality. The practice of continuously cast near net shape [3] profiles (direct hot-charging, thin slab casting and strip casting) has gained in popularity due to energy savings. But these processes limit (or entirely eliminate) the subsequent in-line thermo-mechanical processing possibilities and therefore, the need to control the cast microstructure becomes vital. The microstructure and hence the segregation (non-uniformity in chemical composition) depends on, the alloy chemistry and conditions in the continuous casting mould, primarily the thermal profile and fluid flow. Thus the present generation industrial steel grades in continuous casting operation nowadays are more critical due to macrosegregation. In order to understand the relationship, and identify the operating conditions that control the evolution of the solidification structure, joint efforts both from experimental as well as computational investigations offer ways for in-depth understanding of the continuous casting process and identify sensitivities to distinct process conditions.

1.1 MOTIVATION

Few studies have been performed on commercial grade steels [4], but a clear link between the phenomenon happening on the micro level (dendrite evolution) and the concentration distribution in macro scale [5] is still missing. Arnberg et al. [6] showed that the mesoscopic variation in the solute field in the liquid ahead of the dendrites promotes local destabilization of the solute boundary layer due to flow within the inter-dendritic region. It thus causes the different dendrite tips to grow with different velocities. But on the macro scale and in presence of bulk fluid flow in the continuous casting process, this flow will be at the micro scale. This flow within the inter-dendritic region is slower, compared to that of the bulk flow, which in continuous casting may be strong enough to wash away most of the solutes until a certain degree of solidification has taken place.

It has been reported that in presence of bulk fluid flow, the dendrites during solidification tend to grow in an inclined fashion [7] towards the upstream direction (i.e. towards the inflow direction) due to higher thermodynamic driving force. For multi-component systems, fluid flow around the dendrite tip creates the asymmetric solute profile and hence leads to biased growth of columnar dendrites [8,9] in the upstream direction. Phase-diagrams [10] state that solute rejection during solidification leads to local change in solidification temperature ahead of the dendrite tip and hence affects its growth speed. Incoming bulk fluid flow (macro fluid flow) during continuous casting has a washing effect on the rejected solute in front of the tip thereby altering the degree of undercooling. Also, the flow field (micro scale flow) in between the growing dendrites may have an additional effect. Thus it is the complicated interaction between either types of the fluid flow or their combination and the growth speed of the tip that determines the prevailing conditions ahead of the tip and hence its growth direction.

To the best of our knowledge, the quantitative dependence of growth direction of the primary dendrites on the magnitude of the flow velocity and the solidification speed in steel is limited to two previously reported studies [7,9]. The empirical dependency of the primary dendrite deflection on the solidification speed and the bulk flow velocity for steel ingots as deduced by Takahashi et al. [9] is given as

$$\theta = 22.49\vec{V}^{-0.177} \log \frac{\left(0.00372 \times \vec{V}^{2.08}\right)}{v_{solidification}} \quad (1.1)$$

where θ is the deflection angle of dendrites (degrees), $\vec{V}$ is the bulk inlet liquid velocity (cm/s) and $v_{solidification}$ is the solidification rate (cm/s). The dendrite deflection angle increases with increase in flow and decreasing solidification rate. It can be seen from **equation 1.1** that the dendrite bending angle is not mathematically defined for velocities close to zero because of the logarithmic dependence. It means that the application is limited for this particular equation only and not applicable for stagnant conditions. It doesn't reflect accurately the conditions in an industrial caster. Also, the deflection angle can be both positive and negative because of the logarithmic dependence. Conducting experiments on an inclined chill plate with steels of different carbon contents, Esaka et al. [7] modified the empirical correlation of Takahashi et al. [9] by adding a carbon content dependency term but did not incorporate the anisotropy in interface energy. Also, during the continuous casting process, the degree of undercooling and the bulk fluid flow at various positions of the solidification front within the mould changes depending on the process conditions. This different undercooling pattern may give rise to different deflection behavior in combination with the incoming fluid flow. Developing a better theoretical prediction will thus be helpful in understanding the competition between the preferred growth direction of the dendrite tip and the solute transport.

On the basis of continuum thermodynamic principles, the Phase-Field method [11] has received much consideration for simulating the complicated solid/liquid (S/L) interface structure because of its implicit nature of tracking the S/L front via the diffuse interface approach. Based on the multiphase-field theory, MICRostructure Evolution Simulation Software (MICRESS) [4] is a commercial software package which can simulate solidification microstructure in metallurgical systems. However, only few publications were found related to the above package where the effect of bulk fluid flow on the dendrite deflection has been investigated. In commercially available Computational Fluid Dynamics (CFD) software it is not easy to modify the available numerical models. Modelling investigations of the melt convection effect on solidification microstructure [7,9,12–19] based on in-house developed numerical codes have focussed on the influence of inlet flow magnitude on dendrite bending and branching of dendrites. Primarily this is due to the asymmetric solute profile ahead of

the deflected dendrite. But it is the flow velocity near the dendrite tip which causes the dendrites to grow preferentially against the flow direction and is more representative for solute washing than the inlet flow velocity. Open Field Operation and Manipulation (OpenFOAM) [20] is an open source computational software, capable of handling a broad spectrum of partial differential equations. Thereby, developing a Phase-Field method based open source numerical model in OpenFOAM is useful in understanding the dendrite deflection behaviour of Iron-Carbon (Fe-C) alloys under the influence of bulk fluid flow and relate to the solute advancement behaviour. Moreover being open source the fluid flow coupled model can also be used by the wider materials research community in the development of new alloys and may be extended towards different engineering casting conditions to reduce macrosegregation.

1.2 RESEARCH HYPOTHESIS

The growth of a single dendrite is usually defined by diffusion of the elements near the solidification front. However, in continuous casting the macro fluid flow may be strong enough to “wash” the most of the solutes near the dendrite surface away. This leads to a change of the local composition near the dendrite/melt interface (microsegregation) and also affects the thickness of the diffusion zone causing dendrite deflection.

- The main hypothesis is, that there exists a condition during cooling during continuous casting when the solute transport by diffusion will be considerable enough not to be entirely homogenized by bulk fluid flow.

This is of particular importance because when the effect of diffusion surpasses the bulk fluid flow, one solute starts to accumulate in the dendrite growth region and defines both time and position when macrosegregation starts.

1.3 RESEARCH AIM and OBJECTIVES

The present study investigates the effect of the bulk fluid flow on dendritic structure and hence gives an impression about the influence of flow field on the overall microstructure in a solidified steel slab. To the best of knowledge, no freely available software exists, that combines the effect of fluid flow with solidification kinetics that could be applied to the conditions of this industrially highly relevant process.

The objectives are:

- To quantify dendrite deflection as a function of flow velocity and growth speed.
- To build a digital sub-model of the industrial casting process for quick process optimisation.
- To find the transition between diffusion and fluid flow dominance.
- To experimentally evaluate the effect of bulk fluid flow on the macrosegregation.

CHAPTER 2: LITERATURE REVIEW

2.1 CONTINUOUS CASTING of STEEL

Continuous casting of steel is a worldwide adopted energy efficient and economical technology to produce large quantities of semi-finished products like billet (square cross-section), bloom (cross-section greater than billet) or slab (thick/thin depending on the slab thickness, rectangular cross-section) from molten steel in a semi-continuous manner. Casting of billets (< 200 x 200 mm^2) takes place in single piece tubular moulds [21]. The product exiting the billet caster is then rolled to form rails, axles, bars etc. Casting speed of billets lies in the range of 2 – 5 m/min. Bloom casting takes place in four piece plate moulds similar to conventional slab casting process. Other than square cross-section, blooms can have round cross-section as well. The difference in thin slab casting from conventional slab lies in the thickness of the slab and higher casting speed [22] (4 – 10 m/min in thin slab casting). Thin strip casting is one of the near net shape casting technology where strips of thickness 5 – 20 mm or even less can be cast directly using large rotating rolls as mould walls. The casting speed in thin strip casting lies in the range of 10 – 40 m/min and hence the solidification time is very less compared to conventional slab casting process. **Figure 2.1** shows the schematic of the continuous casting process of liquid steel. Chemically homogenized liquid steel (above the liquidus temperature) contained in the ladle flows into the refractory lined buffer vessel, called tundish. Liquid steel at high-velocity [23] then flows into the water-cooled copper mould through argon shrouded submerged entry nozzle (SEN) in a controlled manner – either with a stopper rod or slide gate mechanism [24]. Mould is the heart of the continuous casting process. Argon shrouding protects the liquid steel from oxidation by air in its passage from tundish to mould. The top layer of the liquid steel in mould is covered with a layer of synthetic slag dosed in powdered form which is a combination of refractory oxides. This synthetic slag is called mould flux. The primary heat extraction from the liquid steel during solidification takes place inside the water-cooled copper mould which is generally 800 – 900 mm long for conventional slab casting. The distance between the copper plates of the oscillating mould can be adjusted, depending on the required width of the semi-finished product to be produced. Thin shell of solidified steel formed

at the upper portion of the mould (called meniscus) thickens continuously as the semi-solid product is pulled downwards at a constant rate. The primary objective of using mould flux [25] is to provide lubrication and horizontal heat transfer between the mould wall and the solidified thin steel shell. In addition to that, mould flux also serves the functions of vertical heat extraction and inclusion absorption from liquid steel. The semi-solid product exits from the mould when the solidified shell is sufficiently thick enough to sustain the ferro-static pressure of the liquid in the core. The thin shell at the mould exit if not strong enough may lead to sudden rupture of the shell. If this shell burst open after the mould exit, then it is called break-out. Liquid steel from the core after tearing the shell will directly come out and the casting process has to be stopped immediately.

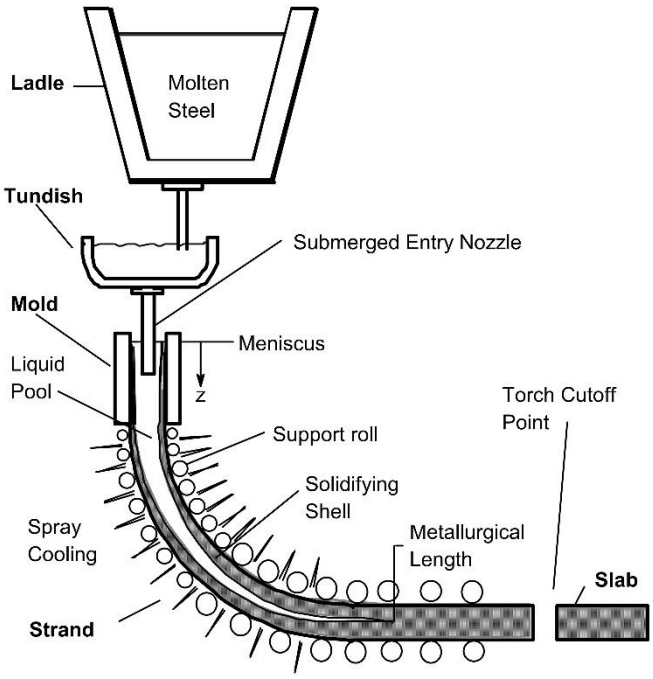

Figure 2.1: Schematic of continuous casting process of steel [1].

The secondary cooling zone which starts after the mould exit plays an important role in further cooling of the semi-solid product. The support rolls withdraw the product from the mould exit at a controlled speed and helps in bending as well as straightening of the solidifying strand. The strand surface is further cooled by either water sprays only or mixture of water and air. At the metallurgical length (the point of complete

solidification), the slab is generally torch cut as per the desired length of the product application. The thickness of the slabs produced may be 200 – 250 mm or even more (for thick slabs) and 50 – 70 mm (for thin slabs). The cast product exiting from the secondary cooling zone is then subsequently used for further downstream processes as per the customer needs. The width of the slabs may vary from 1100 to 1500 mm or even more depending on the customer requirement and so the thickness of the slabs. The surface quality and internal soundness of the cast product depends on how the solidification process is controlled within the mould and thereafter in the secondary cooling zone.

Typical casting defects [22] include internal cracks, surface cracks, porosity, macrosegregation and so on. Some variants of internal cracks include mid-face cracks, off-corner cracks, and centreline cracks. Internal cracks are mainly due to low ductility in high temperature range during solidification. Surface cracks [25] include longitudinal cracking (due to volumetric shrinkage), and transverse cracking. Porosity can happen due to entrapped gas bubbles inside the liquid melt which during solidification try to come out.

2.2 FLUID FLOW and HEAT TRANSFER

Figure 2.2 shows the schematic of the fluid flow taking place inside the continuous casting mould. The mould is filled with liquid steel with a refractory tube called SEN nozzle. Liquid steel enters into the mould through the port of the SEN nozzle. The distance between the steel/slag interface at the mould top and the top surface of the port is defined as the submergence depth. Liquid steel enters the mould with a certain degree of superheat (defined as the extra temperature in degrees above the liquidus temperature to avoid freezing of liquid steel during processing). Flow pattern within the mould depends on the nozzle design parameters like – nozzle diameter, number of ports (one/two/four), port height, port width, submergence depth and so on. Some ports are so designed to have a certain degree of inclination with respect to the meniscus promoting an inclined flow within the mould. So port angle also has an effect on the flow pattern. These nozzle design parameters depends on the caster requirement to the meet the product specification. Too high submergence depth may promote

deeper penetration of the liquid jet in the downward direction thereby delaying the process of complete solidification of the liquid core.

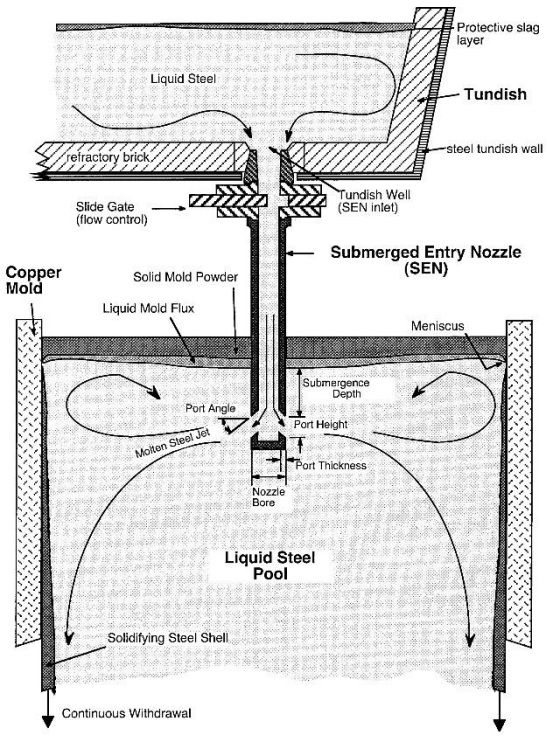

Figure 2.2: Schematic of the fluid flow inside the continuous casting mould [23].

In general, during slab casting, liquid steel after exiting the nozzle travels longer distance along the width direction than the thickness direction and hits the narrow face mould walls. The velocity of the liquid steel at the SEN outlet depends on the desired casting speed of the material being cast – higher casting speed means higher inlet velocity of liquid steel. Fluid flow also depends on the mould geometry like mould width, mould thickness, amount of gas injection, electromagnetic forces [26] and so on. Higher casting speed, shallow submergence depth may give rise to meniscus turbulence. One of the important phenomenon is the turbulent fluid flow behavior within mould due to the incoming jet. Typically the casting speed in the conventional slab casting is around 1 – 2 m/min whereas in the thin slab casting the casting speed is around 4 – 10 m/min [27]. Thus the magnitude of bulk flow velocity is more in thin slab casting than conventional thick slab casting. Because of its transient nature, the fluid flow pattern can oscillate with time depending on the casting parameters and is

one of the most important factors which govern heat and mass transfer thereby having a direct influence on the final product quality. The fluid flow inside the mould may have separate recirculation zones of high velocity as well as low velocity or the flow can be asymmetric which may cause non-uniform heat transfer, entrapment of inclusions, mould powder [25], gas bubbles giving rise to surface inhomogeneities, uneven shell or macrosegregation in the cast product.

Liquid steel after entering the mould quickly dissipates the superheat to the shell. The primary modes of heat transfer within the mould involve conduction through the mould walls and forced/bulk convection due to the incoming liquid stream. Fluid flow and thermal transport are interrelated during the casting process. While heat conduction in solid is a slow process whereas heat transfer in liquid is greatly affected by the convection induced by the highly turbulent flow occurring inside the mould. The heat transfer [28] from the shell surface to the cooling water through the mould is governed by several resistances – mould slag layer, air gap (if any), mould material and the water flowing within the mould. The main process parameters that control the heat transfer behavior within the mould include – shell thickness, mould taper, caster type, casting speed, liquid steel chemistry [29], superheat, water flow rate, lubricant type and so on. The average shell cooling rate (CR) in a slab caster is around 12 °C/s whereas in thin slab caster [27] it is around 50 °C/s. In the upper part of the secondary cooling zone, mainly forced convection by sprays control the heat transfer behavior while in the lower part, the controlling modes of heat transfer involve radiation and conduction. Thus to minimize the degree of inhomogeneity, it is a highly challenging job for a casting operator to control these many number of process parameters. But before controlling these parameters, one needs to understand how each of these parameters affect the flow behavior within the mould and hence the product quality.

2.3 SOLIDIFICATION

2.3.1 Single Component System

Solidification within the mould starts from the meniscus region primarily due to heat transfer through the mould walls. Solidification is a phase transformation process in which the liquid phase gets converted into solid phase by heat extraction. This occurs in accordance with the principle of Gibbs free energy minimization [30] of the process. Solidification at first involves removal of sensible heat from liquid steel and then the latent heat to convert it into solid phase. Solidification of a single component system takes place at a constant temperature called the melting point (T_m). Above this temperature, the liquid phase is thermodynamically stable and below the temperature the stable phase is solid. Both the phases coexist at the equilibrium melting temperature. During the process of solidification, this temperature remains constant until the latent heat is completely removed. On cooling below the melting point, due to its lower free energy nucleation of stable solid phase within the melt starts. This nucleation may happen immediately below the melting temperature or few degrees below the melting temperature. For the latter, even below the melting point if the liquid phase continues to cool it is said to be in a state of being undercooled or supercooled. Formation of nuclei means creation of an interface between solid and liquid associated with an interface energy σ (J/m^2). Thus to create that surface additional energy is required and hence melting generally starts a little below the equilibrium temperature. In order for the nucleation to happen, the total surface free energy of the system has to be a minimum. The equilibrium shape for the nuclei is spherical if the assumed interface energy is same everywhere around the surface, i.e., isotropic. The interface energy can be a function of crystallographic orientation, i.e., interface energy can be higher along one crystallographic direction and lower in another crystallographic direction. This is the case of anisotropic interface energy. In most of the cases, the system has to overcome an activation energy barrier in order to have a stable nuclei. Once the stable solid nuclei has formed, atoms continue to get attach to the stable nuclei which then keeps on increasing in size. On further lowering of temperature, the sensible heat of the solid phase gets reduced. Thus for single component system, solidification is purely a thermally activated phenomenon. It is a diffusional

phenomenon the rate of which depends on the how fast the temperature diffuses away from the moving S/L interface. Higher the degree of undercooling, higher will be the driving force for solidification.

In solids, the atoms are orderly arranged at specific lattice points as compared to that in liquids. In **Figure 2.3a** one can see that the S/L interface is spread over few atomic layers which can be called as a diffuse interface. The broken line shows the width of the interface. The properties of the atoms within the interface vary in a gradual manner between the properties of liquid and solid respectively. **Figure 2.3c** shows that in an atomically flat interface, the liquid to solid transition takes place in a sharp manner. The growth during solidification occurs by the forward propagation of this S/L interface as more and more atoms get attached to the interface. This occurs when the rate of atoms moving from liquid side to solid side is more than that of the atoms moving from solid side to liquid side of the interface. During the interface movement, it is assumed that the liquid and solid phases are at equilibrium at the interface. The thermal gradients in the solid and liquid phases may be different but the energy barrier for atom transport across the interface is negligible. Higher the driving force, higher will be the growth rate of the interface.

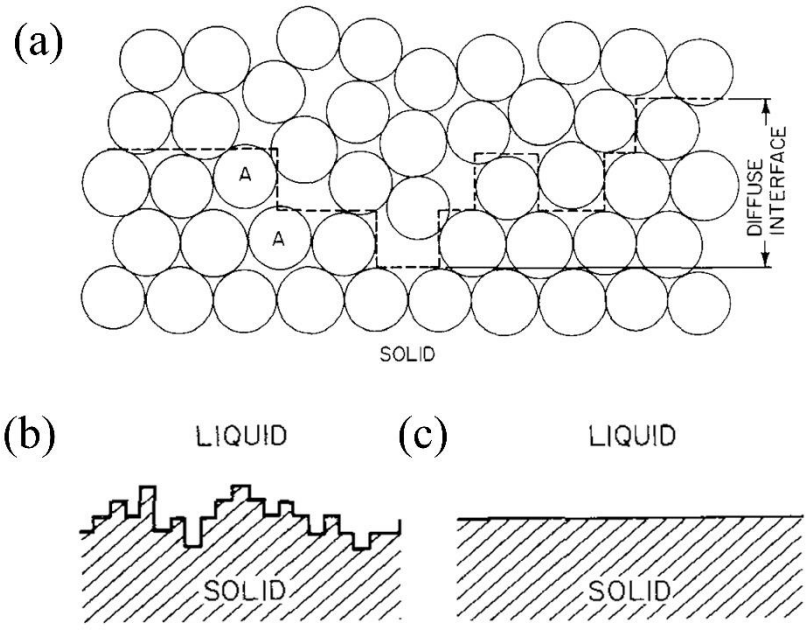

Figure 2.3: Types of interface; (a) atom packing in a diffuse interface; (b) schematic of a diffuse interface; (c) atomically flat interface [30].

2.3.2 Two Component (binary) System

In case of system with two components (binary alloy), the thermodynamics of solidification is also dependent on the composition. The component present in smaller amount is called the solute and the one present in larger proportion is called the solvent. **Figure 2.4** shows the solidification of an alloy with an initial composition of C_0. The solidification starts at temperature T_L (liquidus temperature) above which only liquid phase is stable. The region denoted by "a" is the pure solid region i.e. pure solid phase is stable. At an intermediate temperature T^*, the equilibrium phase diagram (**Figure 2.4a**) states that the respective solid and liquid compositions at the interface are $C_S{}^*$ (on solidus line) and $C_L{}^*$ (on liquidus line) respectively.

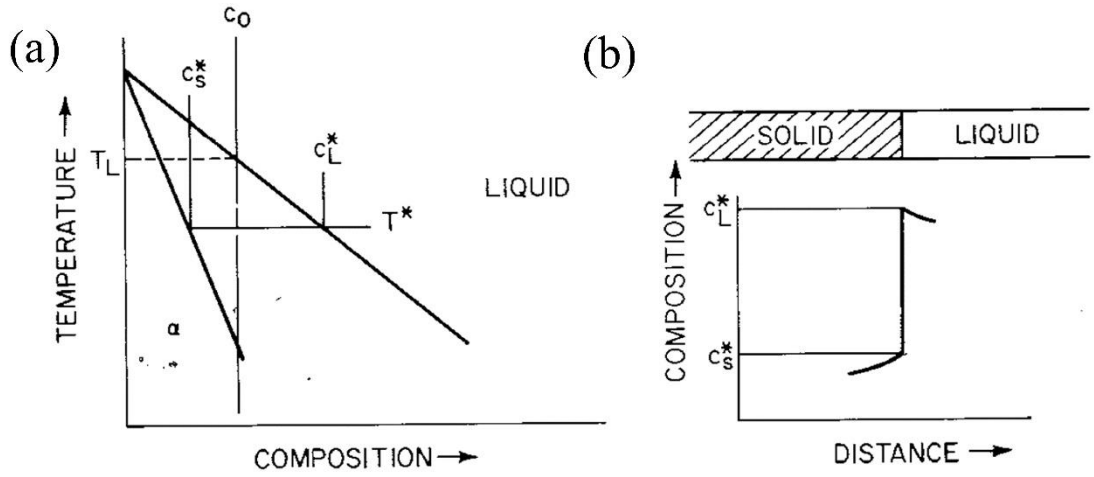

Figure 2.4: Solidification of an alloy with equilibrium at the interface; (a) equilibrium phase-diagram of the alloy; (b) composition profile across the solid/liquid interface [30].

Thus for equilibrium solidification over a range of temperatures, the respective solid and liquid compositions at each temperature are given by solidus and liquidus lines of the phase diagram. The ratio of $C_S{}^*$ to $C_L{}^*$ is called the equilibrium distribution coefficient k^{eq}. **Figure 2.4b** shows that the interface between the solid and liquid phases is planar. In general, during the process of solidification, the growing solid continues to reject the excess solute into the remaining liquid because of its inability

to hold the solute. This excess solute gets piled in front of the interface. The solid which forms from this solute-enriched liquid also gets richer in solute with the progress of solidification. This is the phenomenon of solute redistribution which takes place during solidification only. Thus the equilibrium liquid composition C_L^* is greater than the equilibrium solid composition C_S^* as shown in the **Figure 2.4b**. Also from **Figure 2.4a**, it can be seen that the liquidus and solidus lines have been assumed to have a downward slope. Another important assumption for equilibrium solidification is complete diffusion in liquid and solid. That is why the solidifying material is homogeneous after complete solidification in spite of solute redistribution phenomenon. Generally, the bulk mixing in liquid takes place at a much faster rate than that in the solid because of higher diffusivity of the solute element in the liquid phase. For the case of no solid diffusion and limited diffusion in liquid [30,31], the solute rejected into the liquid will take a longer time (assuming no convection) to mix compared to the case of complete diffusion in liquid. This will give rise to the formation of a solute diffusion boundary layer. At steady-state [30,32] the solute profile ahead of the interface will be similar to that shown in **Figure 2.5a**. In this case, also the interface is assumed to be at equilibrium.

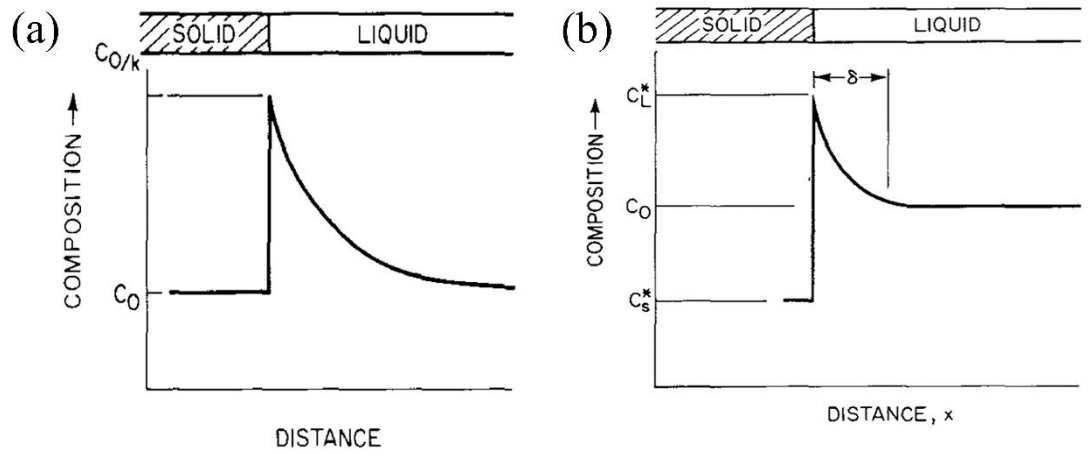

Figure 2.5: Formation of solute boundary layer; (a) solute distribution for steady-state solidification [30]; (b) solute profile for solidification with convection in liquid [30].

Further away from the interface (at infinite distance), the composition in the liquid decays in an exponential manner until it reaches the alloy composition C_0. The

distance over which this decay in composition occurs is called the solute boundary layer, the thickness of which depends on the liquid diffusion coefficient and the interface growth speed.

In cases of solidification where there is bulk fluid flow, the assumption of nil convection in full liquid region is not valid. In this case, outside the diffuse boundary layer, the liquid composition is always maintained at the initial alloy composition level by convection [30]. It can be seen from **Figure 2.5b** that at steady state the liquid composition at the interface is C_L^* while the solid composition is C_S^*. The liquid composition outside the diffusion boundary layer thickness is same as the initial alloy composition C_0. It is be noted that **Figure 2.5a** and **Figure 2.5b** are not identical. The difference lies in the distance at which the liquid composition becomes equal to the alloy composition. In **Figure 2.5a**, it occurs at infinite distance away from the interface while in presence of convection in liquid, the liquid composition becomes equal to the alloy composition at a distance "δ" from the interface as shown in **Figure 2.5b**. The assumption is that the boundary layer thickness "δ" is small compared to the length of the container in which the solidification is taking place. Hence in this case of bulk convection, the partition coefficient gets modified as effective partition coefficient [33] (k_{effec}) which is different from that of equilibrium partitioning coefficient (k^{eq}). Till this point, the interface during the solidification has been shown as a planar one.

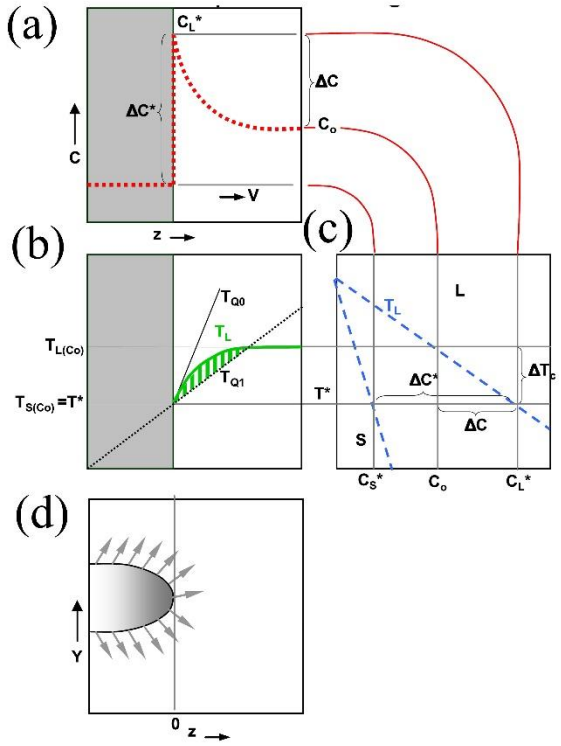

Figure 2.6: Phenomenon of constitutional supercooling in binary alloy solidification [30,34,35].

Figure 2.6 (a - d) shows the phenomenon of constitutional undercooling occurs during alloy solidification. **Figure 2.6d** shows a solid growing into a liquid during solidification. The arrows at the interface mark the direction of solute rejection into the liquid. The green line in front of the interface in **Figure 2.6b** shows that the equilibrium liquidus temperature increases as one move away from the interface ($z = 0$). This is because the solute content is highest at the interface and then decreases away from the interface (as per the phase-diagram shown in **Figure 2.6c**). Let T_{Q0} and T_{Q1} be two different thermal profiles in the liquid phase in **Figure 2.6b**. The S/L interface ($z = 0$) is at the equilibrium liquidus temperature ($= T^*$) in **Figure 2.6b**. When the thermal profile is T_{Q0} along with the liquidus profile of T_L, then the interface is at the equilibrium liquidus temperature and every point ahead of the interface is above the liquidus temperature. This is the condition of stable planar front solidification. If by any chance (may be due to some instability phenomenon) there is formation of a protrusion on the planar interface, it will quickly melt since it will find itself in a superheated zone where the temperature is greater than the equilibrium liquidus temperature. Thus the protrusion will melt back. When the thermal profile is T_{Q1} along

with the liquidus profile of T_L, then every point in front of the interface is below the liquidus temperature. The liquid is thus in an undercooled state and this undercooling arises due to change in composition and not due to temperature (which happens in single component system). This results in the instability of the planar front and if any protrusion forms it will find itself in undercooled state, i.e., at a temperature lower than the equilibrium liquidus temperature. Thus it will become stable and continue to grow. This phenomenon is called "constitutional undercooling". Occurrence of this phenomenon happens when the ratio of actual thermal gradient (G_L) to interface growth speed (v_{tip}) decreases below a critical level as shown in [30].

2.3.3 Solidification Microstructure

Next part of the story is how fast or slow the protruded part grows. Constitutional undercooling tends to make the interface unstable from planar to curved interface (thus to cellular/dendrite) while due to interfacial tension the interface tends to reduce the curvature to reduce total energy. Mullins and Sekerka [36–38] in their analysis of interface stability considered sinusoidal perturbations in front of the interface. **Figure 2.7a** shows the growth of a cell growing opposite to the heat flow direction with its tip having a rounded type of curvature. Crystallographic effects of preferred orientation comes into play when the (G_L /v_{tip}) ratio decreases further i.e. the growth speed of the interface increases. As the growth speed increases further, the growing crystals tend to orient themselves more in the direction of preferred growth direction (<100> for cubic metals) and the tip of interface tends to become pointed. Also, perpendicular to the primary growth direction (<100> in **Figure 2.7d**) the interface tends to develop small protrusions as well. Such changes in morphology are shown in **Figure 2.7 (b – d)**. With the further progress of solidification, such serrations perpendicular to the primary growth direction continue to grow ultimately giving rise to a tree-like morphology having a primary trunk (which grows along the heat flow direction) along with secondary branches. Such a morphology is called dendritic structure. Solidification morphology in pure metals is mainly dictated by the thermal gradient which defines the growth rate of the S/L interface. For pure materials, the initial undercooled liquid is in metastable state below the equilibrium melting temperature and is the source of interface instabilities which changes the interface pattern from planar to cellular or dendritic. In alloys, however, the concentration gradient also plays

an important role in addition to thermal gradients in both solid and liquid phases. Solid crystals that start to form during solidification continuously change their concentrations in accordance with the equilibrium phase diagrams, thereby causing a pile-up of the solute at the S/L interface. This changes the concentration gradient that affect the rate of advancement of the interface as well as the solidification morphology. This concentration gradient is also highly affected by the convection existing within the liquid phase.

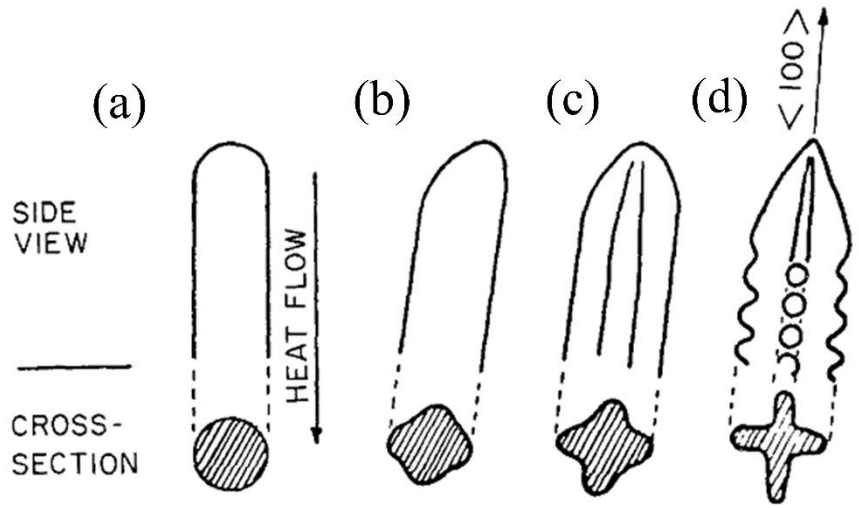

Figure 2.7: Change in growth speed causes change in the crystal growth morphology [39].

If the thermal gradient in the liquid is positive i.e. the latent heat is dissipated through the solid phase, it will result in columnar dendrite as shown in **Figure 2.8**. All the columnar dendrites are oriented in one particular direction. **Figure 2.8** also shows three important length scales of the dendritic solidification structure – tip radius (R, μm), primary dendrite arm spacing (PDAS) (λ_1, μm) and secondary dendrite arm spacing (SDAS) (λ_2, μm). Each of these are affected by the process parameters like undercooling, solute and thermal gradient. In dendritic growth, solute and thermal diffusion control how the latent heat and solute are transported away from the interface. But the problem lies in how to track the interface or the solidification front because the shape of the interface is unknown.

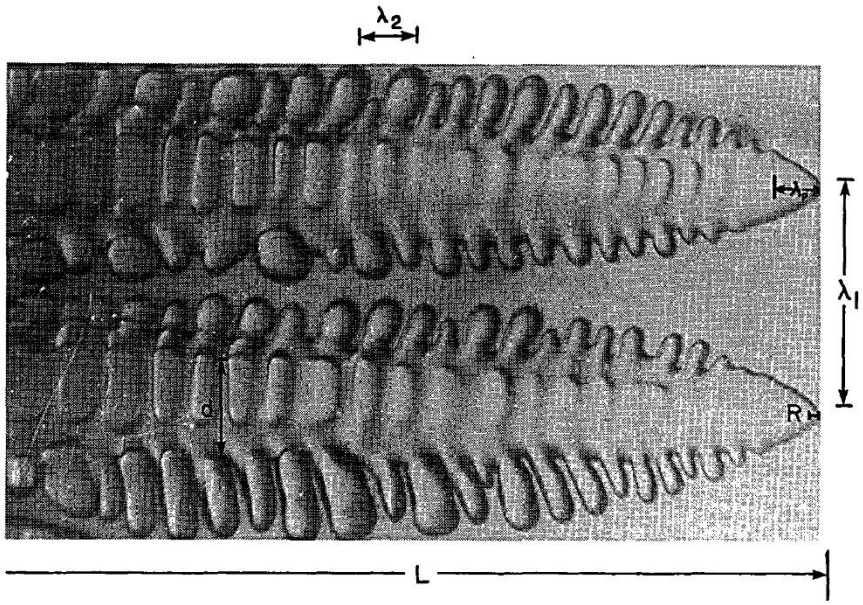

Figure 2.8: Columnar dendrite [40].

Assuming the interface to be of parabolic nature, Ivantsov [41] was the first to develop the differential equation that simultaneously satisfied the thermal diffusion equation and preserved the shape of the dendrite (parabolic) during steady-state growth assuming the interface to be at the equilibrium melting temperature. In a pure undercooled melt, he showed that the tip radius is inversely proportional to the interface speed at a given undercooling. The well-known Gibbs-Thomson relationship [42] states that in order to have a stable curved interface in equilibrium with the melt, the interface will not be at the equilibrium melting temperature (for pure material) but at a temperature lower. For high undercooling condition, the growth theory of the solid crystal is governed by kinetics of the atomic or molecular attachment [43] at the interface as opposed to diffusion limited growth at low undercoolings. For dendrites, the atomic attachment kinetics is weakly dependent on the orientation as opposed to highly anisotropic materials (form faceted dendrites) like semi-conductors. The side-branches arise due to unsteady state nature of the evolution process. Thus understanding the dendritic growth phenomenon requires the knowledge of interfacial phenomenon coupled with the physics of transport theory.

For metals and alloys, the anisotropy in interface energy has important implications on the solidification structure. This anisotropy means that the interface energy is a function of the orientation of the interface normal. The anisotropic interface energy is

characterized by single anisotropy parameters for bcc cubic metals whereas for fcc metals it is characterized by two anisotropy parameters [44]. For cubic structure, the anisotropic interface energy $\sigma(\theta)$ for a four-fold-symmetry in 2D is expressed as $\sigma(\theta) = \sigma(1 + \delta_\varepsilon \cos(4\theta))$ where δ_ε is the anisotropy parameter that defines the strength of the anisotropy.

Figure 2.9 shows three primary dendrites growing from bottom towards the top with all the dendrite arms parallel to each other. The branches growing sideways and perpendicular to the primary arms are secondary dendrite arms. Both primary and secondary arm spacing are functions of the cooling rate. The higher the cooling rate, less will be the arm spacing. In some cases, tertiary arms also may exist. Kinks in the secondary arms shown in **Figure 2.9** may give rise to formation of tertiary arms. The entrapped liquid in between the solidified dendrite arms is called inter-dendritic liquid which is highly enriched with solute elements. The cumulative accumulation of the excess solute in front of the advancing interface, (being a transient process) influences the local undercooling and hence the cooling rate. Rejection of solute during solidification gives rise to segregation in the cast product, which is nothing but a non-uniformity in its local chemical composition. Segregation can be divided into macro / meso / microsegregation. Macrosegregation is the composition inhomogeneity at the scale of casting where as mesosegregation [45] is on the scale of several grains. Microsegregation is the composition inhomogeneity on the scale of dendrites.

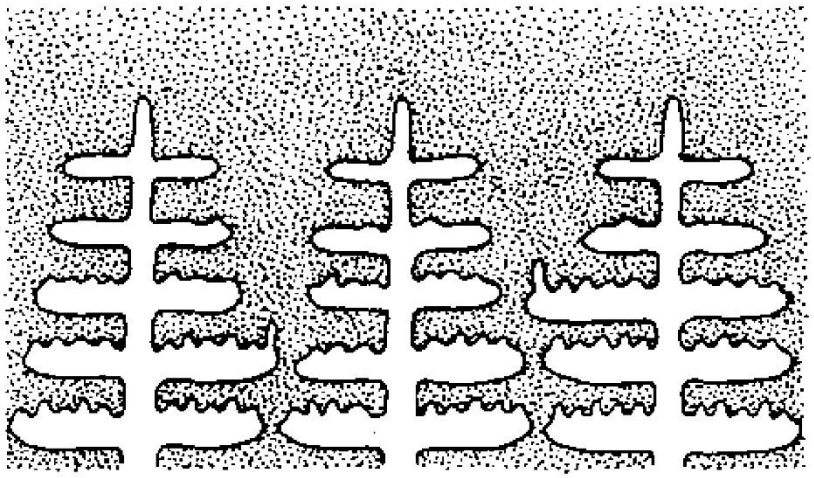

Figure 2.9: Primary and secondary dendrite arms [30].

One of the important parameter in the study of solidification structure is the dendrite arm spacing variation which gives an idea about the change in the cooling rate. The driving force behind this dendrite branching comes from constitutional undercooling existing between the dendrite arms. The arms would tend to branch in a manner to reduce the undercooling. The spacing between the primary dendrite arms depend on the product of thermal gradient and growth rate which has the dimension of cooling rate. Secondary dendrite arm spacing depends on the cooling rate as shown by Suzuki et al. [46]. **Figure 2.10** shows the plot of SDAS with average cooling rate (in ^{o}C/min) for ingot casting of carbon steels with carbon content ranging from 0.14 wt.% - 0.88 wt.%. He obtained a correlation of the form SDAS (in μm) = $710(CR)^{-0.39}$. Another important variable other than the cooling rate is the local solidification time t_f which is also related to SDAS [30]. The expressions for dendrite arm spacing (*DAS*) have the following form [30]:

$$DAS = \left(at_f^n\right) = b \times \left(G_L v_{tip}\right)^{-n} \tag{2.1}$$

where *n* is the exponent. The exponent *n* ranges typically from 0.33 to 0.5 for secondary dendrites and close to 0.5 for primary dendrites. Some of the secondary dendrite arms that form at the beginning of the solidification may get unstable and remelt [30] while others can coalesce and grow with wider dendrite arm spacing compared to that at the initial stage of solidification. The driving force behind this is the surface energy.

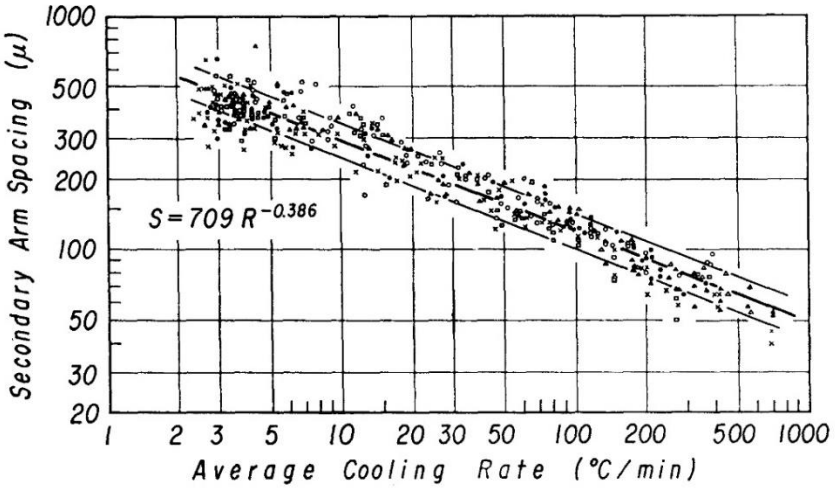

Figure 2.10: Plot of secondary dendrite arm spacing with cooling rate for ingot casting of carbon steels [46].

Kurz [47] and Trivedi [48] developed theoretical relations that showed at high growth rates the primary dendrite arm spacing is a function of Gibbs-Thomson parameter, range of solidification temperature, partitioning coefficient in addition to growth rate and thermal gradient. Based on the published experimental data Thomas et al. [49,50] developed fit correlations with different exponents for estimating primary and secondary dendrite arm spacing as a function of cooling rates and local solidification times for steels with varying carbon contents. Louhenkilipi et al. [51,52] developed model-based equation for estimating the dendrite arm spacing as a function of cooling rates and steel chemistry for continuously cast multi-component steels.

2.3.4 Effect of Fluid Flow on Solidification Microstructure

Bulk fluid flow during alloy solidification washes, to some extent, the rejected solute away (thereby changing the local composition) and will thus define the macrosegregation. This will consequently change the dendrite growth direction [7] and ultimately the evolution of the solidification structure. Takahashi et al. [9] applied the principle of Taylor vortex flow by rotating one of the two concentric cylinders during solidification of carbon steel and Al-Cu alloys [53]. Takahashi et al. [9] showed that with decrease in the solidification rate and velocity increase in the bulk liquid, the solute concentration in the solid decreases. The effective distribution coefficient (k_{effec}) was defined as the ratio of the average solute concentration in the dendrite and the interdendritic region to the solute concentration in the bulk liquid. Takahashi et al. [9] observed that with increase in bulk flow velocity and decrease in the solidification rate, the effective distribution coefficient of each element decreased. Takahashi et al. [9] thus proposed that the segregated solute rich liquid in between the solidified dendrites in the solidifying zone (composed of solid and liquid) must have been washed away due to the liquid flow velocity. This washing effect may take place up to a critical solid fraction. Hence it is possible to understand the extent of macrosegregation during solidification if the bulk flow velocity is known. The effective distribution coefficient can be expressed [9,53] as

$$k_{effec} = 1 - S_p(1 - k^{eq}) \tag{2.2}$$

where S_p is the critical solid fraction. It was also observed that the primary dendrites got deflected towards the upstream direction.

By analysing a continuously cast steel slab Okano et al. [8] found that the deflection angle of the columnar dendrites was large at the edges but decreased towards the slab centre. However, the study did not report the correlation between the deflection angle and compositional analysis. The casting speed of 0.6 m/min was on the lower side and the slab was cast without the influence of electromagnetic brake (EMBR) [54]. Nowadays most of the industrial slab casters are equipped with EMBR, the primary aim of which is to ensure stable and calm fluid flow pattern within the mould and thus can have an effect on the dendrite deflection pattern. The casting process parameters control the fluid flow pattern within the continuous casting mould. Thus predicting the fluid flow transition region (if it exists) within the mould from the experimental dendrite deflection angle can be an useful information for the casting operators as it is still a challenge to experimentally measure the fluid flow pattern in the mould.

Murakami et al. [19,55] did experimental measurements of the deflection angle of the growth directions in the upstream direction as a function of the flow rate and copper content in Al-Cu alloys. They observed that the inclination angle increased with the increase in flow rate. Esaka et al. [7] showed that in low manganese (Mn) steels (0.15 wt.% Mn) the deflection angle of the growing dendrites in a flowing melt increased with the increase in carbon content till 0.1 wt.% C after which the angle remained almost constant. The deflection angle also increased with flow velocity. They also proposed an empirical correlation of deflection angle as a function of carbon content, flow field and growth velocity of the dendrite tip. Lee et al. [13] developed a cellular automaton based continuum model to model the deflection behaviour of dendritic grains in a flowing melt for Al-Cu alloys and experimentally verified through inclined chill plate experiments. Similar to earlier authors [7,9,19,55] they also observed that the deflection angle increased with an increase in the copper content as well as with increasing bulk flow velocity. Forced convection washed away the solute towards the downstream direction thereby promoting the upstream deflection of the dendrites. The growth of the dendrite tip was found to be faster than the growth between dendrites due to a solute depleted liquid ahead of the tip. Thus even if the solute content is lower, the high bulk flow velocity may lead to severe upstream deflection of the dendrites.

Increased fluid flow also has an impact on the dendrite morphology [56]. Also, the angle [15,57] between the melt flow direction and the dendrite growth orientation has an impact on dendrite branching. Most of the research on the effect of flow has been focussed on non-ferrous systems like Nickel (Ni)-Copper (Cu) [15,16], Aluminium (Al)-Silicon (Si) [14,17], Aluminium (Al)-Copper (Cu) [12,13], [58] Lead (Pb)-Tin (Sn), convection in Gallium (Ga)-Indium (In) alloys [59], while a few exists for Fe base alloys like Fe-C [57], Fe-Mn [60] etc. that can improve the understanding of the microstructure formation under industrial conditions. For a Fe-0.15 wt.% C binary alloy in presence of bulk fluid flow at relatively high undercooling condition, Natsume et al. [57] investigated the single dendrite deflection at three different growth speeds by considering the anisotropy in interface energy. Rappaz et al. [61] performed the electron backscatter diffraction (EBSD) characterisation of the solidified columnar grains in the presence of fluid flow in a twin roll caster. Xu et al. [62] studied the effect of liquid flow and superheat on the formation of equiaxed zone in continuously cast low carbon steel slabs (Mn: 1.2 - 1.6 wt.%). They showed that it is the washing effect at the solidification front in the mould that detaches the dendrite arms and leads to the formation of an equiaxed zone. Thus bulk fluid flow can have an influence on the morphology and size distribution of the dendritic growth which in turn can promote macrosegregation thereby effecting the material properties of the final product.

2.3.5 Macrosegregation

Figure 2.11 shows the solidification structure in a cast ingot. When the superheated melt immediately comes in contact with water cooled mould walls, formation of randomly oriented small crystals/grains takes place on the mould walls as shown in **Figure 2.11**. This zone is called “chill zone”. With time, some of the grains tend to move fast perpendicular to the mould walls i.e. along the heat flow direction and overwrite the slow-moving ones giving rise to elongated grains. This zone is called “columnar zone”. Due to high kinetic energy from the melt convection, many of the crystals / grains may get detached from the mould surface and act as heterogeneous nucleation sites within the melt. At the center, one may find cluster of big equiaxed grains. The length of various zones (like chill zone, columnar zone, equiaxed zone), position of the columnar to equiaxed transition (CET) zones depend on the casting process parameters which control the growth rate as well as the thermal and

concentration gradients inside the melt. The elongated columnar grains may impinge upon each other almost near the center of the cast cross-section. Liquid present near the center will be the last to solidify and thus highly enriched in alloy additions, giving rise to centerline macro / microsegregation.

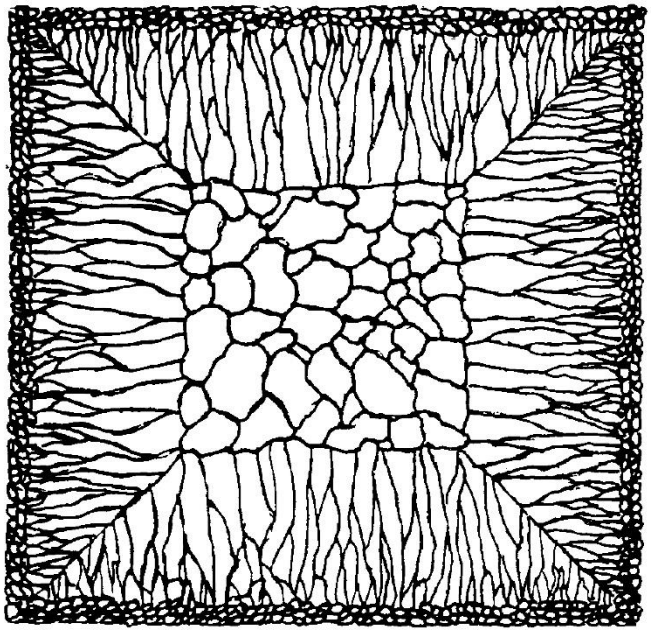

Figure 2.11: Cast structure in a solidified ingot [30].

In continuous casting process, conditions like thermal and concentration gradients, alloy chemistry govern the morphology and the distribution of the growing solid phase. The solidification structure of the cast product is thus directly dependent on the complicated multiscale interaction of heat and mass transfer along with turbulent fluid flow within the mould region. Movement of the solute-enriched liquid during solidification due to the liquid flow in ingot or continuous casting process over large distance is critical for macrosegregation in the cast product. Macrosegregation is difficult to eliminate completely by annealing treatment. Macrosegregation will tend to produce zones of composition which lies outside the specified composition limit of the product and thus leads to their rejection. Hence macrosegregation is considered a defect in the cast product.

Nowadays, product requirements for the automotive industries and the heavy industry sectors like the defence sector are getting more stringent as far as the product quality is concerned. Most of the automotive industries are going for advanced high strength steel grades, which offer unique combination of enhanced formability along with high tensile strength. Due to their enhanced properties, the proportion of usage of such steels are increasing in the current world. The use of advanced high strength steel grades are driven by the low international carbon dioxide (CO_2) emission standards and high safety requirements which demand light weight, yet stable cars. With appropriate manufacturing techniques, these steels have the potential for cost and weight savings with improved crash resistance. The problem with these steels, however lies in the number of constituent elements which define both strength and ductility. Other than iron and carbon they contain a number of alloying elements like manganese, niobium (Nb), titanium (Ti), vanadium (V), aluminium (Al) which are all prone to segregation. These advanced high strength steel grades are more sensitive towards small scale differences in composition. High Mn and Al contents can often lead to macrosegregation [63,64] in TRIP and TWIP steels. Segregation [65] can also lead to formation of undesirable microstructure. Cracking susceptibility during casting can be influenced by microsegregation, localised precipitation and undue phase transformation. Near net shape casting techniques have been proposed for advanced steel grades to circumvent castability issues and achieve an improved as-cast structure and composition. Here, the as-cast properties will more severely influence the properties of the final product.

Solute washing due to bulk fluid flow or internal flows due to shrinkage, natural convection, deformation of solid network (due to thermal stress, liquid melt pressure head) give rise to macrosegregation [66]. In addition to that, there can be flows due to gas bubble formation and electromagnetic forces. The zone where solid and liquid phases coexist is called mushy zone. **Figure 2.12a** shows an ideal liquid steel, mushy zone and solid phase profiles in a continuous casting process as superheated liquid steel is being continuously fed from the top and **Figure 2.12b** shows the schematic of a solidifying mushy zone with a typical bulk fluid flow profile in the liquid phase. In the primary cooling zone, formation of thin solid shell takes place due to heat extraction from the mould walls. In continuous casting of steel, the shell thickness is directly proportional to the square root [28] of the solidification time (given as distance from meniscus divided by the casting speed). As it is being lowered, the shell

continues to thicken while the core is still fully liquid or semi-solid. As soon as it comes in contact with the secondary cooling zone, further cooling takes place due to water spraying. Three distinct zones can be seen – inner fully liquid core, outer solid portion and in-between lies the mushy zone which is a mixture of solid and liquid. As the solidification front moves towards the center, the solute rich liquid ahead of the front being denser flow downwards in the casting direction. The solid fraction changes continuously in the mushy zone and hence the permeability becomes zero when the solid fraction reaches 1. Depending upon the process conditions, the dendrites may be free to flow within the liquid or may form a rigid coherent network. The flow behavior with change in permeability is approximated as per Darcy's Law [67]. Because of the higher density of the free floating dendrites, downward convection of these free-floating dendrites may happen in the central liquid pool due to gravity.

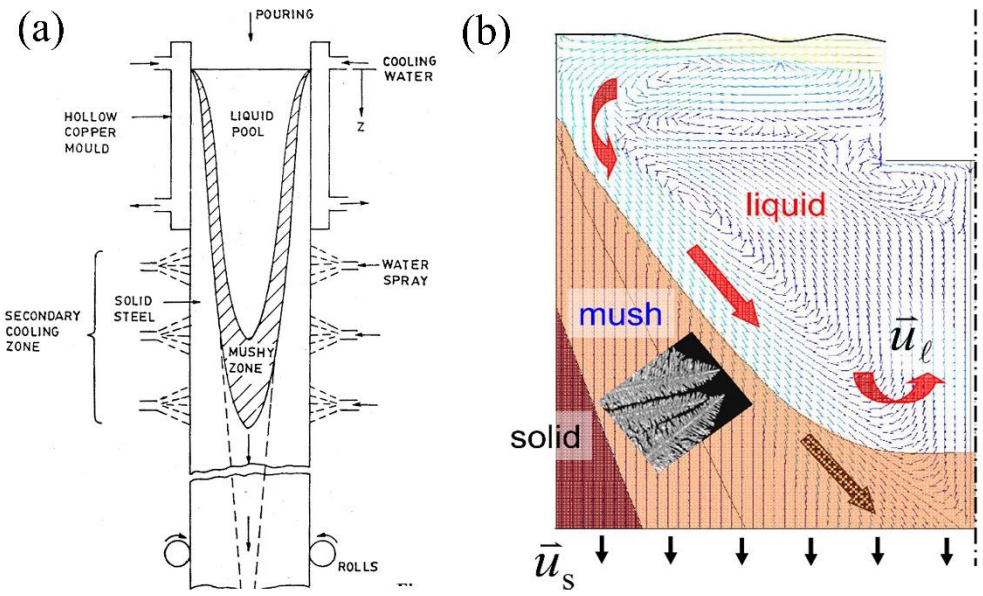

Figure 2.12: Mushy zone profile; (a) in continuous casting of steel [68]; (b) with bulk fluid flow profile [69].

Two important casting process parameters are thermal gradient and the solidification rate. Heat transfer in vertical and horizontal directions govern how the latent heat is removed from the solidification front and thus define the mushy zone thickness. The higher the casting speed, the higher is the heat extraction rate and the lower will be the thickness. Flow occurring within the dendrite arms is called inter-dendritic flow [30]

which is quite similar to flow through porous medium. If the temperature range of solidification is quite large then the width of the mushy zone will vary over large distances. Higher mushy zone width will promote coarsening of the dendritic solidification structure which depends on the local solidification time. Flow due to solidification shrinkage gains importance at a later stage when considerable amount of solid has already formed, i.e., when the permeability decreases to a lower extent. While the solidification front moves inwards towards the centre, liquid flows [70] in the opposite direction to fill up the shrinkage cavities present in the semi-solid mush. Flow from the bulk liquid into the dendritic region causes positive microsegregation at the surface region and negative microsegregation at the centre [22]. The primary cause of this type of inward flow is shrinkage. This type of segregation is called inverse segregation [71]. Similarly outward flow pushes the solute enriched liquid towards central portion. Thus, if the central portion of the cast product has a composition higher than the nominal composition, then it is called centreline positive macro / microsegregation. Process variables which affect the macrosegregation include but are not limited to steel chemistry, casting speed and superheat. Feeding of liquid steel from top helps to fill the cavities with fresh liquid and thus have a tendency to reduce centreline macrosegregation. If the columnar dendrite front progresses steadily towards the centre, giving less chance of feeding the cavities, then the centreline macrosegregation increases. At a particular horizontal level along the cast product, there will be zones which solidify at a very early stage (close to surface or sub-surface) while there will be zones also which solidify at much later stage (close to the central region). Thus the cooling rate decreases from the surface towards the center portion.

Pickering [72] in his review on macrosegregation put forward a schematic of various types of macrosegregation observed in large steel ingots. The factors responsible for each of the mechanisms are a result of complicated interaction between imposed bulk flow, fluid flow due to temperature and concentration difference, solidification shrinkage, flow of equiaxed grains along with casting process parameters, deformation as well as the cast ingot size. Zhi-Ghang Xu et al. [62] found that the segregation ratio away from the slab surface remained almost constant until the slab centre where positive microsegregation was observed in low carbon steel slabs of superheat more than 15°C. The slab macrostructure was found to be columnar whereas the centre line segregation was attributed due to bridging. Similar centerline microsegregation was

observed in low alloy steel slabs by Pikkarainen et al. [73] as well as in high carbon steel slabs by Choudhary et al. [74]. El-bealy [75] explained that the initial fluctuation in the microsegregation levels close to the slab surface is due to the interactions between the strand surface cooling behaviour and the casting process parameters. The segregation ratio was defined as the ratio of the actual measured composition to that of the nominal composition. A maximum segregation ratio of 1.5 was reported by El-bealy [75]. This along with the spary cooling pattern in the secondary cooling zone creates different thermomechanical strain (both tensile and compressive) behaviour on the strand surface thereby affecting the interdendritic fluid flow. This is also known as deformation induced flow because it creates a degree of deformation on the mushy dendrites thereby affecting the macrosegregation. It is the length scale of the transport and the combined effect of the transport due to diffusion and fluid flow that determines the extent of macrosegregation. Thus segregation in solidification will occur inevitably, whereas it is the length scale and the amplitude of segregation that determines the quality of the cast product. The extent of each of the mechanisms mentioned above depend on the material properties and process parameters. Thus the movement of solid and liquid phases play a critical role in governing the macrosegregation in ingots and castings. In a nutshell, solidification in continuous casting is a multifactor dependent transient heat transfer, coupled fluid flow as well as mass transfer phenomena. It is to be noted that the solidification structure is not same as the final microstructure as solid-state phase transformation may alter the original solidification structure.

2.3.6 Methods of Elemental Analysis for Macrosegregation

Methods of quantitative elemental analysis for macrosegregation in steel slabs include [76] wet chemical methods (time consuming), optical emission spectroscopy (OES), wavelength-dispersive X-ray spectroscopy (WDS), energy-dispersive X-ray spectroscopy (EDS), and X-ray fluorescence (XRF). The Optical Emission Spectrometry with Pulse Discrimination Mapping (OES-PDA) [77] is a method by which one can quickly measure the chemical composition of elements across large sections of slab samples in short time. Techniques like scanning electron microscope (SEM) / EDX, Electron probe microanalysis (EPMA)-WDS provide more accurate local quantitative elemental analysis and spatial resolution through line scans and area

maps, but are time-intensive. The energy dispersive X-ray technique in combination with (SEM) is a useful method for compositional analysis of various elements in a sample. But the composition detection limit is restricted up to 0.1 – 0.3 wt.% [78]. EPMA technique [79] with WDS is a powerful technique to identify even the concentration of elements much more accurately because of its 10 times lower detection limit compared to that of SEM / EDX technique. A highly focused electron beam is allowed to incident at the measurement point. The beam then interacts with a small volume of the test material to generate characteristic X-rays (characteristic of each element) along with back-scattered electrons, secondary electrons etc. Apart from the quantitative measurement of the elemental composition, one can also get high-resolution electron images as well as quantification of the phase distribution. Various means of representing macrosegregation [80] include – segregation ratio (C_{max}/C_{min}), degree of segregation ($C_i - C_0$) and relative deviation of the concentration from the average ($(C_i - C_0)/C_0$) where C_{max} and C_{min} are maximum and minimum concentrations and C_i is the composition at a specific location. Line scan measurement in EPMA [81] is the composition profile measured across a specified line with a specific step size. **Figure 2.13** shows a typical centreline macrosegregation of carbon in a continuously cast steel. It can also extend over macroscopic distances in several mm. Miyazawa [82] observed solute enriched region of carbon at the center of a continuously cast steel slab and concluded that it is due to bulging action of the rolls in the secondary cooling zone on the solid shell.

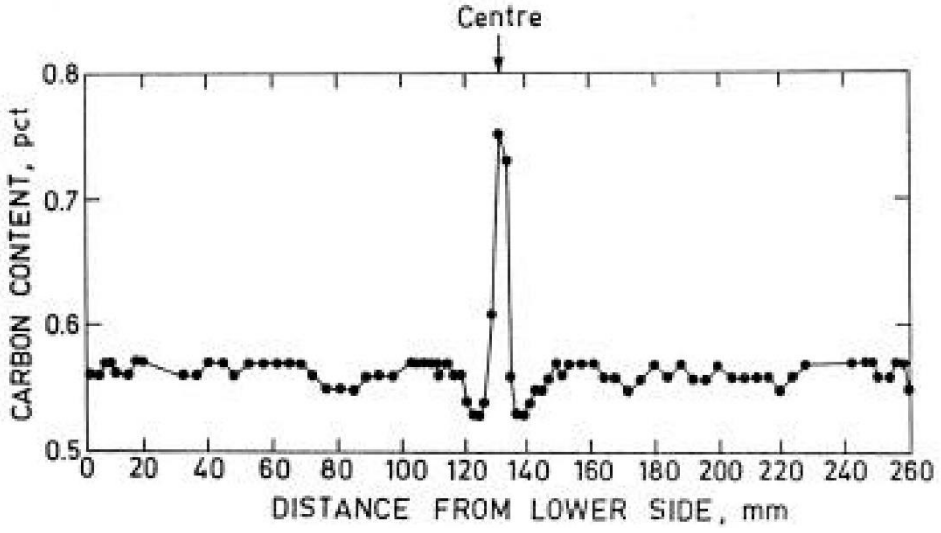

Figure 2.13: Centreline macrosegregation in continuous casting of steel [83].

2.4 MATHEMATICAL MODELLING

As already stated before that during continuous casting of steel, phase change of liquid steel to semi-solid cast product takes place due to heat extraction process. The complex interaction between heat transfer and fluid flow begins as soon as the liquid steel comes in contact with the continuous casting mould and it continues till the point of complete solidification. The fluid flow at the entry into the mould is highly turbulent, the intensity of which decreases as solidification proceeds until completion. Even after a certain degree of solidification, the laminar nature of the fluid flow ahead of the solidification front may be sufficient enough to alter the solute redistribution. All these high temperature coupled interactions are very difficult to visualize under real experimental conditions – due to the safety issues involved in conducting those high-temperature experiments in continuous casting moulds and the excessively high cost of the infrastructure involved to carry out the experiments. In this regard, mathematical / numerical modelling has gained worldwide acknowledgment in numerous fields to understand the details of such complex phenomenon with the availability of high performance computing power. Mathematical modelling involves the solution of various complicated mathematical expressions that represent the underlying physics of the engineering or scientific phenomenon like solidification during continuous casting of steel. Mathematical models generate an idealized picture of the situation, under reasonable, yet restrictive, assumptions – maximum benefit is obtained when comparing the outcome to experiments. Nowadays readily available commercial software packages (e.g. Diffusion-Controlled Transformations (DICTRA) [84], MICRESS [4], OpenFOAM [85] and so on) provide the flexibility of building a robust model right from basic stage to complicated ones by including step-by-step modifications through various add-on features available with the package. DICTRA is a package [86] for simulations of diffusional transformations (like heat treatment, carburizing, homogenization, microsegregation of alloys and so on) in multicomponent systems with one dimensional geometry. One of the drawback of various models (like lever rule, Scheil equation [30], Clyne – Kurz model [87]) used for estimating microsegregation is the assumption of constant partition coefficient of the solute element. But it has already been mentioned before that due to bulk convection the partitioning coefficient doesn't remain constant. OpenFOAM [20] has the advantage of having a set of precompiled libraries which can be customized by the

user as per the requirements. Despite the wealth of publications [87–89] on CFD, limited amount of literature can be found wherein coupling of OpenFOAM to Phase-Field methods have been carried out [90,91].

Recently decreasing computational costs due to advanced numerical methods and availability of high performance computing cluster is making life simpler to get into details of the complex engineering processes through the use of these mathematical models. All these models will give a near approximate realistic picture of the underlying complex scientific phenomenon from micro scale to macro scale. The first step in mathematical modelling involves identifying the governing equations that best captures the physics of the phenomenon under study. In order to complete the theoretical picture, appropriate boundary conditions and initial conditions need to be taken into account. Considering the restrictive assumptions, the equations are numerically solved after being discretized on a selected computational domain. A model validated with literature data as well as real-life experimental measurements will be ready to get implemented for engineering applications.

2.4.1 Fluid Flow

Fluid flow during the continuous casting process is one of the main building blocks that govern the heat transfer behavior and the final solidification structure. In continuum mechanics, the extensive properties like mass, momentum, and energy are governed by conservation laws. For the dynamics of fluid, the chosen approach is Control Volume (CV) where the flow inside an infinitesimal space called the control volume is considered. Quantitative estimation of the flow pattern of liquid steel inside the continuous casting mould can be determined by numerically solving the continuity equation (mass conservation) and the incompressible (assuming liquid steel to be a Newtonian fluid) single-phase Navier-Stokes equation [92] (momentum conservation) which are given as

$$\frac{\partial \rho}{\partial t} + \rho\left(\nabla . \vec{V}\right) = 0 \qquad (2.3a)$$

$$\rho\left(\frac{\partial\vec{V}}{\partial t}+\vec{V}.\nabla\vec{V}\right)=-\nabla P+\nabla.\left(\eta\nabla\vec{V}+\nabla\vec{V}^{T}\right)+S \qquad (2.3b)$$

where ρ is the liquid steel density (kg/m^3), η is the dynamic viscosity (kg/ms), P is the pressure (N/m^2), t is the time and S is the source term (if any). The first term in each of the above equations represent the transient term followed by convection term. The source term S may involve the thermal buoyancy effect, the solute buoyancy effect [93] on fluid flow, forces like electromagnetic force, body force, momentum sink term due to solidification of liquid steel. The 2nd term on the RHS in **equation 2.3b** is the diffusion term. Solving the Navier-Stokes equations will give the respective values of pressure and velocity components at each grid point within the domain. Computational fluid dynamics [94] deals with the study of solving such complex partial differential equations with the aid of computers. To get an approximate solution, several discretization methods are used to convert these differential equations into approximate non-linear algebraic equations that can be solved numerically. Discretization in space is done by breaking the total computational domain into finite discrete regions (or points), whereas for transient calculations the discretization in time is done by diving the time interval into small time steps. For transient / unsteady problems, because of their non-linear physical nature, an iterative scheme is followed to solve. The accuracy of the solution depends on the discretization method used. The grid size also affects the accuracy of the solution- finer grid enhances the accuracy but at the cost of computational time and memory. The most commonly applied discretization methods [94] are – Finite Difference Method (FDM), Finite Volume Method (FVM) and Finite Element method (FEM). The FVM deals with the integral form of the governing equations and it requires appropriate methods to approximate the volume and surface integrals. The computational domain is sub-divided into a number of non-overlapping control volumes and the governing equations are applied to each of those control volumes. Each of the CV is bounded by a set of faces and each face is shared between other neighbouring CV's. The computational nodes are situated at the centre of CV. The method is based on global conservation by construction and is suitable for complex geometries. This is why it is preferred widely nowadays over FDM. In the explicit method of temporal discretization, the variable (for which solution is sought) value at i'th grid point is determined from the known values of the rest of the terms like source term, flux etc. at the previous time-step. This method is

1st order accurate with time and will give quicker solution subjected to restriction on the time step size for a stable solution. On the other hand in the implicit method of temporal discretization, the only known value is the variable value at the previous time-step and rest of the terms like source, flux term etc. are evaluated along with variable value from current time-step which are unknown. This method is more stable in finding a solution but comes at the cost of additional computational time, compared to the previous explicit method. Other time discretization schemes for unsteady problems are being explained in literature [94]. The main problem of solving the Navier – Stokes equations is that there is no independent equation for pressure. Hence well-established algorithms like SIMPLE, PISO [94] etc. construct an additional pressure equation from the momentum equations that satisfies the continuity equation. The high energy of the incoming liquid steel stream from SEN during continuous casting gets cascaded down in the form of eddy currents or recirculation towards the mould exit as the solidification continues. Popular commercial software packages for calculating fluid flow include OpenFOAM [85], CFX [95], FLUENT [96] and so on.

Solving the transport equations for mass, momentum, energy and solute, Guthrie et al. [97] studied the evolution of macrosegregation for an iron-carbon binary alloy in a continuous billet caster. The model was based on the concept of two-phase mixture continuum model where each point in the domain is a mixture of solid and liquid phases respectively. The average mixture velocity was thus a sum of the liquid and solid velocity weighted by respective fractions. Mushy zone was assumed as a porous medium so that Darcy law could be applied. Porosity of the mushy zone was equal to the liquid fraction. Hence the porosity was zero when the material was fully solid. The momentum sink term was included in the source term. When fully liquid the momentum sink term becomes zero [98]. As the solidification goes on, the porosity decreases and the momentum sink increases. In fully solid zone, the condition is that the solid will move as the casting speed. Left portion of the **Figure 2.14** shows the instantaneous fluid flow pattern of liquid steel inside the mould obtained by direct numerical solution of the Navier-Stokes equation as reported [99]. The right image shows the fluid flow pattern as obtained by particle image velocimetry technique (PIV) in water model. The arrow head mark of the arrows shows the direction of the velocity vector. At the liquid steel entry point from the SEN nozzle into the mould, high density of the velocity vectors can be seen. The liquid steel after exiting from the nozzle directly hits mould walls. A portion of the flow travel upwards while rest travel

downwards in the casting direction. Argon injection [100] rate through the SEN nozzle have a considerable effect on the fluid flow pattern which can affect the steel quality. Transient phenomenon like sudden change in the casting speed, abnormal surface level fluctuations [101] may induce asymmetric flow thereby having a direct impact on the quality of the cast product.

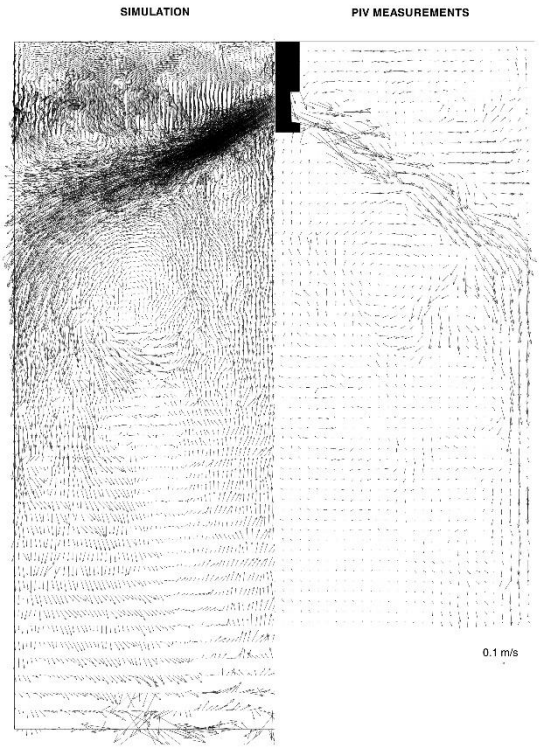

Figure 2.14: Instantaneous liquid steel flow pattern inside a continuous casting mould; (Left) numerical simulation; (right) PIV technique in a water model [99].

2.4.2 Modelling of Phase Formation

Any liquid metal casting process is relevant in terms that it determines the kinetics of phases that forms, its morphology and size distribution / structural length scales which affects the internal soundness / quality of the cast structure and hence deeply influences the mechanical properties of the cast product. The actual structural length scales of the phases that form during continuous casting process range from few μms to several mms along the several meters long cast steel slab, thereby defining its multi-

scale nature. The kinetics of the phase formation and its morphology governs the segregation of the product. From a customer point of view, the utmost demand is a high-quality cast structure with a minimum of defects and a uniform chemical composition (i.e., minimum macrosegregation). Thus, a steelmaker has to optimize the continuous casting process so as to satisfy the needs of the customer resulting in increased profitability. A combination of the influence of casting parameters like casting speed, cooling rate, liquid steel chemistry and super-heat controls the final cast structure during the solidification process. Due to the large cross-sectional area of the cast slabs, the cooling conditions and release of latent heat vary considerably from surface to the central core of the slab, which influences the phase evolution mechanism. Hence, the need to have thoughtful insights into the formation of phase evolution mechanism to achieve a better product quality.

In early years, the optimization of the casting process was primarily done by correlating the casting process parameters by thorough experimental characterization of the cast steel samples cut from the actual slabs. This was indeed quite a hectic and time-consuming task. With the advent of high-performance computing power, people started to develop various models to track the phase evolution mechanism in the product in an efficient and fast manner. The main ingredients in such models include the mathematics that describes the release and transport of heat and species along with appropriate boundary conditions that rule the thermodynamics at the interface. Modelling of phase evolution is quite a demanding job because of the complex interaction of the solid phase with the bulk fluid flow, particularly in the two-phase mushy zone. With the progress of solidification, solute-rich liquid steel gets continuously accumulated in the various pockets of the solidified dendrites. Combination of various factors like thermo-solutal effect over different length and time scales plays an important role in understanding the kinetics of phase transition. Since solidification is a heat transfer coupled fluid flow as well as a mass transfer phenomenon, it requires numerical solution of mass and momentum equations along with the heat diffusion equation. Moreover, the modelling situation becomes more challenging, as the number of solute elements with different partitioning and diffusion coefficients increase.

Advanced numerical methods have helped further in understanding of the very details of the transport phenomena during solidification. Two types of approach are available in literature – deterministic approach and stochastic (probabilistic) approach. In

deterministic modelling, the continuum equations are solved over the whole mesh. Most of the deterministic methods are based on the simplification that the solid phase has zero velocity. In the deterministic models, the initial mesh is divided into macro volume elements within which temperature is assumed to be uniform. Within each macro volume element, solid grains are allowed to nucleate based on nucleation laws. Volume averaging technique, front tracking method, Phase-Field Method are such common deterministic numerical methods of modelling the phase evolution while methods like Cellular Automaton (CA) or Monte Carlo Method (MC) (mainly used for diffusion simulations) are the stochastic ones. Each method has its own advantages and disadvantages. A detailed description of Phase-Field Method will be discussed later.

a) Front Tracking Method

The front tracking method of S/L interface [102] during solidification is one of the most common methods of explicit tracking of the interface to understand the mechanism and kinetics of phase evolution. In this case, the solid and liquid phases are considered as different entities and the continuity equations like heat diffusion equations are solved separately for each of the phases. Because of its explicit nature, an additional continuity equation for the interface is also solved. One of the main problem for this method is the explicit tracking of the interface (because of its complicated geometry) which makes the numerical method computationally intensive in 2D and even more in 3D. This method is also called 2-domain method. Industrial alloys have a large mushy zone rather than a sharp S/L interface. In the 3-domain method, the continuity equations are solved for each of the three domains – solid, mushy zone and liquid. The front tracking method also called the Sharp Interface Method is thus a direct phase evolution modelling approach where the grid points and time step are chosen so that they scale with the smallest length and time scales of the problem. A well-known example of such a method is the solidification of a pure material in an undercooled melt, known as the Stefan problem. In this case, the advancement of the solidification front is governed by how quickly the latent heat diffuses away from the S/L interface and the ability of the interface to maintain specific boundary conditions.

Similarly, for solidification of binary alloy [103], additional set of partial differential equations governing the diffusion of solute in solid and liquid phases have to considered along with the solute flux balance at the solid/liquid interface. As mentioned before, the heat transfer equation contains a term that takes into account the latent heat release that depends on the fraction of solid. Assuming a simple relationship between temperature and the solid fraction will give the macroscopic evolution (of temperature or solid fraction) while it fails to predict the phase evolution in micro scale. Thus, to predict the phase evolution at the micro level, one has to take into account the nucleation and growth phenomenon of the solid particles at micro level and couple them with the macroscopic continuity equations. This is called macro-micro coupling method for modelling of solid phase structure / microstructure during solidification. Because of the averaging technique, this method is more suitable for industrial solidification problems involving mushy zone formation across varied length scales. Obviously, some information will get lost due to averaging technique but it is preferred over the computationally intensive 2-domain methods. The importance lies in the choice of the volume, over which the averaging is carried out and the functional relationship of solid fraction with time.

Microscopic models are those models which are associated with the nucleation and growth phenomenon during solidification. The aim is to obtain an appropriate solid fraction relationship to couple with the macroscopic heat transfer equation so that the solidification conditions like undercooling can be related to the microstructural features. A brief review of the nucleation and growth models for phase evolution modelling is given by Stefanescu [104]. Most of the empirical equations for nucleation models are based on fitted experimental data for specific experimental conditions. One set of experimental data that works well with one model may not work for other models. Volume averaging is a very popular technique where one can relate the macroscopic variables to their microscopic counterparts. In this technique, the macroscopic transport equations are numerically solved based on the representative volume elements that form the computational mesh. Interface microscopic phenomena like solute rejection, latent heat release, mass transfer due to solidification etc. are volume averaged in those representative volume elements and this accounted for some disagreements with the experimental results. Each grain considered as a dendrite envelope is defined as the surface that touches all the tips of the primary and secondary dendrite arms. Thus it includes solid and inter-dendritic liquid and not the extra

dendritic liquid. Models based on volume averaging techniques are called continuum models. Two-phase models developed by Beckerman et al. [105] and Prakash et al. [106] consist of separate volume averaged continuity equations for solid and liquid phases including the interfacial transfer terms. Wang and Beckerman [107] have utilised this technique to develop multiphase solute diffusion models for dendritic alloy solidification. Ludwig et al. [108] in the two-phase volume averaging model, modeled the formation of equiaxed solidification microstructure by considering separate conservation equations (mass, momentum, species, and enthalpy) for solid and liquid phases respectively. It is based on the continuum model developed by Incropera et al. [109]. In the three-phase volume averaging model, Ludwig et al. [110] assumed the columnar dendrites as one of the solid phases and equiaxed grains as the second solid phase. Phenomenon like columnar to equiaxed transition, grain structure distribution, and sedimentation of floating grains can be effectively modelled for ingot solidification. However, though it modelled the formation of columnar dendrites but the preferred growth orientation of the growing dendrites were not taken into account.

In addition to the macroscopic governing equations, several other auxiliary governing equations which relate macroscopic to microscopic processes are also taken into account. Once solid nuclei have formed, its growth with time influences the heat and solute diffusion equations in macro level due to the release of latent heat and excess rejected solute. Since the solidification of alloys occurs over a large range, various microsegregation models have to be applied to take the solute diffusion effect into account to determine the solid fraction. Under the assumption of local interfacial equilibrium, the phase fractions can be correlated to macroscopic temperature with the help of equilibrium phase-diagrams. The simplest microsegregation model [104] is based on the lever rule where one assumes complete mixing in both liquid and solid, while Scheil model assumes complete liquid mixing and no mixing in solid. Thus it is the solute diffusion model (like lever rule) which links the macro model to microscopic phenomenon. Most of the macro-micro coupled models in literature [87,111–113] have either assumed lever rule or Scheil model which are the two extreme cases. For predicting macrosegregation, most of them [114,115] have taken into account the flow due to shrinkage or solid deformation into account. They have not taken into account the effect of bulk convection on the solute boundary layer. Also most of the reported works were on evaluating the macrosegregation in ingot casting or the centreline segregation in continuous casting. The author have not found enough literature on how

the zone of dominance of the solute washing effect by bulk fluid flow shifts in a continuously cast steel slab. The challenge lies in taking into account the physics of the various types of flow starting from the beginning of solidification process till the point of metallurgical length in a continuous casting process. Hence evaluating the macrosegregation phenomenon [112,116,117] is still a persisting problem. For complex alloy systems, the phase equilibrium data from the Gibbs free energies of the liquid and solid phases as a function of composition and temperature are determined through thermodynamic software like Thermo-Calc [10]. Various numerical schemes [102,104] for macro-micro coupling include equivalent specific heat method, enthalpy method, micro enthalpy method, latent heat method etc. Other dual macro-micro scale models for alloy solidification using the concept of mixture theory are detailed in [89,118,119]. Since the growth [102] of a dendrite tip depends on the local solute and temperature gradients, the functional relationship of the solid fraction with temperature depends on the solidification conditions ahead of the tip. Voller et al. [120] developed a unique numerical modelling technique for treating the evolution of mushy zone during the course of phase change. They considered the case of freezing of liquid in a cavity which was treated as a porous medium. In fully liquid state the porosity was taken as 1 while in solid state the porosity was zero. The superficial velocity in the momentum equations was defined as the liquid fraction multiplied by the actual fluid velocity. CON1D heat flow model developed by Thomas et al. [121] simulates in 1D the growth of steel shell in a continuous casting mould.

The influence of convection during solidification occurs at both macroscopic and microscopic levels. At macro scale, it reduces the thermal gradient within the liquid core, while it also affects the local solidification conditions in front of a growing interface at microscale. Thereby it affects the segregation and phase evolution at both levels. With the increase of solid fraction during continuous casting, the effect of bulk convection diminishes and local / natural convection due to density gradients gains importance. The accurate way to determine the effect of convection is to calculate the velocities from the Navier-Stokes equations. In 2-domain methods, the fluid flow equations are solved within the liquid region only. Several techniques [109,120] like increasing the viscosity with the progress of solidification, average velocity field as a function of solid and liquid fraction have been applied to take the flow resistance due to solid mush into account. Assumptions in these models include laminar Newtonian flow in the liquid with constant viscosity. Inertial differences between liquids of

different densities are ignored. The problem in these multi domain models lies in the explicit tracking of the interface of the phases.

Until now, only the continuum scale modelling methods have been discussed, where some kind of averaging techniques are used to couple the microscale features with the macro scale phenomenon. Advancements in computing speed, numerical methods, parallel computing on high-performance machines etc. have shown a green signal to small scale simulations to have the multiscale effect even in 3D. **Figure 2.15** shows various models used for the phase evolution in literature. Phase-field method and the molecular dynamics simulations take into account the full complexity of the S/L interface during the entire solidification process. They are far more accurate than the averaging methods discussed above but they come at the cost of computational time. In the probabilistic methods, the computational domain is divided into a number of cells. All the variables and states (like liquid / solid for solidification) are associated with each of the cell. The neighborhood influence of surrounding cells are also considered. Then transformation rules that govern the phase evolution of the states and variables of the cells are defined. The stochastic methods [66] describe the dendrite growth envelope or the development of the morphology of dendrite grains. In the field of steel metallurgy, the method is mostly applied to understand recrystallization, grain growth or phase transformation phenomena. In the Monte Carlo (MC) method, the physical problem is looked from a probabilistic or statistical model point of view. It is mainly a mesoscale model to develop the grain structure in cast product. The correspondence between MC time step used in calculations and real time is not clear. Also this method lacks the physical principles [122] of the dendritic or equiaxed growth, since the evolutionary rules are purely probabilistic. The main output of such models is to show the grain boundary development and grain impingement without any description of the interface dynamics associated with the primary and secondary dendritic arms.

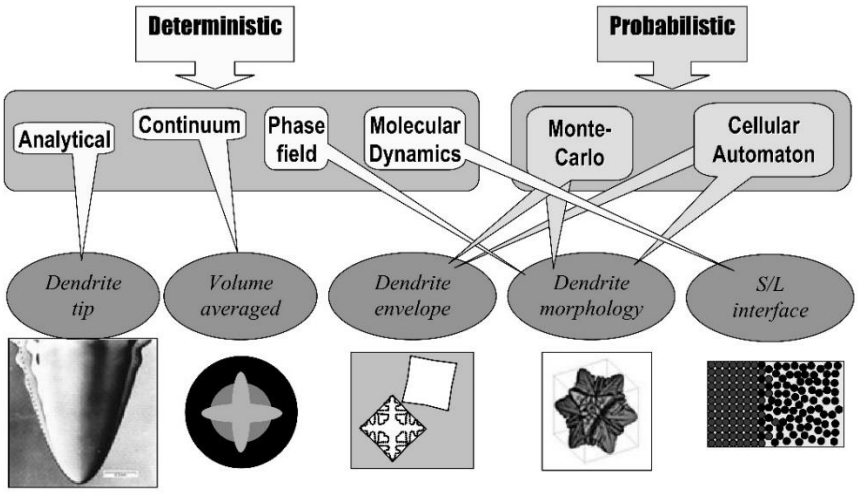

Figure 2.15: Various computational models for phase evolution [66].

b) Phase-Field Method

Phase-Field Method is an implicit front tracking algorithm derived from continuum thermodynamic principles to study the kinetics of phase evolution mechanisms in the field of materials science. This method is now widely used not only to study phase evolution in solidification but also in solid state phase transformations, grain growth and coarsening phenomena, microstructure evolution in thin films, crack propagation [123] and so on. Consider the case of solidification of a pure material, where a liquid phase having temperature above the melting point gradually transforms into a solid phase due to heat extraction. This happens because of lowering the local system temperature, resulting in nucleation of a stable solid phase and its further growth at the expense of the unstable liquid phase. This is because at temperatures below T_m (freezing / melting point), the Gibbs free energy of the solid is less than that of the liquid phase and vice-versa (as shown in **Figure 2.16a**). At the equilibrium melting temperature, the solid and liquid phases will coexist. This signifies the presence of some boundary or interface between the phases. The creation of any surface requires some energy. Thus the creation of new solid phases necessitates the creation of solid – liquid interface associated with the S/L interface energy σ. Physical properties like temperature, pressure, volume, internal energy define the thermodynamic state of a system.

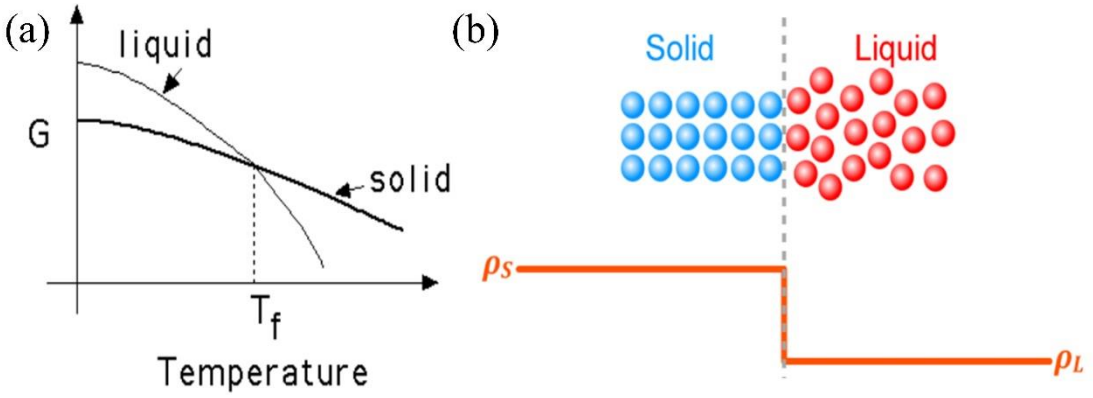

Figure 2.16: Solidification of pure material; (a) variation of Gibbs free energy with temperature [124]; (b) schematic of a S/L interface [125].

Figure 2.16b shows an S/L interface where the interface is defined as the region between the close-packed solid spheres and the dense but randomly packed liquid spheres. As shown in the figure, the density of the solid phase changes in a discontinuous sharp manner at the interface and then becomes again constant in the pure liquid phase. Similarly, the free energy of the solid phase will change abruptly to that of the liquid at the boundary. In general, in a continuous solidification process, the solid-liquid interface (or solidification front) gradually moves with the progress of solidification till it vanishes, when solidification is complete. This movement is based on how fast the atoms in liquid state cross the energy barrier and attaches on the solid side of the boundary.

Phase-field method based models mimic the S/L interface as a continuous thin transition layer, having a thickness wide enough compared to the actual length scale of a physical interface (~ nm) but small enough, compared to the structural length scales (~ several μms) obtained in standard solidification castings. The avoidance of the problem of explicit tracking of the interface is done by using an additional dimensionless variable ϕ (function of space and time) called the Phase Field variable, which takes the value of 0 in fully liquid phase and 1 in fully solid phase. Any intermediate values of ϕ (say $0.05 < \phi < 0.95$) signify the interface. The physical relevance is that the amplitude of this phase density function is constant in both the bulk phases whereas it changes only at the interface. The set of values of the variable in the whole volume is defined as the phase field. The kinetics of the phase evolution during solidification is thus given by an additional equation for the phase field

variable, which is derived by forming an expression for the entropy distribution of the system and assuring positive entropy generation. Thus, no separate equations for both solid and liquid phase are needed to solve. This versatile technique is applied in various fields of materials science like thin films, solidification, solid-state phase transformations, study of interface dynamics in two-phase flows and so on. One of the serious limitations of this technique is that the computational mesh has to be sufficiently fine to capture the interface dynamics, which leads to massive computational requirements. Because of the continuous transition of ϕ across the phase boundary, the computed interface between the two phases is called diffuse interface as opposed to the sharp interface in reality. **Figure 2.17** shows the difference between sharp and diffuse interface. Making the interface more diffuse (i.e., thicker) enables one to use larger grid size and quick calculations. The interface thickness has to be so chosen such that the numerical predictions must capture the physics of the underlying problem and must be similar to that of the experimental results. The interface thickness is defined as 2λ. **Figure 2.18** shows [11] the profile of the phase field variable across a S/L interface in solidification.

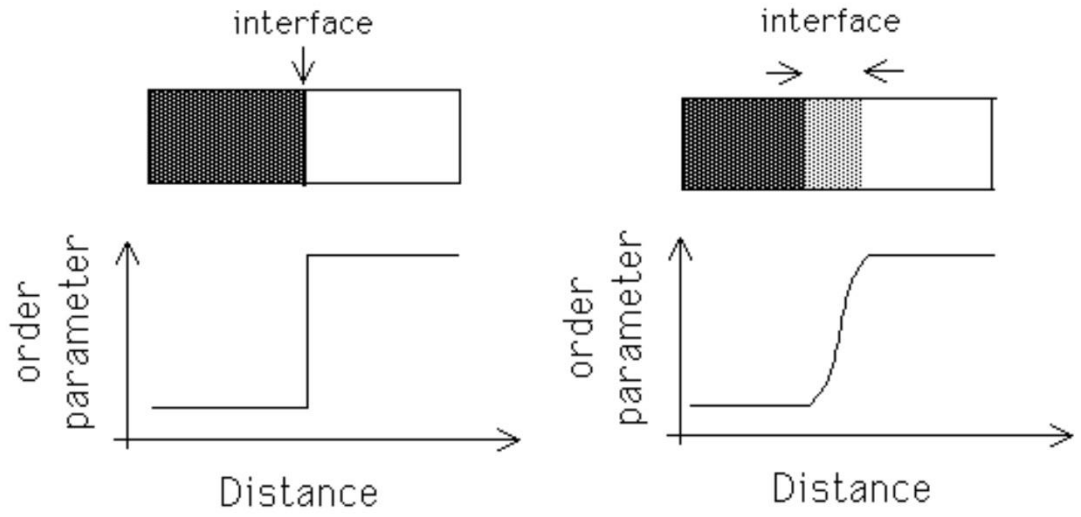

Figure 2.17: Schematic of sharp Interface (1st) and diffuse Interface [126] (2nd).

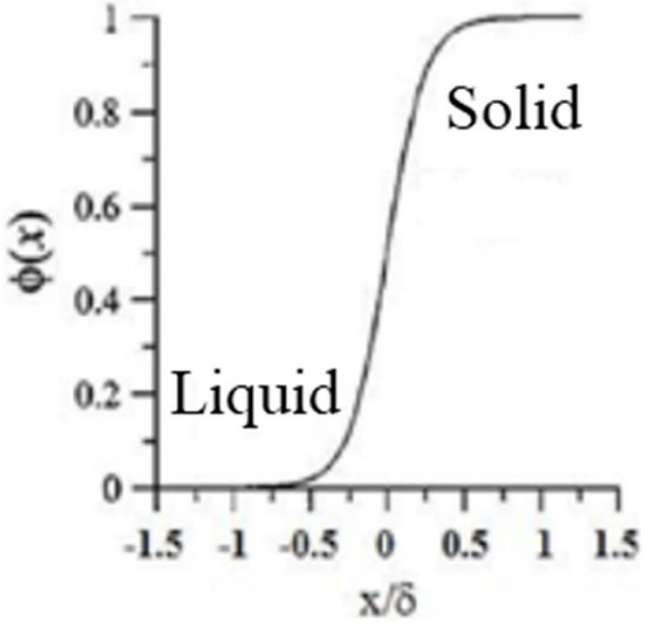

Figure 2.18: Phase field variable across a S/L interface [11].

The real essence of the phase-field method stems its origin from the well-known Cahn Hilliard equation [127] originally developed to model the spinodal decomposition of a binary system A-B at a fixed temperature. It describes the temporal and spatial evolution of a conserved field like composition. It was assumed that initially, the system was homogeneous with uniform composition and with the progress of time the system splits into two phases (e.g. α and β) of different compositions, according to the principles of minimization of gradients of the chemical potential. The main point to note here is that the interface between the phases is not sharp but rather diffuse with a finite thickness across which the concentration varies gradually. Consider a binary solid solution of A and B atoms. Let $f_0(Composition)$ be the Helmholtz free energy per unit volume of the homogeneous system at temperature T and $F(Composition)$ be the total free energy of a heterogeneous system, consisting of α and β phases. Using a Taylor series expansions Cahn and Hilliard [127] obtained the following expression (from the principle of Ginzburg–Landau free energy theory) for the Helmholtz free energy of the heterogeneous system (of the phases say α and β)

$$F(Composition) = \int \left[f_0(Composition) + \frac{\varepsilon^2}{2} (\nabla Composition)^2 \right] dV \qquad (2.4)$$

where ε^2 is called the gradient energy coefficient.

The above equation reveals that the free energy of a heterogeneous system is the sum of the free energy of the homogeneous system and the gradient energy which is the excess free energy due to interface because the material at the interface is neither fully equilibrium α nor fully equilibrium β. This provides the very basis that the interphase boundary must take into account the finite non-zero width of the phase separation. The concept of gradient energy [128] stems from the fact that when two separate homogeneous solutions of A and B atoms are mixed, then the free energy of the final heterogonous system will be the sum of the individual bulk free energies of the homogeneous systems and the excess free energy due to mixing.

Allen-Cahn [129,130] instead of the concentration variable, used the order parameter and termed it as phase field variable ϕ . Thus the free energy density will be given in terms of ϕ and it's gradient as

$$F = \int \left[f_0(\phi) + \frac{\varepsilon_\phi^2}{2} |\nabla \phi|^2 \right] dV \tag{2.5}$$

For equilibrium, one needs to fulfil

$$\frac{\delta F}{\delta \phi} = 0 \tag{2.6}$$

The thermodynamics of irreversible systems [126] deals with the non-equilibrium systems, where there is constant dissipation of free energy (or increase in entropy). Here, the flux describing the rate of change of a system is proportional to the force, responsible for the change. Hence the rate of evolution of the phase field variable ϕ (i.e., the flux) is proportional to the change of free energy (i.e., the force) given as

$$\frac{\partial \phi}{\partial t} = -M \frac{\delta G}{\delta \phi} \tag{2.7}$$

The above equation is also called the Allen-Cahn Equation or time-dependent Ginzburg-Landau equation where G is the total Gibbs free energy functional of the system, $\frac{\delta G}{\delta \phi}$ is the variational derivative of Gibb's free energy w.r.t ϕ which must decrease and M is the constant phase field mobility [130]. The above equation is the case, where the phase field variable is not conserved. For e.g. in solidification, the volume of each of the phases is not constant.

The total Gibbs free energy functional G of a heterogeneous system, involving more than one component is given as

$$G = \int \left[g(\phi, C, T) + \frac{\varepsilon_\phi^2}{2} |\nabla \phi|^2 + \frac{\varepsilon_C^2}{2} |\nabla C|^2 \right] dV \tag{2.8}$$

where the free energy density $g(\phi, C, T)$ is a function of phase field variable, composition (C) and temperature (T).

For pure materials, the **equation 2.8** will be

$$G = \int \left[g(\phi, T) + \frac{\varepsilon_\phi^2}{2} |\nabla \phi|^2 \right] dV \tag{2.9}$$

where ε_ϕ^2 is called the gradient energy coefficient due to the gradient of the phase-field within the interfacial region. The 1st term is the sum of the free energies of the solid phase, liquid phase and the double-well potential at the interface. The 2nd term is valid only in the interface region and is related to the interface energy. It is constant for isotropic interface energy.

From the principle of thermodynamic equilibrium for the solidification of a pure material, the free energy density must have constant values in the bulk solid and liquid phases respectively. As mentioned earlier, there exists a free energy barrier for transformation from liquid phase to solid phase. **Figure 2.19** shows various shapes of the free energy density function as a function of the phase-field variable and T_m which is the melting point where the free energy densities of bulk solid and bulk

liquid phase are equal. Please note that phase-field variable value of 1 signifies pure solid phase and value of 0 signifies pure liquid phase. The total free energy density for solidification of pure material is written as

$$F = \int \left[W g(\phi) + h(\phi) f_S + \big(1 - h(\phi)\big) f_L + \frac{\varepsilon_\phi^2}{2} |\nabla \phi|^2 \right] dV \tag{2.10}$$

where f_S is the free energy of the solid phase, f_L is the free energy of the liquid phase, $g(\phi)$is a double well function, W is the height of the energy barrier at the interface and $h(\phi)$ is a monotonically increasing interpolating function satisfying $h(0) = 0$, $h(1) = 1$ and $h'(0) = h'(1) = 0$. The profile of $h(\phi)$ is shown in **Figure 2.20a**. The double well function is also a polynomial in ϕ with non-zero values only near the interface i.e., $g(0) = g(1) = 0$. The profile of the function is shown in **Figure 2.20b** which has the form

$$g(\phi) = \phi^2 (1 - \phi)^2 \tag{2.11}$$

It can be seen that in a fully solid phase, the total free energy is equal to the free energy of the pure solid phase and in fully liquid phase the total free energy is equal to the free energy of the pure liquid phase. Two types of polynomial expressions for $h(\phi)$ are used in literature [131]:

$$h(\phi) = \phi^3 (10 - 15\phi + 6\phi^2) \tag{2.12}$$

$$h(\phi) = \phi^2 (3 - 2\phi) \tag{2.13}$$

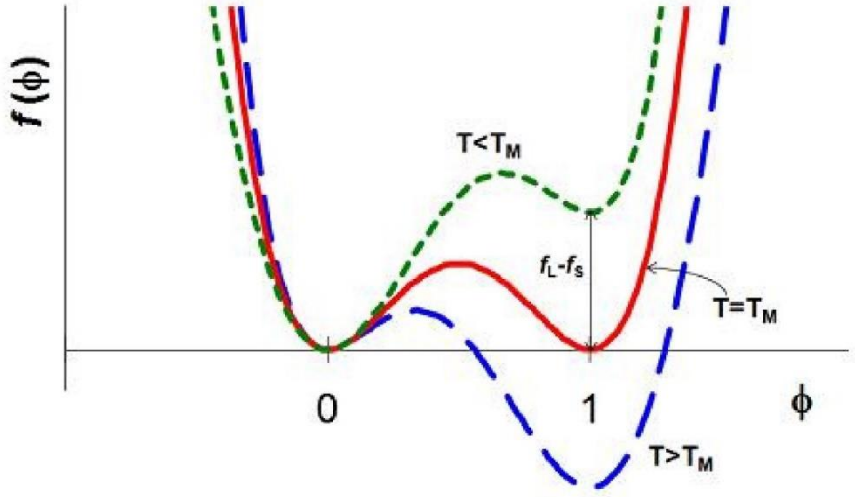

Figure 2.19: Variation of free energy density function [132].

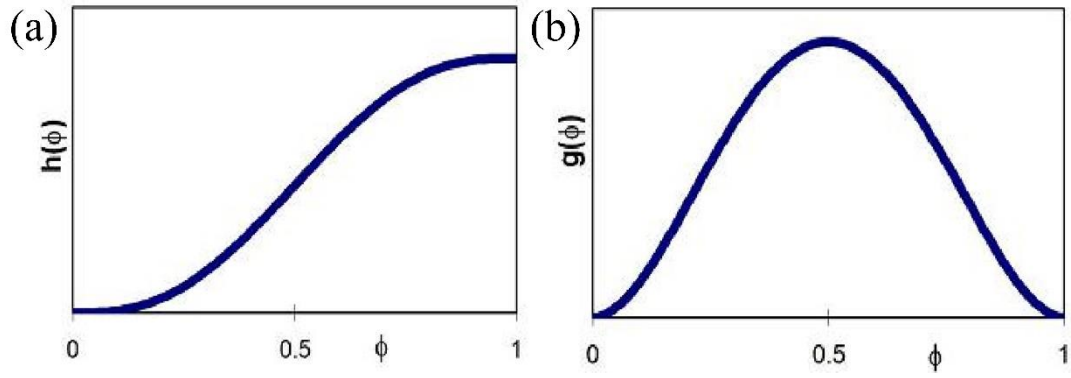

Figure 2.20: Profile of the mathematical functions; (a) interpolating function $\boldsymbol{h(\phi)}$ [132]; (b) double well function $\boldsymbol{g(\phi)}$[132].

2.5 SUMMARY

This chapter gives a comprehensive overview of the various topics related to this research from literature. The chapter starts with the basics of continuous casting of steel and how fluid flow as well as heat transfer are relevant to it. Following that the fundamental theories on the formation of solidification microstructure during solidification and how fluid flow effects the microstructure were discussed. At last various methods of modelling fluid flow as well as phase formation were discussed.

CHAPTER 3: MODEL DEVELOPMENT

The purpose of this chapter is to give reader an overview and physical significance of the various governing equations used in the present work. The significance of the various variables and constants used are also mentioned. Variation across different length scales of phase evolution during solidification define the final properties of the solidified cast product, resulting from a continuous casting process. Considerable challenges are still present in quantitative understanding of the complicated evolution of the dendritic structures in solidification due to the non-linear coupling of heat, mass and phase transition. Building a micro scale solidification model requires accurate incorporation of the physics of thermodynamics and hence the phase-field method is being used in the current work. Kobayashi [133] used the phase-field method along with the anisotropy function of interface energy to represent the evolution of dendritic patterns in an undercooled single component melt. Based on the 2nd law of thermodynamics, Wang et al. [131] deduced phase-field models that had a strong resemblance to that of Kobayashi [133]. Starting from a pure metal, Kim et al. [134–136] and Boettinger et al. [11,137] deduced the phase-field models for alloy solidification in a thermodynamically consistent way. Based on the free energy density functional, Kim et al. in his model [134,136] of binary alloy solidification assumed the interface to be a mixture of solid and liquid phases with different compositions but with same chemical potential. The model developed by Kim et al. [134–136] at a dilute solution limit can be reduced to the model developed by Steinbach [138]. The model developed by Kim et al. [134–136] has been widely used for simulating the microstructure evolution in Fe-C binary alloys [136,139,140]. Other works on phase field modelling of solidification in binary [137,141] Fe-C alloys and ternary [142,143] Fe-C-P alloys are also reported in literature.

3.1 GOVERNING EQUATIONS for SOLIDIFICATION

3.1.1 Temperature Evolution

Let us consider the case of solidification of pure Nickel [135,144]. Simulation of phase-field method based solidification in single component system is easily available for nickel. Hence pure Nickel (Ni) was chosen as the starting material during the initial phase of the PhD work to establish a basic phase field solidification model and validate by reference to available data. The value of the phase-field variable ϕ indicates the thermodynamic stable phase of the system as a function of time, *t* and position, *x*. The thermal energy transport equation for solidification of pure material [135] under a non-isothermal temperature field is given as

$$\frac{\partial T}{\partial t} = D_T \nabla^2 T + \frac{\Delta H_m}{C_p} h'(\phi) \frac{\partial \phi}{\partial t} \tag{3.1}$$

where T is the temperature in Kelvin (K), t is the time in secs, D_T is the thermal diffusivity in m^2/s, ΔH_m is the latent heat of melting per unit volume in J/m^3, ϕ is the phase-field variable, C_p is the material specific heat in J/m^3K. The 2nd term on the RHS in **equation 3.1** represent the removal of latent heat associated with the rate of phase evolution. The chosen polynomial for the interpolating function is given as [135]

$$h(\phi) = \phi^3(10 - 15\phi + 6\phi^2) \tag{3.2}$$

By choosing the above interpolating function, we have $h'(\phi) = 30g(\phi)$. It is reasonable to assume the specific heat capacity and thermal diffusivity of solid and liquid phase to be equal and constant. This is because the temperature range for the modelling being small enough so that the difference in those parameters for both phases will be small.

3.1.2 Solute Diffusion

The solute transport equation [134] for diffusion of solute in a two component system (binary alloy) is given as

$$\frac{\partial C}{\partial t} = \nabla.\left(D(\phi)\{\big(1-h(\phi)\big)C_L(1-C_L) + h(\phi)C_S(1-C_S)\}\nabla ln\frac{C_L}{(1-C_L)}\right) \quad (3.3)$$

where C is the solute concentration in the interface region in mole fraction, C_L and C_S are the solute concentrations of the liquid and solid phases in mole fraction, $D(\phi)$ (in (m^2/s) is the solute diffusivity as a function of ϕ and defined as

$$D(\phi) = \big(D_S h(\phi) + \big(1-h(\phi)\big)D_L\big) \quad (3.4)$$

where D_S and D_L are the solute diffusivities in solid and liquid phases respectively. It is to be noted that no convection term has been shown in the **equation 3.3**.

The solute concentration [134] in the interface region, C is given as

$$C = \big(C_S h(\phi) + \big(1-h(\phi)\big)C_L\big) \quad (3.5)$$

Local equilibrium has been assumed at the interface. Kim et al. [134] assumed the interface as a mixture of solid and liquid phases respectively with different compositions but with same chemical potential (across the interface only at a thermodynamic equilibrium state) which for a dilute solution yields

$$\frac{C_S^{eq}C_L}{C_L^{eq}C_S} = \frac{\big((1-C_S^{eq})(1-C_L)\big)}{\big((1-C_L^{eq})(1-C_S)\big)} \quad (3.6)$$

where C_S^{eq} and C_L^{eq} are the equilibrium solute compositions of the solid and liquid phases respectively at a particular temperature.

Taking $h(\phi) = \phi$, Kim et al. [134] modified his original solute transport **equation 3.3** and showed that the modified version resembles Steinbach's model [138]. The modified equation [134] is given as

$$\frac{\partial C}{\partial t} = \nabla.[D(\phi)\nabla \mathrm{C}] + \nabla.(D(\phi)(C_L - C_S)\nabla \phi) \tag{3.7}$$

3.1.3 Phase Evolution

The phase-field governing equation for solidification of a pure material [11,145] with isotropic interface energy is given as

$$\frac{1}{M}\frac{\partial \phi}{\partial t} = (\varepsilon^2 \nabla^2 \phi) - W g'(\phi) - h'(\phi)\frac{\Delta H_m}{T_m}(T - T_m) \tag{3.8}$$

where $Wg'(\phi)$is the imposed double-well potential [136] which is the excess free energy at the interface, M is the phase-field mobility (assumed to be isotropic) in m^3/sJ, and ε is the gradient energy coefficient which is related to the averaged interface energy σ of the material. The last term is the degree of undercooling which provides the driving force for the interface movement.

Solidification structure is the result of competition between the interface energy associated with the formation of a new surface and thermodynamic driving force due to undercooling. The phase-field variable ϕ gradually changes its value from 0 to 1 across a distance of finite value called the interface thickness (2λ). It is to be noted that this interface thickness is not a real physical one present in the actual solidification microstructure but rather a mathematical construction for solving the **equation 3.8** as stated by Kim et al. [134]. For the case of solidification, the free energy functional F of the system can be represented as a sum of the free energies of the bulk phases (i.e. solid and liquid) and the excess energy associated with the creation of the interface

typically called interface energy. The free energy functional is assumed to be a continuous function of the phase-field variable across the diffuse interface. The interface energy [11] constitutes the energy barrier at the interface (where W is the activation energy barrier) and the gradient energy (where gradient energy coefficient is denoted by ε) associated with the gradient of the phase-field variable across the interface. These are two counteracting effects – the gradient energy tries to widen the interface region to reduce the energy while the barrier height "W" tries to make the bulk phases stable by sharpening the interface region. This interface energy vanishes in the bulk phases and is non-zero in the interface region only. It is to be noted that both W and ε are computational parameters of the phase-field model. For isotropic interface energy, the equilibrium shape is spherical. The term ε is associated with the gradient of the phase-field variable i.e. $\nabla\phi$ as mentioned before. The above governing equation shows that the interface movement is the inter-play between smoothing by the diffusion term (that tends to make the interface diffuse to reduce gradient energy) against the thermodynamic driving force (that tends to make the interface sharp to minimize the excess material within the interface and stabilise the bulk phases).

The model parameters W, ε, and M are related to the material parameters as per the following equations [134,135,144].

$$\sigma = \frac{\varepsilon\sqrt{W}}{3\sqrt{2}} \tag{3.9}$$

$$2\lambda = \frac{2.2\sqrt{2}\,\varepsilon}{\sqrt{W}} \tag{3.10}$$

where $0.1 \leq \phi \leq 0.9$.

$$M = \frac{T_m\mu}{2.73\Delta H_m\lambda} \tag{3.11}$$

where μ (defined as the constant of proportionality between the S/L interface velocity and degree of undercooling) is the linear kinetic coefficient [146] in m/sK.

During the process of solidification, the atoms from the liquid side jump onto the solid side after overcoming the energy barrier. This atomistic jump process is a random process and thermally driven. In real systems, temperature fluctuations (in pure metals) ahead of the S/L interface create interface instabilities and thus drives the motion of the interface. To simulate the effect of random thermal noise [137,144] on the interface for solidification of pure material, the temperature variable in the phase-field governing equation was multiplied by

$$Noise = 16\alpha r\phi^2(1-\phi)^2 \tag{3.12}$$

where r is the random number generated between +1 and -1, α is the noise amplitude (taken to be 0.01 i.e. 1% random noise). From the **equation 3.12**, it can be observed that the noise will be generated only when ϕ has values intermediate between 0 and 1 i.e. at the interface only. Noise on total driving force signifies the noise term applied on the summation of 2nd and 3rd terms on RHS in **equation 3.8** whereas noise on latent heat release signifies the noise term applied on 3rd term only.

The governing equation for solidification of a pure material with anisotropy in interface energy is given as [144]

$$\frac{1}{M}\frac{\partial\phi}{\partial t} = \nabla.(\varepsilon(\theta)^2\nabla\phi) + \frac{\partial}{\partial y}(\varepsilon(\theta)\varepsilon'(\theta)\frac{\partial\phi}{\partial x}) - \frac{\partial}{\partial x}(\varepsilon(\theta)\varepsilon'(\theta)\frac{\partial\phi}{\partial y}) - Wg'(\phi) - h'(\phi)\frac{\Delta H_m}{T_m}(T-T_m) \tag{3.13}$$

where θ is the orientation of the normal to the S/L interface with respect to the positive *x* axis and defined [137] as

$$\tan\theta = \frac{\partial\phi}{\partial y}\Big/\frac{\partial\phi}{\partial x} \tag{3.14}$$

The most widely used method in phase-field models [11,135,144] to include the anisotropy is to assume ε as a function of θ represented as $\varepsilon(\theta)$. For materials with

cubic symmetry undergoing dendritic solidification, the weakly anisotropic nature of the interface energy in 2D is taken into account by assuming the following dependency of ε as

$$\varepsilon(\theta) = \varepsilon(1 + \delta_\varepsilon \cos(j(\theta - \theta_0))) \tag{3.15}$$

where δ_ε is the anisotropy constant and j is the mode of anisotropy respectively. The parameter j controls the number of preferential directions of the anisotropy in interface energy. It is 0 for isotropic interface energy while 4 for anisotropy along 4 directions. θ_0 is a constant which signifies the interface orientation [144] with respect to the maximum anisotropy. δ_ε is the strength of the anisotropy. The value of θ_0 if taken to be zero will allow the interface to grow along the vertical and horizontal directions. The above **equation 3.15** for anisotropy is not valid for highly faceted solidification i.e. for materials having strong anisotropy. Thus since ε is related to the material interface energy (**equation 3.9**), the assumed dependency of ε on θ also relates the material interface energy σ to θ. Formation of solid crystals during solidification takes place in a faceted manner. Solidification of cubic crystals in dendritic mode has been assumed to take place in a weakly anisotropic manner at high undercooling [147]. The anisotropic nature is taken into account by assuming the above relationship which depends on the angle θ between the interface normal and a reference crystalline axis. This anisotropy dictates the preferred growth direction for the dendrites.

The governing equation [134] for solidification of a binary alloy with anisotropy in interface energy is given as

$$\frac{1}{M}\frac{\partial \phi}{\partial t} = \nabla.(\varepsilon(\theta)^2 \nabla\phi) + \frac{\partial}{\partial y}(\varepsilon(\theta)\varepsilon'(\theta)\frac{\partial \phi}{\partial x}) - \frac{\partial}{\partial x}(\varepsilon(\theta)\varepsilon'(\theta)\frac{\partial \phi}{\partial y}) - Wg'(\phi) + h'(\phi)\frac{\mathrm{RT}}{V_m} ln\left(\frac{\left(1 - C_S^{eq}\right)(1 - C_L)}{\left(1 - C_L^{eq}\right)(1 - C_S)}\right) \tag{3.16}$$

where V_m is the molar volume in m^3/mole and R is the universal gas constant. Each point in the computational domain was assumed to be a mixture of solid and liquid phases. The last term on the RHS in the above equation is the thermodynamic driving

force for the solidification of a binary alloy. At the beginning, the concentration of the liquid phase is equal to the initial alloy concentration but with the progress of solidification the thermodynamic driving force decreases.

Under the approximation of dilute solution, the phase-field mobility for a binary alloy [134,140] is given as

$$\frac{1}{M} = \frac{\varepsilon^3 \varsigma\left(C_S^{eq}, C_L^{eq}\right)}{\sigma D_i \sqrt{2W}} + \frac{\varepsilon^2 \beta RT(1-k^{eq})}{\sigma V_m m^{eq}} \tag{3.17}$$

where β is the kinetic coefficient defined [139] to be the inverse of the linear kinetic coefficient [146] μ, k^{eq} is the equilibrium partition coefficient of Carbon in δ-iron, $m^{eq}$is the equilibrium liquidus slope and D_i is the diffusion coefficient in the interface region assumed [140] to be equal to the diffusion coefficient in the liquid. The term $\varsigma(C_S^{eq}, C_L^{eq})$ is given as

$$\varsigma\left(C_S^{eq}, C_L^{eq}\right) = \frac{RT}{V_m}\left(C_L^{eq} - C_S^{eq}\right)^2 \int_0^1 \frac{h(\phi)\left(1-h(\phi)\right)}{\left(1-h(\phi)\right)C_L^{eq}\left(1-C_L^{eq}\right)+h(\phi)C_S^{eq}\left(1-C_S^{eq}\right)} \frac{d\phi}{(1-\phi)} \tag{3.18}$$

The **equation 3.17** permits vanishing kinetic coefficient [134,136] conditions for an infinite value of μ since the value of linear kinetic coefficient is very high [139] in metal systems. Under the vanishing kinetic coefficient condition, the phase-field mobility [142,148] for a binary alloy is given as

$$\frac{1}{M} = \frac{\varepsilon^3 \varsigma\left(C_S^{eq}, C_L^{eq}\right)}{\sigma D_i \sqrt{2W}} \tag{3.19}$$

Taking $h(\phi) = \phi$, Kim et al. [134] modified the **equation 3.16** and showed that the modified version resembles Steinbach's model [138]. The modified equation [134] is given as

$$\frac{1}{M}\frac{\partial \phi}{\partial t} = \nabla.(\varepsilon(\theta)^2 \nabla\phi) + \frac{\partial}{\partial y}(\varepsilon(\theta)\varepsilon'(\theta)\frac{\partial \phi}{\partial x}) - \frac{\partial}{\partial x}(\varepsilon(\theta)\varepsilon'(\theta)\frac{\partial \phi}{\partial y}) - Wg'(\phi) + h'(\phi)\frac{RT(1-k^{eq})}{V_m m^{eq}}(T_m - T - m^{eq}C_L) \quad (3.20)$$

3.2 GOVERNING EQUATIONS for FLUID FLOW

For incompressible fluid flow, the equation for conservation of mass coupled with phase-field model as developed by Steinbach [138] (assuming solid velocity to be zero) is given as

$$\nabla.(1-\phi)\vec{V} = 0 \tag{3.21}$$

and the corresponding equation for conservation of momentum [138] coupled with phase-field model is given as

$$\frac{\partial}{\partial t}\left[(1-\phi)\vec{V}\right] + \nabla.\left[(1-\phi)\vec{V}\vec{V}\right] = -(1-\phi)\nabla P + \nabla.\left[\nu\nabla(1-\phi)\vec{V}\right] - \frac{2.757\nu\phi^2(1-\phi)\vec{V}}{(2\lambda)^2} \tag{3.22}$$

where P is the liquid pressure in m^2/s^2, ν is the constant kinematic viscosity of liquid steel in m^2/s and $\vec{V}$ is the liquid velocity in m/s. The 1st and 2nd terms on left hand side of **equation 3.22** denote the transient term and convection term respectively. The 1st term on the right hand side is the pressure force term and the 2nd term is the diffusion term. The source term due to gravity has been neglected. Putting $\phi = 0$ in the **equation 3.22**, reduces the equation equivalent to solving the Navier-Stokes equation in single phase liquids with constant density and viscosity. Due to increasing solid fraction in the diffuse interface region, the incorporation of the dissipation of the viscous forces in the liquid phase is taken into account through the last term [105] on the right hand side in **equation 3.22**. The dissipative viscous term is proportional to the liquid viscosity and the velocity gradient. While deriving **equation 3.22**, Steinbach [138] assumed that the interface thickness varied over which the phase-field variable varied from 0.05 to 0.95.

3.3 GOVERNING EQUATIONS for SOLUTE TRANSPORT with CONVECTION

As per the author's knowledge, Kim et al. [134] did not extend the original phase-field model (the **equations 3.3** and **3.16**) of solidification to incorporate the solute convection effect. Only a few authors [14,57] who used the solidification model of Kim et al. [134] incorporated the melt convection effect on the solute transport by adding the convection term in the solute transport **equation 3.3** and coupled it with the Navier-Stokes equation. Others [15,16,149] who incorporated the melt convection effect with solidification used the phase-field model developed by Boettinger et al. [137]. As a general case, investigations [13,17,19,150] on the modelling of the melt convection effect on the solidification microstructure have been focussed on the effect of flow magnitude on increased dendrite bending and branching of dendrites in the upstream direction which is primarily due to the asymmetric solute profile ahead of the deflected dendrite. In the present work it was decided to go ahead in coupling the solidification model of Kim et al. [134] with the incompressible phase-field coupled Navier-Stokes equations (**equation 3.21** and **3.22**) as per Steinbach's [138] formulation since there are not much-reported works on melt convection effect using the model of Kim et al. [134]. Incorporating the convection term in the previously stated solute transport **equation 3.3** in the way as done by Steinbach [138] gives

$$\frac{\partial C}{\partial t} = \nabla.\left(D(\phi)\{(1-h(\phi))C_L(1-C_L) + h(\phi)C_S(1-C_S)\}\nabla ln\frac{C_L}{(1-C_L)}\right) - \nabla.\left((1-\phi)\vec{V}C_L\right) \tag{3.23}$$

where the term $(1-\phi)$ is the liquid fraction. The last term signifies that the composition of the liquid phase is advected by the liquid velocity.

The solute transport equation including convection for the modified version of the model of Kim et al. [134] as per Steinbach's formulation can be written as

$$\frac{\partial C}{\partial t} = \nabla.[D(\phi)\nabla \mathrm{C}] + \nabla.(D(\phi)(C_L - C_S)\nabla \phi) - \nabla.\left(\frac{(1-\phi)}{1-\phi+\phi k^{eq}}\vec{V}C\right) \qquad (3.24)$$

3.4 SUMMARY

In a single component system, the temperature profile dictates the phase evolution and hence the chapter starts with the governing equation of temperature. Then comes the case of a solidification of binary alloy in which concentration profile also affects the phase evolution. Following that, the governing equations of phase evolution were discussed. At the end comes the coupling of fluid flow where the fluid flow governing equations and the convection coupled solute transport equations were mentioned.

CHAPTER 4: RESEARCH METHODOLOGY

First part of the chapter gives an overview of the sequence of the steps followed in implementing the numerical model in OpenFOAM from elemental stage. Second part of this chapter initially deals with the methodology followed in conducting the laboratory scale wedge mould casting experiments and collection of industrial grade steel slab samples. Afterwards detailed steps of sample preparation and the various measurements undertaken have been described.

4.1 NUMERICAL METHODOLOGY

The main aim of developing the numerical model is to understand how the presence of bulk fluid flow during solidification affects the solute transport behaviour and thus alters the interface growth direction. Starting with planar solidification in a single component system (pure material), an open source micro scale phase-field method based solidification model, incorporating the thermodynamics of solidification was developed. Simulations were verified for a Fe-C alloy with anisotropic interface energy. Quantitative validation with literature was done for both single component systems and two component systems respectively. Afterwards, the solidification model was coupled with fluid flow. Various stages of the model developed in OpenFOAM have been presented in this section – coupling with an integrated OpenFOAM solver, parallel computing, coupling to Steinbach's model [138] and running the simulations in high performance computing cluster. The necessary modelling parameters, material properties, the initial and boundary conditions to reproduce the same results are tabulated alongside the description.

4.1.1 General Overview about OpenFOAM

OpenFOAM [20] is an open-source computational software used to solve wide range of engineering problems like fluid flow and diffusion. It is written in C++ programming language and runs on Unix / Linux / Windows based operating systems.

It has the advantage of readily available pre-compiled solver codes, known as applications for numerous engineering problems. One of the main advantage of using this software is that any user can port his own code into the latest version in order to be freely available for the benefit of the wider scientific community. OpenFOAM allows a wider range of the collaboration among the audience of the CFD community across the globe than any other commercial software packages. The main components of any CFD software package are – defining the geometry, initial and boundary conditions, solving the governing equations and data interpretation of the numerical results. The blockMesh utility of OpenFOAM generates the computational mesh from the description of blockMeshDict input dictionary. The boundary and initial conditions for the variables to be solved for, are mentioned in another dictionary/file. The physical constants and modelling parameters are stored in the transport properties dictionary. The input data for time control, reading and writing of data are mentioned in controlDict dictionary. OpenFOAM comes with an additional application, called Paraview for post-processing of results.

All the simulations were performed in 2D. The self-written code was used to solve the governing equations. The initial simulations for solidification were performed in the OpenFOAM version 3.0.1 on a Virtual Machine Workstation with configurations of 4GB RAM, processor Intel Core i7 and 3.20 GHz. To start with, the scalarTransportFoam solver in OpenFOAM ver. 2.2.0 was modified and then coupled with phase-field equation to simulate the planar solidification of pure material. Later the developed code was modified as per the requirements and ported to newer versions of OpenFOAM.

4.1.2 Solidification Model

The starting case for developing the solidification model was considered to be that of planar solidification in single component system i.e. pure metal. Initially, the computational domain was considered to be filled with liquid ($\phi = 0$) nickel at the melting point i.e. no undercooling was taken into account. For the solidification without undercooling and anisotropy, the source term of the thermal energy equation (**equation 3.1**) was solved using explicit scheme while rest of the terms were solved by implicit scheme. Similarly, the diffusion term of the phase-field equation (**equation**

3.8) was solved using implicit scheme while the other source terms were solved using explicit scheme. At first the phase-field governing equation was solved and subsequently, the governing equation for temperature was solved. Since the driving force for interface movement is the thermal gradient, the restriction on the time step (Δt) is given as $\Delta t \leq \Delta x^2/4D_T$ where D_T is the thermal diffusivity of the material and Δx is the grid spacing in *x* direction. For the case of solidification with undercooling, the phase-field equation was solved using explicit scheme only. The simulations were performed in a square computational domain of $12\ \mu m \times 12\ \mu m$ with a resolution of 600 grid points each in *x* and *y* directions (equals to 360,000 cells) to ensure visualization of secondary dendrite arms. This resolution was chosen such that the width of the S/L interface could be represented by four grid points. **Table 4.1** and **table 4.2** summarize the model parameters and the material properties for Nickel (Ni) and Iron (Fe) respectively.

Table 4.1: Model parameters for solidification of single component system.

Model parameters	**Ni** [144]	**Fe**
(ε)	2×10^{-4} $J^{-1/2}m^{-1/2}$	1.49×10^{-4} $J^{-1/2}m^{-1/2}$
Free energy factor (W)	0.61×10^{8} Jm^{-3}	0.337×10^{8} Jm^{-3}
(M)	13.47 $m^3s^{-1}J^{-1}$	4.27 $m^3s^{-1}J^{-1}$
Δx	2×10^{-8} m	2×10^{-8} m
Δy	2×10^{-8} m	2×10^{-8} m
Δt	10^{-12} s	10^{-11} s
δ_ε	0.025	0.04

Table 4.2: Material properties for solidification of single component system.

Material properties	**Ni** [144]	**Fe**
σ	0.37 Jm^{-2}	0.204 Jm^{-2} [151]
μ	2 $ms^{-1}K^{-1}$	0.5 $ms^{-1}K^{-1}$ [125]
T_m	1728 K	1811 K [151]
ΔH_m	2.35×10^{9} Jm^{-3}	1.94×10^{9} Jm^{-3} [125]
D_T	1.55×10^{-5} m^2s^{-1}	0.5×10^{-5} m^2s^{-1} [125]
C_p	5.42×10^{6} $Jm^{-3}K^{-1}$	6.35×10^{6} $Jm^{-3}K^{-1}$ [125]
2λ	8×10^{-8} m	8×10^{-8} m

For the initial set of simulations, the domain boundaries were maintained at 300 K. The thermal gradient at the boundary was kept high enough to monitor the movement of the S/L interface within a short time. The phase-field variable was assumed to be equal to 1 at the domain boundaries thereby signifying a layer of solid on the boundary walls to initiate the process of solidification. The simulations were ran for 10^{-7} s. To simulate the effect of undercooling for solidification of nickel, the computational domain was filled with liquid nickel at 1468 K i.e. a degree of undercooling of 260 K. For initial few simulations both the boundary conditions were kept same. But later the boundary condition for temperature was changed to fixed thermal gradient boundary condition. In the literature [144], it was assumed that the region close to the boundaries were at 300 K and was cooled with a heat transfer coefficient of 45 W/m^2K. With a quick calculation, the heat flux was found to be 45× (1468 - 300) = 52560 W/m^2. In the present work it was assumed that the heat being conducted through a solid layer of nickel at the boundary with a thermal conductivity value of 90 W/mK. To have the similar heat flux value of 52560 Wm^2 as reported [144], the calculated thermal gradient on all the boundaries was found to be -584 K/m.

For simulations with anisotropic interface energy, the governing equation for the phase-field variable was **equation 3.13**. The anisotropy constant for pure Ni was taken as 0.025 and the mode of anisotropy as 4 indicating (four-fold symmetry). To simulate the formation of nickel dendrite with well-developed secondary arms in an undercooled melt, the boundary conditions for both the phase-field and temperature were changed to zero flux condition. Solidification was initiated by putting a solid seed at one of the corners of the domain i.e. by putting $\phi = 1$. The seed was allowed to grow with time. Afterwards, the material properties of nickel were replaced by that of pure iron to simulate the formation of iron dendrite in an undercooled melt since the ultimate goal was to simulate a Fe-C dendrite.

To simulate the solidification of Fe-C alloy, initially the chosen alloy was Fe-0.08 wt.% C as this would represent a low carbon steel (grades like AISI 1108, 1010, etc.) that are mainly used in automobile body panels, nuts & bolts, wires and for other structural applications because of good weldability. All the simulations for binary alloy solidification were performed isothermally i.e. under constant undercooling. The numerically solved governing equations were **equations 3.3 - 3.6** and **equation 3.16** respectively. Both the governing equations were solved through the explicit Euler scheme. The computational domain was kept same as before. Since the driving force

for interface movement in binary alloy solidification is the concentration gradient, the time step restriction is given as $\Delta t \leq \Delta x^2/4D_L$ where D_L is the solute diffusivity in the liquid phase. All the equilibrium compositions were taken from Thermo-Calc 2019a software and the material properties were assumed to be independent of composition. A random noise of 1% was applied to the liquid concentration (C_L) at the interface to simulate the formation of secondary dendrite arms. Zero flux boundary conditions were applied for both phase-field and concentration. The solid seed composition was chosen by simultaneously solving **equation 3.5** and **equation 3.6** respectively. **Table 4.3 and table 4.4** summarize the model parameters and the material properties used for the solidification of Fe-0.08 wt.% C alloy respectively.

Table 4.3: Model parameters for solidification of Fe-0.08 wt.% C alloy.

ε	1.05×10^{-4} $J^{-1/2}m^{-1/2}$ [148]
W	0.673×10^{8} Jm^{-3} [148]
M	0.166 $m^3s^{-1}J^{-1}$ [148]
Δx	2×10^{-8} m
Δy	2×10^{-8} m
Δt	10^{-9} s
δ_ε	0.05

Table 4.4: Material properties of Fe-0.08 wt.% C alloy.

σ	0.204 Jm^{-2} [136,139]
D_L	2×10^{-8} m^2s^{-1} [136,139]
D_S	6×10^{-9} m^2s^{-1} [136,139]
V_m	7.7×10^{-6} m^3mole^{-1} [136,139]
R	8.314 $Jmole^{-1}$ K^{-1}
k^{eq}	0.178 [10]
ν	6.79×10^{-7} m^2s^{-1} [57]
T_m	1810 K [136]
2λ	4×10^{-8} m

Later to validate the results qualitatively with literature [136], the alloy composition for the isothermal binary alloy solidification was changed to Fe-0.108 wt.% C (Fe-0.5 mole% C) alloy. The computational domain was chosen as $5\ \mu m \times 10\ \mu m$ with a resolution of 500 grid points in *x* direction and 1000 grid points in *y* direction (equals to 500,000 cells). Thus the grid size was equal to 10^{-8} m in both *x* and *y* directions respectively. The phase-field mobility value was determined under the vanishing kinetics coefficient condition (from **equation 3.19**). The interface width was represented by four grid points. The anisotropy constant δ_ε for interface energy was chosen as 0.03 [136]. As an initial condition, a square box of 5×5 grid points in *x* and *y* directions were put as solid seeds.

For quantitative validation, Kim's extended solidification model based on Steinbach's formulation was used for which the governing equations were **equation 3.7** and **equation 3.20** respectively. The alloy composition was modified to Fe-0.1 wt.% C to validate the secondary dendrite arm spacing data with that of Kim et al. [139]. Kim et al. [139] validated his modelled data against experimental reported results. The width of the domain was taken to about 11 times the length of the reported secondary dendrite arm spacing and the domain height was taken to be around 4.5 times the secondary arm spacing. A mesh size of 0.5 µm was used to calculate the dendrite arm spacing. The interface thickness was represented by eight grid points. No-flux boundary conditions for both phase-field and concentration were used on all sides of the domain. As an initial condition, a uniform thin layer of solid was placed at the bottom of the domain. The effect of cooling rate was implemented in form of the equation $T(t) = T_0 - \Delta T.t$ [139] where T_0 was the initial temperature few degrees below the liquidus temperature of the alloy and ΔT was the cooling rate in K/s. The initial temperature T_0 was taken to be 1800 K for all the cases and only the cooling rate was varied for each simulation. Growth of secondary dendrite arms were simulated at three different cooling rates namely – 83.33 K/s, 33.33 K/s and 8.33 K/s. Simulations were performed for Fe-0.1 wt.% C binary alloy under isothermal conditions with the thermodynamic data taken from Thermo-Calc [10]. **Table 4.5** shows the model parameters used.

Table 4.5: Model parameters for solidification of Fe-0.1 wt.% C alloy.

ε	1.055×10^{-3} $J^{-1/2}m^{-1/2}$ [148]
W	0.673×10^{6} Jm^{-3} [148]
Δx	0.5×10^{-6} m [148]
Δy	0.5×10^{-6} m [148]
Δt	0.25×10^{-5} s
δ_{ε}	0.03 [148]

The variation of the equilibrium solidus and liquidus concentrations as a function of temperature was incorporated using statistical fit equations determined by Wolfram Mathematica 11 [152] numerical software. The respective correlations are given as

$$Equilibrium\ mole\ fraction\ (carbon)\ in\ liquid = (-1.22159 \times 10^{-06} \times T \times T) + (0.00381549 \times T) - 2.90337 \quad (4.1)$$

$$Equilibrium\ mole\ fraction\ (carbon)\ in\ delta\ ferrite\ (solid) = (-1.98848 \times 10^{-07} \times T \times T) + (0.000612082 \times T) - 0.456322 \quad (4.2)$$

The phase-field mobility values at each temperature were determined by numerical integration of **equation 3.18** using MATLAB R2018a [153] software leading to the following correlation as determined by Wolfram Mathematica 11 [152] numerical software

$$\frac{1}{M} = (-0.469462 \times T \times T) + (1494.72 \times T) - 1167210 \quad (4.3)$$

4.1.3 Fluid Flow Coupling

Once the phase-field method based solidification model was developed, coupling of the fluid flow with the solidification model needed step by step modifications. IcoFoam [20] solver is an implemented OpenFOAM solver for incompressible, laminar flow of Newtonian fluids in transient state. In 3D, the **equations 3.21** and **3.22** solve for four unknowns i.e. pressure and the three components of velocity in *x*, *y* & *z* directions. Standard algorithms for solving the equations include [94] SIMPLE (Semi-implicit method of pressure linked equations), PISO (pressure implicit split operator) and PIMPLE (merged PISO-SIMPLE). Detailed description of the various algorithms is given elsewhere [94]. The IcoFoam solver uses the PISO algorithm and the implicit method [94]. The stability criteria [94] that needs to be fulfilled is that the Courant Number (Co) has to be less than 1. Courant number less than one means that instruction from one cell to the adjacent cell in the computational domain should reach within one time-step only. Thus there is a restriction on the time-step size.

All the flow coupled simulations were performed under isothermal conditions. The 1st step in the coupling the fluid flow coupled with solidification model was to couple the IcoFoam solver step by step with the already developed solidification model. As a first case, a small rectangular domain of 10 $\mu m \times 2.2\ \mu m$ with a resolution of 1000 grid points in *x* direction and 220 grid points in *y* direction were taken (equals to 220,000 cells). Liquid steel with initial alloy concentration and a fixed velocity of 0.15 m/s [57] enters the left wall. It exits through the right wall where zero-gradient velocity boundary condition was assumed. The top wall was assumed to move with a fixed velocity of 0.15 m/s in the same direction of the fluid flow. The inside of the domain was assumed to contain full liquid phase equal to initial alloy concentration. Zero velocity and pressure were considered inside the computational domain as initial conditions. Zero pressure gradient was assumed on all domain walls except the right wall where the pressure value was fixed as zero. Solid seed was placed at the centre of the bottom wall and thus under the action of thermodynamic driving force, the seed would tend to grow towards the top wall. The bottom wall of the domain was assumed to be stationary similar to the actual continuous casting mould. Zero flux boundary condition for both concentration and the phase-field variable were assumed on all the domain walls except the left wall. At first, the velocity field was determined by solving the Navier-Stokes equation (**equation 3.21** & **equation 3.22**), followed by solving the

solute transport equation (**equation 3.23**) and then the phase-field **equation 3.16**. At the end, the velocity field at the current time step was multiplied by $(1-\phi)$ i.e. the liquid fraction to get the updated the velocity field for the next time-step. This step meant that the velocity values for each cell were multiplied by the liquid fraction of the corresponding cell. The interface width was represented by four grid points. The modelling parameters ε and W were kept same as shown in **table 4.3**. The anisotropy constant was taken as 0.03 and time step as 10^{-10} s. The flow coupled simulations were run by enabling parallel computing in OpenFOAM. Initially the domain was divided into 3 sub-domains in *x* directions for running the code in parallel with three processers. The initial fluid flow coupled solidification simulations were performed parallel with three processors in OpenFOAM on the Virtual Machine Workstation with 16GB RAM, processor Intel Core i7-7600U and 2.80 GHz. Later the rectangular domain size was increased to $10\ \mu m \times 5\ \mu m$ with a resolution of 1000 grid points in *x* direction and 500 grid points in *y* direction (equals to 500,000 cells).

As a next step of code modification, the extended form of the solidification model developed by Kim was coupled with the Navier-Stokes equation (**equation 3.21** & **3.22**). The corresponding solute transport equation and the phase-field governing equation were **equation 3.24** and **equation 3.20** respectively. To reduce computational time, the domain size was modified to $5\ \mu m \times 2.5\ \mu m$ with a resolution of 500 grid points in *x* direction and 250 grid points in *y* direction (equals to 125,000 cells). The top wall of the domain was taken to be a slip-wall and the bottom wall was taken to be in contact with stationary mould wall ($V = 0$).

Once the flow coupled solidification model was developed, the longer time taking simulations with fluid flow were ran on high-performance computing cluster available at the Centre of Scientific Computing (CSC) Facility at University of Warwick. The CSC department of University of Warwick has two high-performance clusters namely – Tinis and Orac for parallel computing. Batch systems are typically used to run jobs on Linux clusters. With a batch system, jobs are described using a straightforward batch script which is then submitted to a batch queue. To determine the optimum number of processors to run the numerical code in Tinis cluster, the developed flow coupled code was ran under isothermal condition in OpenFOAM 4.1 with different number of processors – 8, 16, 32, 64 and 96 respectively. Rest of the parameters were kept same. Each simulation was executed up to same time instant. **Figure 4.1** shows the plot of total simulation time in seconds against the number of processors. The total

simulation decreases in a steep manner with increase in the number of processors from 8 to 32 after which steepness decreases. From the plot, the optimum number of processors was found to be 64. Total time taken for the simulation with least undercooling was roughly about 24 hours in the high-performance cluster with 64 processors.

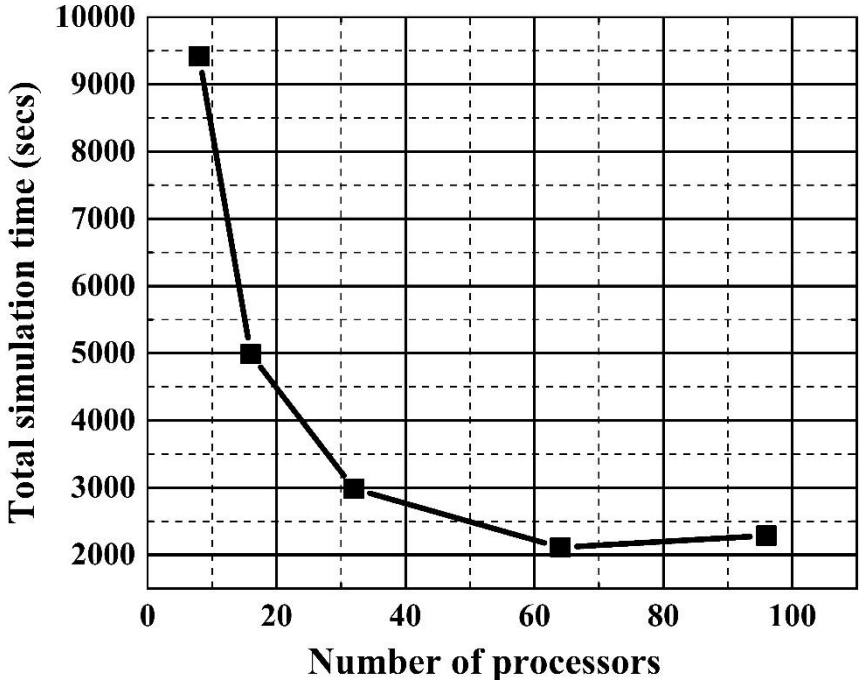

Figure 4.1: Plot of total simulation time against number of processors.

4.2 EXPERIMENTAL METHODOLOGY

The highly competitive market for the production of thinner steel sections demands a diverse product mix to cater to the changing customer needs. It creates a thrust among the casting research community to focus more on the as-cast solidification structure by understanding the linkages between the solidification structure and the casting process parameters. A thorough understanding of the relationship between solidification structure like dendrite arm spacings and the process parameters like fluid flow, casting speed etc. is required to get clear picture of the structure-property correlation of the cast product. This helps in the development of advanced steel grades. Thus, one of the main purposes of doing the experiments was to understand how the

cooling rate influences the solidification structure and hence the macrosegregation in the as-cast product. This was done by performing laboratory scale wedge mould casting experiments.

In the laboratory scale, wedge mould casting experiments without bulk fluid flow were carried out as opposed to the flow in a continuous casting process. Hence to understand the effect of bulk fluid flow on the solidification structure in the cast product, industrial grade steel slab samples produced during a continuous casting process were collected and compared with that of the wedge mould cast samples. Measurements of the dendrite deflection angle in the slab samples and correlating with the macro scale bulk fluid flow profile was performed.

4.2.1 Laboratory Scale Wedge Mould Casting Experiments

The procedure of laboratory-scale wedge mould casting experiments were performed at the Tata Steel Research and Development in IJmuiden, The Netherlands. The whole experimental set-up (**Figure 4.2a**) of the induction furnace and the wedge mould was kept under vacuum during the experiment to protect the liquid steel from oxidation. The wedge mould set-up was an in-house development, designed to study the effect of cooling rate on the as-cast solidification structure and microsegregation phenomena of different advanced high strength steel grades. The idea of having different cooling rates for a single cast in the mould was conceived by making five steps of different thicknesses of the mould gap along the length of the mould. The thickness increases in a step-wise manner from bottom to top thereby allowing liquid steel of different volumes to solidify at different cooling rates. Each step was equipped with a pair of thermocouples. A smaller mould gap will allow a smaller volume of liquid steel to solidify and thereby leads to higher cooling rates. **Figure 4.2b** shows the schematic of the wedge mould of height 340 mm. It can be seen that the mould consisted of five steps with gap thicknesses of 6, 12, 24, 50 and 100 mm respectively.

Each casting experiment was done in the following manner. At the beginning, the vacuum chamber was flushed with argon gas three-four times to remove the traces of air/oxygen. After that, the furnace was switched on. The raw materials used include electrolytic grade iron, pure carbon and manganese, the respective amounts being dependent on the desired chemistry. It takes around 25 – 30 minutes to completely

melt the iron. 50 kgs of melt with the desired chemistry were prepared in vacuum induction furnace. De-oxidation of the melt was done by adding pure aluminum before casting. The oxygen content of the melt was measured by Celox probes both before and after de-oxidation. After the desired casting temperature was reached, a lollypop sample was taken and sent for composition analysis of the melt. Finally, the melt was poured into the wedge mould for casting. The wedge part of the mould was filled from bottom with the thinnest cross-section filling first and more calmly. After the experiment was finished, the mould was allowed to cool down to room temperature. Later, one slice of the cast product along the central plane was cut out for subsequent steps of analysis. **Figure 4.2c** shows such a sample slice from one of the wedge mould casts. It shows that the thickness of the solidified steel increases from bottom to top.

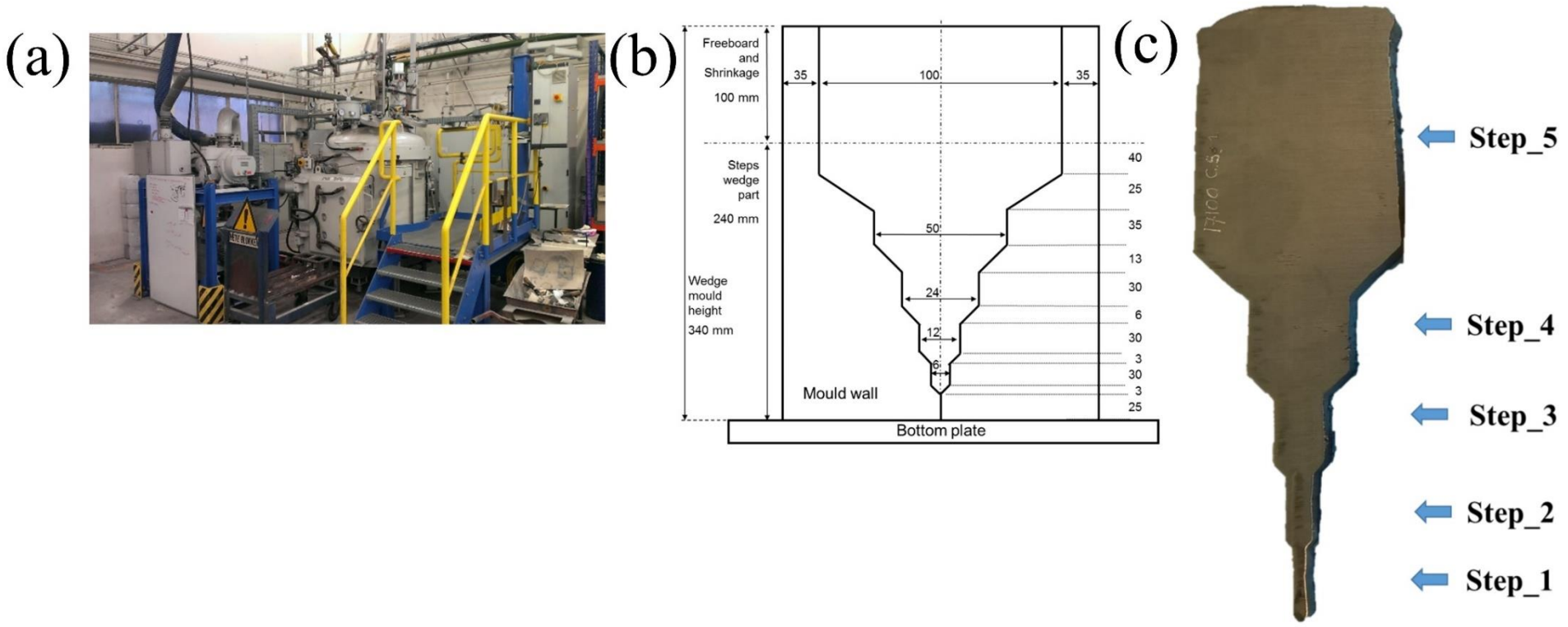

Figure 4.2: Experimental set-up for wedge mould casting experiments; (a) vacuum induction melting set-up; (b) schematic of the wedge mould; (c) slice cut from the wedge mould cast sample.

4.2.2 Collection of Industrial Slab Samples

To understand the effect of bulk fluid flow on the solidification structure, steel slab samples were collected from the conventional slab caster at Tata Steel in IJmuiden, The Netherlands. The comparison of the solidification structure of the laboratory cast samples and the industrial slab caster samples would give a picture of the effect of bulk fluid flow. **Figure 4.3** shows the portion of the slab from where the samples were taken with the sample cutting plane shown as a green broken line.

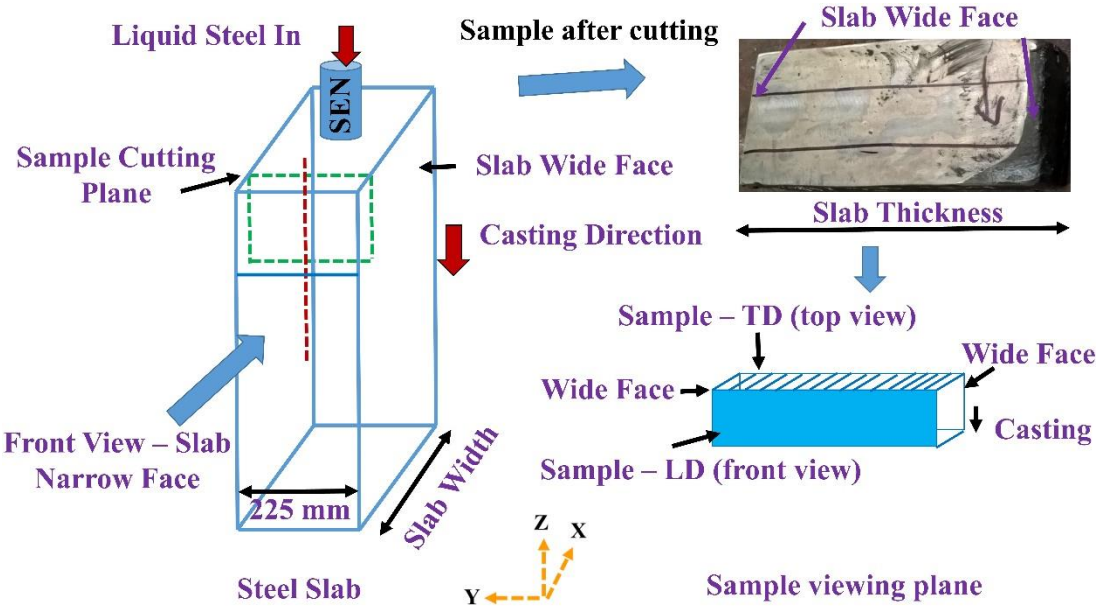

Figure 4.3: Collection and sample preparation scheme for continuously cast steel slab samples.

The casting direction was along *z* direction, *x* direction along the mould width direction and *y* direction was along the slab thickness direction. The sample was cut approximately at a quarter distance inwards from one of the narrow face along the *y* - *z* plane. Thus the sample cutting plane was parallel to the narrow face. The red broken line in **Figure 4.3** shows the slab centreline on the narrow face along the longitudinal direction. Samples after cutting from the slab resembled the one shown on the upper right corner (with two wide faces) which were cut further into small pieces of 35×35×10 mm. The image on the lower right side shows the sample viewing planes.

4.2.3 Sample Preparation and Measurements

Small samples from the collected slabs and sliced samples from the wedge mould casts were mounted as per the standard metallographic procedure [154] so that they could be used for subsequent steps of metallographic sample preparation. Final samples for solidification structure analysis were prepared after coarse grinding and subsequent fine polishing with diamond abrasive particles followed by room temperature etching with Bechet–Beauchard etchant [35,155] to reveal the dendritic structure. The etchant was prepared by adding 17.6 grams of picric acid (solid moistened with 35% water since dry picric acid is hazardous) to 1000 ml of water along with a little amount of soap solution as wetting agent. About 0.5% Teepol solution (sodium alkyl sulphonate) was added as a wetting agent. The wetting agent was added to clear out the surface from the residue of the etchant (reacted particles that come out while etching). Samples were dipped in the etchant solution and the top surface was constantly rubbed with cotton. Etching of the slab samples were challenging as etching times varied for samples of different chemical compositions. After the etching was complete, the etched sample was observed under Leica optical microscope for visualization of the dendritic solidification structure and subsequent measurements of primary and secondary dendrite arm spacing. Dendrite arm spacing for the wedge mould cast and slab samples were measured from one surface towards the opposite direction. **Figure 4.4** below shows two primary dendrites growing perpendicularly to the mould surface. The primary and secondary dendrite arm spacing are designated as λ_1 and λ_2 respectively.

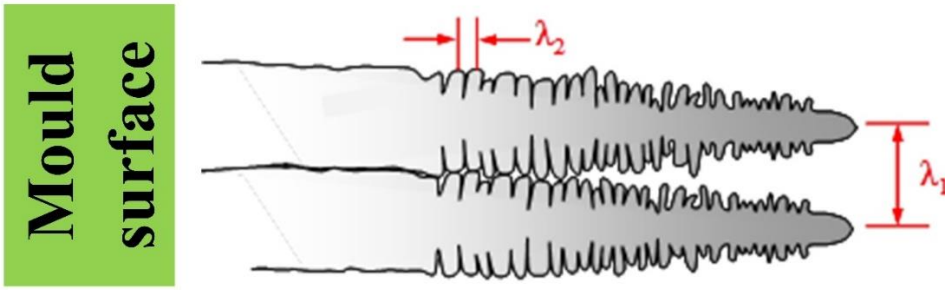

Figure 4.4: Representation of primary and secondary dendrite arm spacing [35].

Dendrites grow in 3D fashion in the cast slab samples. Since it was difficult to measure the bending angle of dendrites in 3D, the microstructure analysis was done in two different planes as shown in **Figure 4.3**. At first, the bending angle and dendrite arm spacing were measured on the plane shown as "Sample_LD" (shown as blue shaded region in **Figure 4.3**) i.e. along the longitudinal direction on the *y*-*z* plane. The bending angle and dendrite arm spacing were also measured on the plane shown as "Sample_TD" (shown as blue hatched region in **Figure 4.3**) i.e. along the transverse direction on the *x*-*y* plane. For both the cases, the measurements were done from the slab surface towards the slab centre. The dendrite deflection angle was measured by individually selecting the dendrites and measuring the height and width of the rectangle with dendrite as the diagonal. **Figure 4.5** shows the convention of measuring the bending angle of a dendrite originating from the mould wall in presence of fluid flow (bending angle denoted as θ). In absence of fluid flow, the dendrites will tend to grow perpendicularly to the mould walls whereas due to bulk fluid flow the dendrites will tend to bend towards the upstream direction as shown in **Figure 4.5**. Starting from the slab surface, the bending angle was measured at perpendicular distances from the surface.

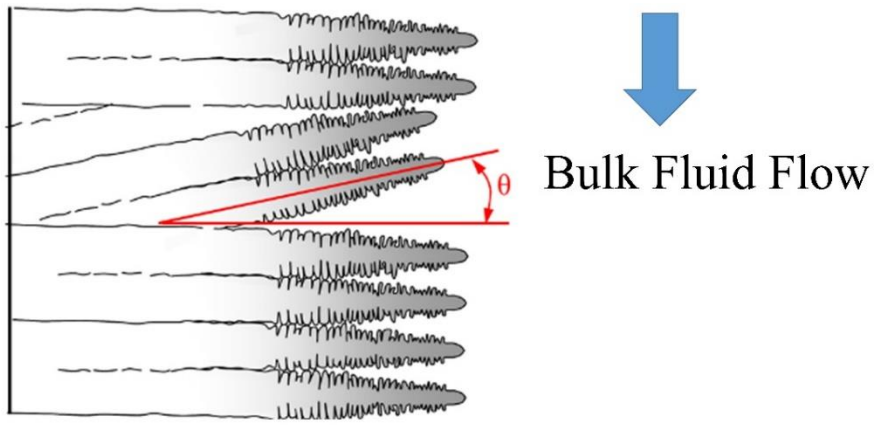

Figure 4.5: Schematic representation of the definition for the bending angle θ [35], used in this study.

4.2.4 Line Scan Analysis by Electron-Probe Micro-Analyser

EPMA technique [79,156] is a widely used technique for quantitative measurement of the concentration of elements across a specimen using the principle of X-ray spectrometry. The EPMA facility at Tata Steel Research and Development in IJmuiden, The Netherlands used for the measurement was Cameca_SX_100 which used the tungsten filament electron source and had five different spectra for analysis. Wavelength dispersive spectrometer (WDS) was used for the quantitative analysis. For any measurement of a particular element, the difference between the generated peak intensity and the background intensity was determined for that element for the test sample. This determined intensity was then compared against the difference of the peak intensity and the background intensity for the same element but on a standard sample of known concentration. The ratio of these intensities is proportional to the concentration of that element in the test specimen. The main objective was to determine the composition profile of various elements in the wedge mould and the steel slab samples. The measurements were done along a straight line (the main line-scan direction) with a fixed interval between successive points. Each measurement point was an average of a line scan of 100 μm length i.e. a line scan in a direction perpendicular to the main line-scan direction. Before the start of the actual measurement, calibration of the respective elements were done as per the standard samples after which measurements were performed on a secondary standard steel sample of known composition. For every measurement of steel samples, the instrument was fed with the additional information that the matrix was iron and stable beam was ensured. For calibration of carbon, carbon contents of several standard samples of known carbon concentration were measured and plotted to get a straight line pattern. Polished bare samples placed in an in-house developed sample holder were used. To minimize the contamination, the carbon analysis was performed for a few seconds. Measurement time for manganese was kept around 20 – 30 s each. The analytical conditions (e.g., accelerating voltage, beam current, etc.) were set at the beginning and maintained throughout the session. Surface to surface analysis for each sample was done at the mid-height portion.

4.3 SUMMARY

In the numerical methodology part, the chapter describes the step by step methodology of the flow coupled solidification model developed in an open source computational software. The modelling parameters, material properties, boundary conditions and domain size used to get the results (discussed in the next chapter) were mentioned. Also, for the case of validation for a binary alloy, the mobility variation was expressed as a function of temperature rather than used as a constant. Optimum number of processors for running the flow coupled simulations in the high performance cluster were also discussed. On the experimental side, initially the methodology of laboratory scale wedge mould casting experiments were discussed. Following that how the industrial slab samples were collected and the detailed steps of experimental measurements were discussed. The results related to solidification structure analysis and composition profile measurements have been discussed in the next chapter.

CHAPTER 5: EFFECT OF FLUID FLOW ON INTERFACE GROWTH BEHAVIOUR: MICRO SCALE

First part of the chapter deals with the modelling and experimental results without fluid flow. The initial part with reference to the single component system describes the interface movement as a function of thermal undercooling and the effect of random noise. To begin with, the material chosen was pure nickel and latter the material properties were changed to that of pure iron. For the case of Fe-C binary system, the interface movement leads to solute pile-up ahead of the interface. On the experimental side, results pertaining to the solidification structure and segregation ratio for wedge mould cast alloys were discussed. Lastly, the solidification model was coupled to fluid flow and the results related to the change in interface growth direction due to fluid flow were discussed.

5.1 SOLIDIFICATION without FLUID FLOW

The initial numerical modelling results deal with how the flow decoupled solidification model was built starting from the planar interface solidification in single component system. Results pertaining to step by step modifications of the model (like changing the boundary conditions, governing equations, domain size, alloy etc.) up to the state of binary alloy solidification under different conditions have been shown. Later the experimental results on wedge mould cast ingots (without bulk fluid flow) were compared with the modelling results.

5.1.1 Solidification of Single Component System

Figures 5.1 shows the phase-field and temperature profiles for solidification of pure nickel without undercooling. The total simulation run time corresponding to the solidification time of 10^{-7} s was 8.5 hrs with single processor. This simulation run time

seems to be reasonably high. It has already been stated that phase-field simulations are computationally intensive due to fine mesh size. But one can reduce the computation time through parallel computing, code optimization, adaptive meshing and so on. The red colour code in the phase-field profile signifies solid phase and the blue colour code signifies liquid phase. The domain was cooled from its walls simultaneously. Solidification occurs from the walls and the S/L interface grows inward. The interface between the pure solid and pure liquid region is sharp. The stable S/L interface moves in a planar fashion opposite to the heat extraction direction in a non-undercooled melt. The latent heat generated at the interface being removed continuously through the evolving solid phase and finally through the boundaries. In the core liquid region, the temperature is uniform at the melting point whereas it decreases away from the interface in the solid region. **Figure 5.2** shows the plot of interface velocity with time. Initially, the interface velocity is highest and then it decreases exponentially as the thermodynamic driving force for interface movement decreases.

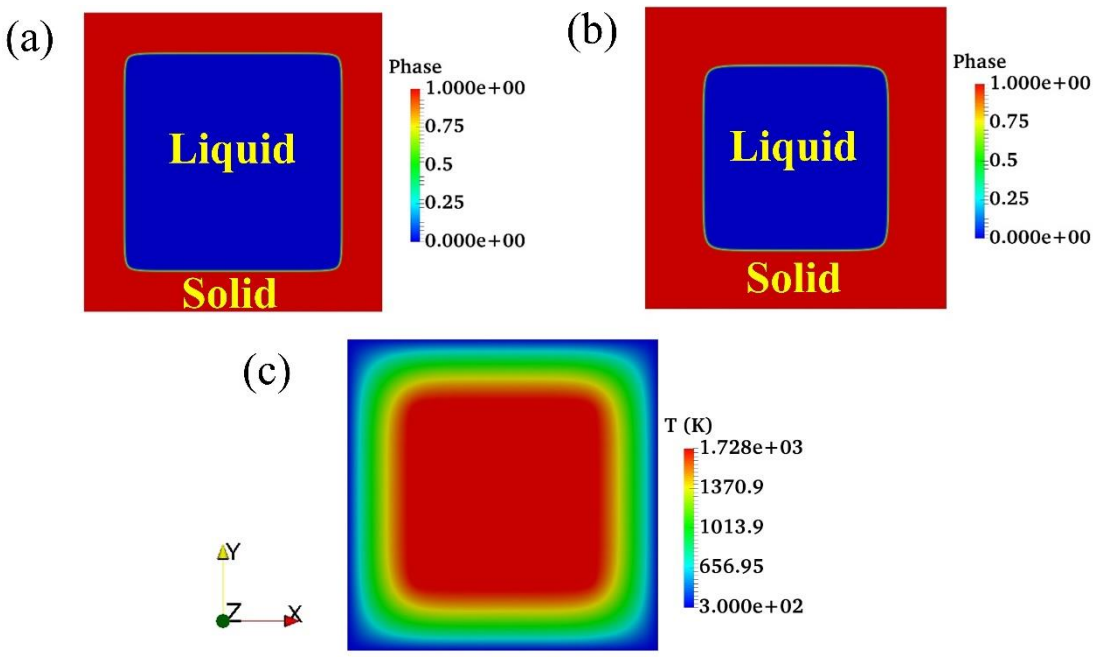

Figure 5.1: Planar S/L interface for solidification of pure Nickel without undercooling in a $12\ \mu m \times 12\ \mu m$ domain with 360,000 cells; (a) phase-field profile at time 5×10^{-8} s; (b) phase-field profile at time 10^{-7} s; (c) temperature profile at time 10^{-7} s.

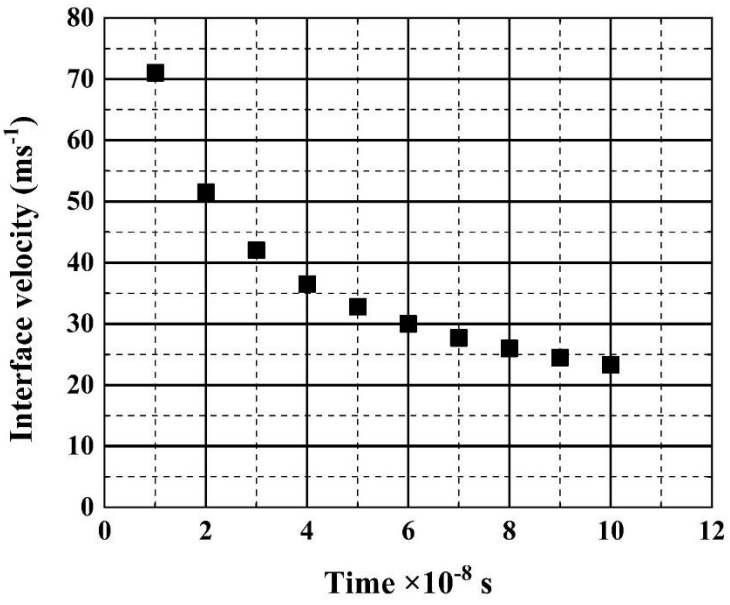

Figure 5.2: Variation of S/L interface velocity with time for solidification of pure Ni without undercooling.

Figure 5.3 shows the effect of random noise on the S/L interface profile for solidification of nickel at an undercooling of 260 K at $t = 10^{-7}$ s. **Figure 5.3a** shows the interface profile without random noise. Due to the undercooling effect, the S/L interface becomes unstable and hence it shows a curvature. Portion of the interface moves faster than other portions thereby rendering a degree of non-uniformity in the movement of the solidification front. **Figure 5.3b** shows the interface profile with 1% random noise on the latent heat and **Figure 5.3c** shows the interface profile with 1% random noise on the total driving force i.e. the double well potential and the terms involving degree of undercooling in **equation 3.8** respectively. Similarly **Figure 5.3d** shows the interface profile with 1% random thermal noise. Thus it can be observed that only in the case of thermal noise, the interface instabilities get reflected. Noise on other terms was not enough to create random interface instabilities. The boundary conditions were kept same.

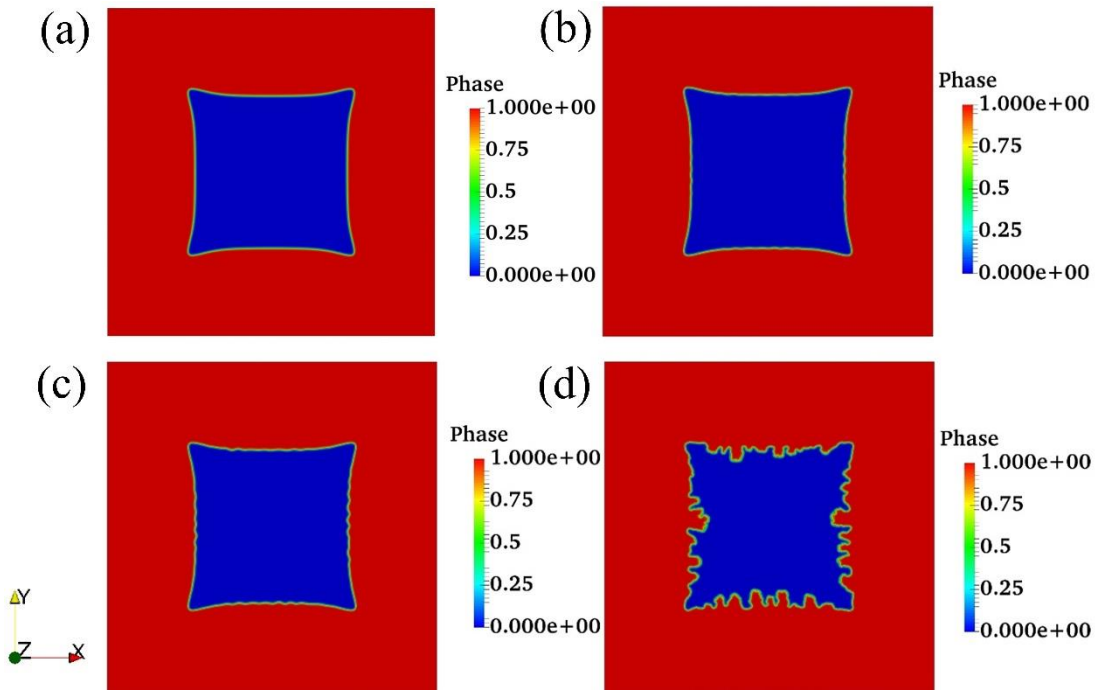

Figure 5.3: Effect of random noise on the S/L interface profile for solidification of nickel with an undercooling of 260 K in a 12 $\mu m \times 12\ \mu m$ domain with 360,000 cells at time 10^{-7} s; (a) without noise; (b) with 1% random noise on latent heat; (c) with 2.5% random noise on total driving force; (d) with 1% random thermal noise.

Figure 5.4 shows the effect of anisotropy on the interface profile for solidification of nickel at an undercooling of 260 K. The thermal boundary condition being kept to fixed gradient at -584 K/m. **Figure 5.4a** shows the interface profile without random noise. The domain corners solidify slowly due to greater release of latent heat and thereby reducing the degree of heat extraction. With the addition of random thermal noise (**Figure 5.4b**), the interface instabilities gets magnified giving rise to interface splitting with random curvatures. Portions of the interface progressed fast, overruling other portions which were found to be lagging behind. Kobayashi [133] also observed similar kind of tip splitting in case of directional solidification with isotropic interface energy in an undercooled melt. Presence of thermal noise aggravates the interface instabilities and gives rise to protrusions along the interface which moves faster compared to other regions. Towards the end of the solidification, these protrusions will give rise to formation of primary dendritic arms. In presence of anisotropy in interface energy, branching of these protrusions will give rise to formation of secondary dendrite arms. For the case of solidification with anisotropic interface

energy, the interface energy was assumed to be maximum in horizontal and vertical directions i.e. $\theta_0 = 0$. **Figure 5.4c** shows the interface profile with 1% random thermal noise and anisotropic interface energy at 8×10^{-8} s (simulation time 7 hrs). It can be seen that the previously observed random interface structures in **Figure 5.4b** get oriented in *x* and *y* directions. The interface instabilities gave rise to the growth of well-developed primary dendritic arms in horizontal and vertical directions which were the directions of maximum anisotropy. The S/L interface growing from opposite walls advances towards each other against the direction of heat extraction. The growing interfaces then would finally meet at the centre at the end of solidification. Kinks can be seen on the periphery of some of the primary dendrite arms which will give rise to secondary dendrite arms. The growth rates of the primary dendrite arms were faster compared to the interface structures in **Figure 5.4b**. It can be seen that the present result of the growth of primary dendrites agrees well with the published literature as shown in **Figure 5.4d**. The domain size (as well as the grid spacing) and the time step size used in the present calculation were same corresponding to the **Figure 5.4d**.

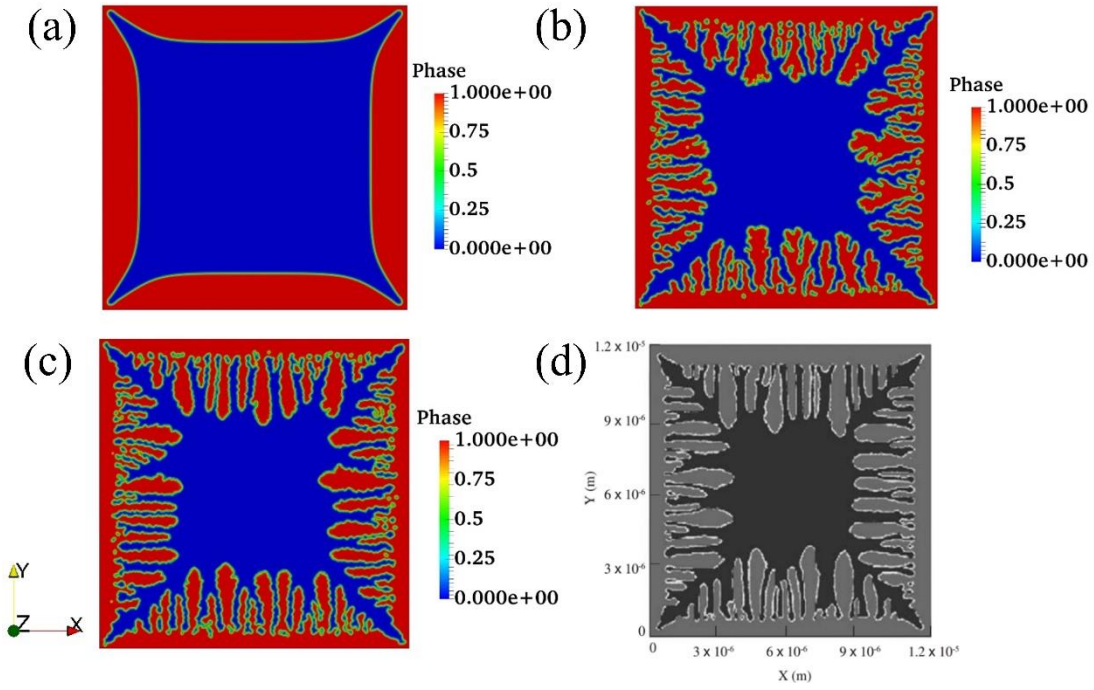

Figure 5.4: Effect of anisotropy on the S/L interface profile for solidification of nickel with undercooling of 260 K in a $12\ \mu m \times 12\ \mu m$ domain with 360,000 cells; (a) without noise and anisotropy at time 10^{-7} s; (b) with 1% random thermal noise but without anisotropy at time 10^{-7} s; (c) with 1% random thermal noise and anisotropy at time 8×10^{-8} s; (d) with 2.5% random noise and anisotropy [144] at time 7.5×10^{-8} s.

Figure 5.5 shows a pure nickel dendrite with well-developed secondary arms growing into an undercooled melt at 2×10^{-7} s (simulation time 19.5 hrs) and its comparison with literature [144]. By putting $\theta_0 = 45^0$ in the **equation 3.15**, the tip of the primary dendrite (in **Figure 5.5a**) was found to be growing at an angle of 45° with the horizontal. Both secondary dendrite arms and some tertiary dendrite arms were found to grow. Higher degree of randomness of the secondary and tertiary arms might be due to the high degree of random noise applied which was 1% of the temperature field. Since the melting point of nickel is 1728 K, maximum variation in temperature as per the applied thermal noise will be 1% of 1728 K ≈ 17.28 K. Thus the maximum temperature will be 1728 K + 17.28 K = 1745.28 K. Temperature fluctuations of this much magnitude is reasonably high. **Figure 5.5b** shows the thermal field distribution corresponding to **Figure 5.5a** and **Figure 5.5c** shows the thermal field distribution from literature [144]. It can be observed that the tip of the primary arm moves into the undercooled melt at 1468 K. The thermal field for the present work qualitatively agrees well with the literature [144]. The thermal diffusivity for pure Nickel in the energy transport **equation 3.1** is 1.55×10^{-5} m^2/s while the term corresponding to thermal diffusivity for pure Nickel in the phase-field governing **equation 3.13** is $M\varepsilon^2$ which is around 27.07×10^{-8} m^2/s. Since (D_T) >> $M\varepsilon^2$, it is the thermal field which remains ahead of the S/L interface and drives the movement of the interface. It is this thermal gradient which stabilizes the formation of interface instabilities resulting in secondary and tertiary dendrite arms.

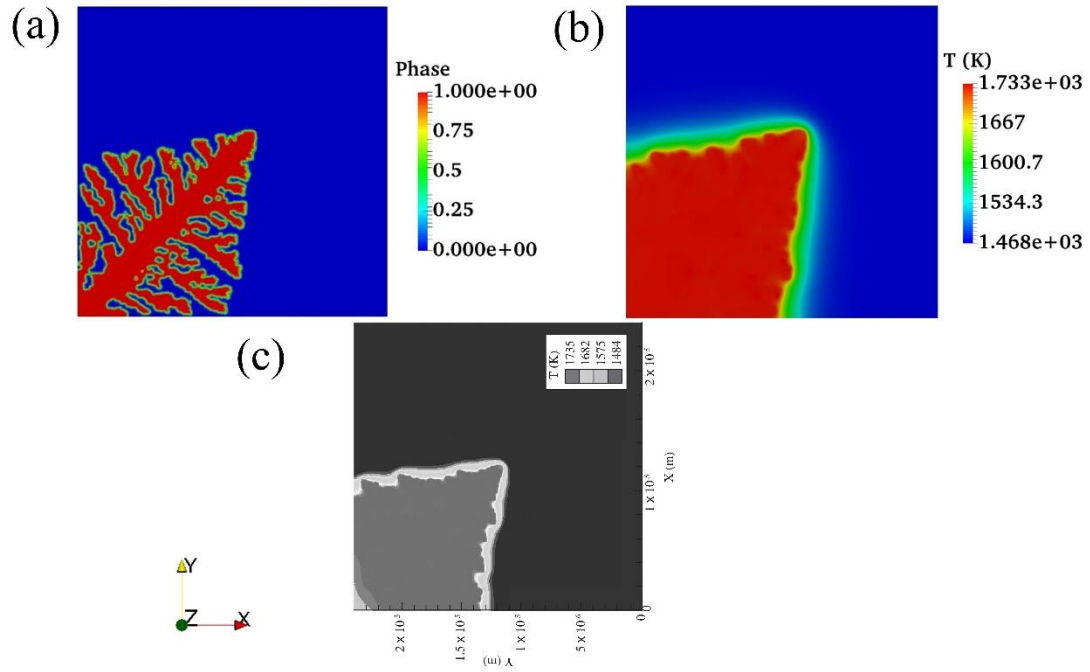

Figure 5.5: Formation of nickel dendrite in an undercooled melt (260 K) in a 12 μm × 12 μm domain with 360,000 cells at 2×10^{-7} s; (a) phase-field profile; (b) temperature profile in present work; (c) temperature profile [144].

Figure 5.6 shows the phase-field profile of iron dendrite growing into an undercooled melt at 1551K (degree of undercooling being 260 K). **Figure 5.6a** shows the effect of 1% random thermal noise. It can be seen that growth rate of the interface for iron is less than that of nickel. This is because iron has lower value of interface kinetics coefficient and lower thermal diffusivity than nickel. Hence the dendrite tip for nickel is sharper than that of iron. Also, the number of secondary dendrite arms is less for iron. **Figure 5.6b** shows the iron dendrite with 0.5% random thermal noise. With decrease in amplitude of random noise term, the interface becomes smoother. **Figure 5.6c** shows the profile of iron dendrite with 2.5% noise on the total driving force including the double-well potential as followed by [137]. The total driving force including the double-well potential is of the order of 10^8 J/m^3, 1% of which corresponds to of the order of 10^6 J/m^3. Thus the maximum driving force including the fluctuation will be around ~ 1.01×10^8 J/m^3 (10^8 + 10^6) which is almost same as the one without fluctuation. Thus the magnitude of fluctuations were much less when the noise was applied over the total driving force compared to the case of thermal noise.

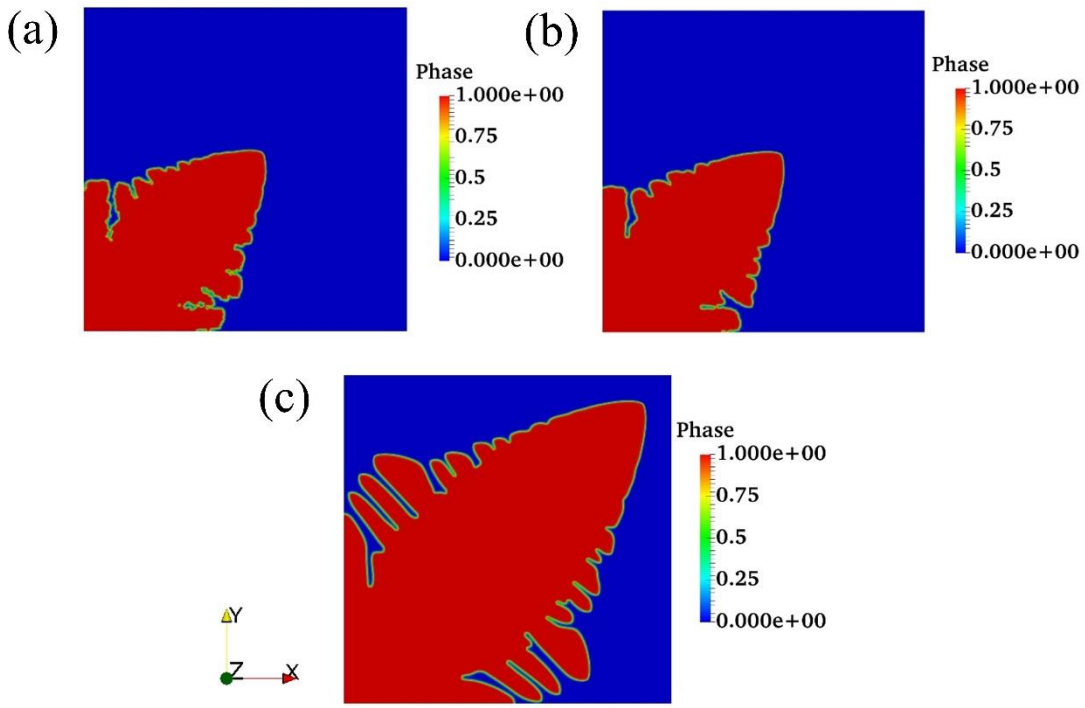

Figure 5.6: Formation of iron dendrite in an undercooled melt (260 K) in a 12 μm × 12 μm domain with 360,000 cells with different magnitudes of random noise; (a) phase-field profile at 6×10^{-7} s with 1% random thermal noise; (b) phase-field profile at 6×10^{-7} s with 0.5% random thermal noise; (c) phase-field profile at 10^{-6} s with 2.5% random noise on total driving force.

Effect of undercooling on dendrite tip growth speed for pure Ni (validation)

For quantitative validation with literature [144], the simulation for solidification of pure Nickel was run at different degrees of undercooling from 60 K – 160 K and the primary dendrite tip growth rate was measured at different time instants. 2.5% of random noise was applied on the total driving force term in the phase-field **equation 3.13**. The parameters were kept same as followed in literature [144]. **Figure 5.7** shows the plot of the variation in tip growth rates with undercooling. The black points were retrieved from literature [144]. It is to be noted that Ferreira et al. [144] in his work validated the modelled results with experimental results. The modelled results obtained by Ferreira et al. [144] were very close to the experimental ones, especially at higher degree of undercooling. At the initial time instant, tip growth rate was quite high. At the next time instant of 1.2×10^{-08} s, there was a sharp drop in the tip growth

rate. This drop in tip growth rates with successive time instants decreased with time. It can be observed that for each degree of undercooling, the tip growth rate decreased with increase in time. This was due to high driving force at the beginning and it decreased with time for each degree of undercooling. Also higher undercooling means higher driving force. Hence with decrease in undercooling, the thermodynamic driving force decreased and hence the tip growth rates also decreased. This decrease of tip growth rate followed an approximate linear path. This is because of the assumed constant linear kinetic coefficient. The variation in tip growth rates with undercooling at 1.6×10^{-08} s in **Figure 5.7** closely matches well with the literature [144].

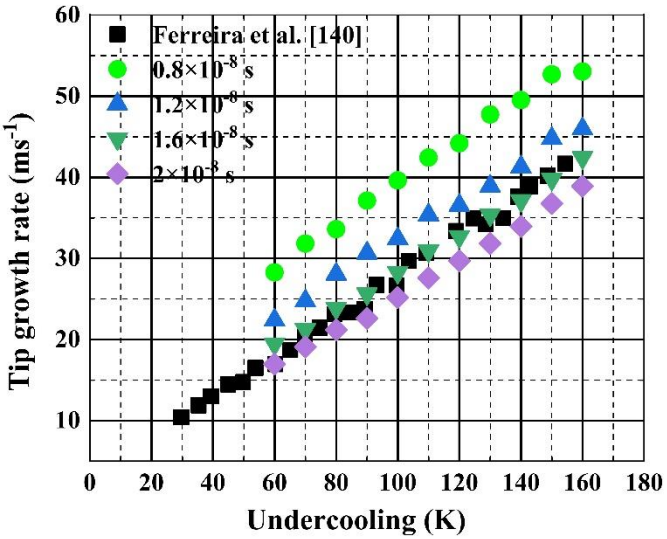

Figure 5.7: Variation of primary dendrite tip growth rate for solidification of pure Nickel at different time instants for each degree of undercooling and its comparison with literature [144].

5.1.2 Solidification of Two Component (Binary) System

For the isothermal (constant temperature) solidification of Fe-0.08 wt.% C alloy at 1801 K, the phase-field mobility was taken from literature [148] which was for a very low carbon Fe-C alloy. The primary dendrite was allowed to grow at an angle of 45° to the horizontal. The secondary dendrites were found to grow perpendicularly to the primary arms. The equilibrium compositions as determined from Thermo-Calc 2019a

software [10] were $C_S^{eq} = 0.023$ wt.% C and $C_L^{eq} = 0.129$ wt.% C respectively. **Figure 5.8a** and **Figure 5.8b** show the dendrite of Fe-0.08 wt.% C alloy under isothermal (1801 K) solidification condition at 0.0001 s. **Figure 5.8c** and **Figure 5.8d** show the comparison of the phase-field profile and the carbon concentration profile across the S/L interface in the present work (Fe-0.08 wt.% C alloy) with literature [148] (Fe-6.93×10^{-3} mole% C alloy). The total simulation time was 11.5 hrs. The composition of the solid and liquid phases at the S/L interface was close to the respective equilibrium compositions as governed by the assumption of local equilibrium at the interface. The composition of the bulk liquid far away from the S/L interface was 0.08 wt.% C which was equal to the initial alloy composition. As we all know that during the solidification of a binary alloy, the solidifying phase continuously rejects the excess solute into the bulk liquid ahead of the interface. This leads to pile-up of the solute ahead of the S/L interface which increases with time. This is called microsegregation i.e. non-uniformity of chemical composition in micro scale. One can observe (**Figure 5.8b**) the solute microsegregation ahead of the interface where the maximum solute concentration was almost 1.5 times the initial alloy composition. Thus one can see that the liquid concentration just ahead of the S/L interface was highest and it exponentially decays down to the bulk liquid concentration as one goes away from the interface into the bulk liquid leading to formation of diffusion boundary layer. The carbon diffusion layer is always ahead of the S/L interface due to larger diffusivity compared to the phase and thus drives the movement of the interface. With the progress of solidification the tip of the primary dendrite (or the S/L interface) would move forward in a continuous manner with time. Hence the solute rejection ahead of the interface will increase and the solute build up layer will get continuously pushed in the direction of interface movement.

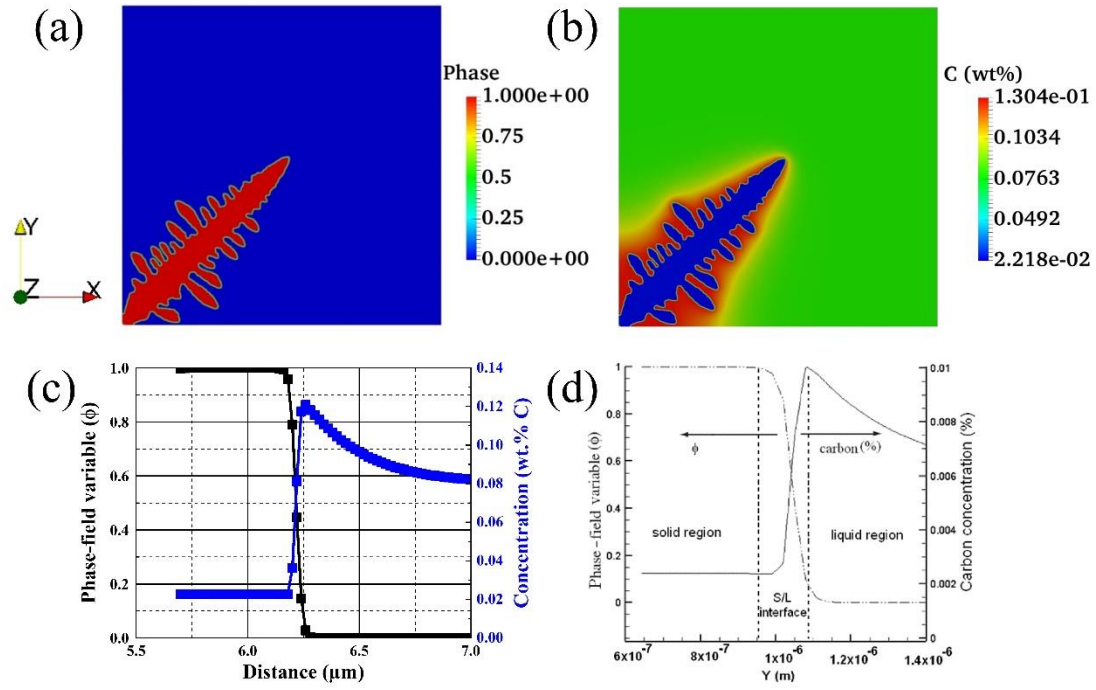

Figure 5.8: Isothermal (1801 K) solidification of Fe-0.08 wt.% C alloy at 0.0001 s and the similarity of the phase-field profile as well as concentration profile across the S/L interface for the present work with literature [148]; (a) phase-field profile; (b) carbon concentration profile (microsegregation); (c) phase-field profile and concentration profile across the S/L interface for the present work; (d) phase-field profile and concentration profile across the S/L interface in literature [148] for isothermal solidification of Fe-6.93×10^{-3} mole% C alloy.

Figure 5.9a and **Figure 5.9b** show the phase-field profile for isothermal solidification of Fe-0.108 wt.% C (Fe-0.5 mole% C) alloy at 1780 K where the interpolating functions were chosen as $\phi^3(10-15\phi+6\phi^2)$ and $\phi^2(3-2\phi)$ respectively. Since both the images were symmetric, simulations were done for half the dendrite only (for which the domain size was $5\ \mu m \times 10\ \mu m$). The simulation time corresponding to **Figure 5.9a** was 1.6 hrs approximately. The equilibrium mole fractions were taken from Thermo-Calc software [10]. The corresponding phase-field mobility values were 1.689 and 1.33 (m^3/sJ) respectively under the vanishing kinetic coefficient condition. **Figure 5.9c** shows the phase-field profile for isothermal solidification of the same alloy at same temperature taken from literature [136] with $h(\phi)=\phi^2(3-2\phi)$. Both **Figure 5.9a** and **5.9b** match qualitatively well with **Figure 5.9c** in the literature [136]. Comparing both **Figure 5.9a** and **5.9b**, it can be observed that the dendrite tip velocity

and the number of secondary dendrite arms were higher in the phase-field profile with interpolating function as $\phi^2(3-2\phi)$. In the phase-field governing equation, the thermodynamic driving force term was multiplied by the derivative of the interpolating function i.e. $h'(\phi)$. **Figure 5.9d** shows the plot of the derivative of both the interpolating functions i.e. $h'(\phi)$ with the phase-field variable ϕ. It can be seen that outside the interface ($0.1 \leq \phi \leq 0.9$) region i.e. in the bulk solid or liquid phases, the magnitude of $h'(\phi)$ is more when $h(\phi) = \phi^2(3-2\phi)$ than when $h(\phi) = \phi^3\left(10-15\phi+6\phi^2\right)$. Also, the volume fraction of each of the bulk phases being much more than the volume covered by the interface width. This makes the average thermodynamic driving force higher when $h(\phi) = \phi^2(3-2\phi)$ and thus may give rise to higher dendrite tip growth rate and secondary dendrite arms.

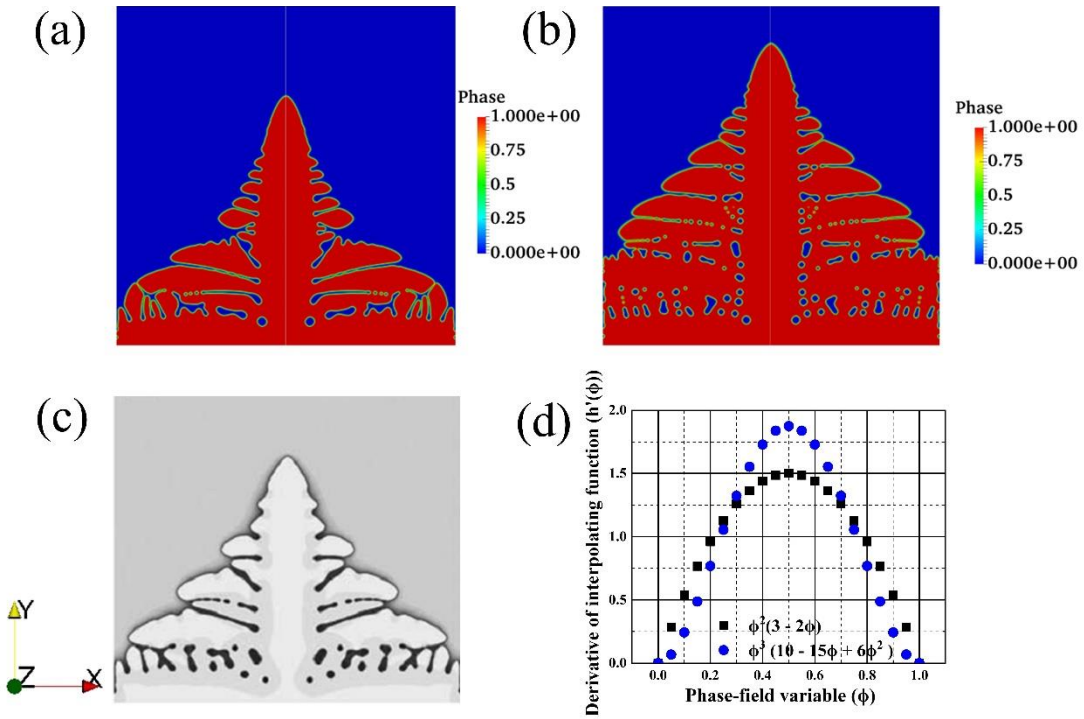

Figure 5.9: Effect of the interpolating function $h(\phi)$ on isothermal (1780 K) solidification of Fe-0.108 wt.% C alloy; (a) phase-field profile with $h(\phi) = \phi^3(10-15\phi+6\phi^2)$; (b) phase-field profile with $h(\phi) = \phi^2(3-2\phi)$; (c) phase-field profile with $h(\phi) = \phi^2(3-2\phi)$ in literature [136]; (d) variation of the derivative of the interpolating functions.

To understand the effect of carbon content, simulations were performed with Fe-C alloys of different carbon contents with same degree (87%) of solid super saturation. **Figure 5.10** shows the dendrite profiles for isothermal solidification of the alloys at 10^{-5} s. **Figure 5.10a** shows the concentration profile for Fe-0.06 wt.% C (Fe-0.3 mole% C) alloy, **Figure 5.10b** that of Fe-0.108 wt.% C (Fe-0.5 mole% C) alloy and **Figure 5.10c** that of Fe-0.13 wt.% C (Fe-0.6 mole% C) alloy respectively. The solute build up layer ahead of the S/L interface can be seen. With the increase of carbon content, thermodynamic driving force increases giving rise to higher growth rate and more number of secondary dendrite arms. Hence the degree of microsegregation also increases.

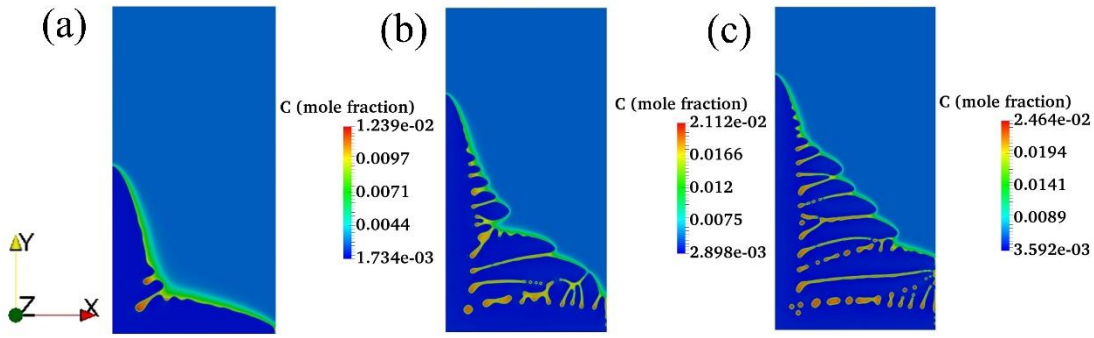

Figure 5.10: Effect of carbon content with same degree (87%) of solid super saturation on the dendrite profile for isothermal solidification at 10^{-5} s; (a) Fe-0.06 wt.% C (Fe-0.3 mole% C) alloy at 1792.9 K; (b) Fe-0.108 wt.% C (Fe-0.5 mole% C) alloy at 1780 K; (c) Fe-0.13 wt.% C (Fe-0.6 mole% C) alloy at 1773.4 K.

Figure 5.11 shows the comparison of the phase-field profile for isothermal (1780 K) solidification of Fe-0.108 wt.% C (Fe-0.5 mole% C) alloy at same time instant using two different models of Kim. **Figure 5.11a** is for Kim's original model [134] while **Figure 5.11b** is for Kim's modified version [134] as per Steinbach's formulation. The dendrite profiles looked very similar except the growth rate was relatively high in **Figure 5.11a**.

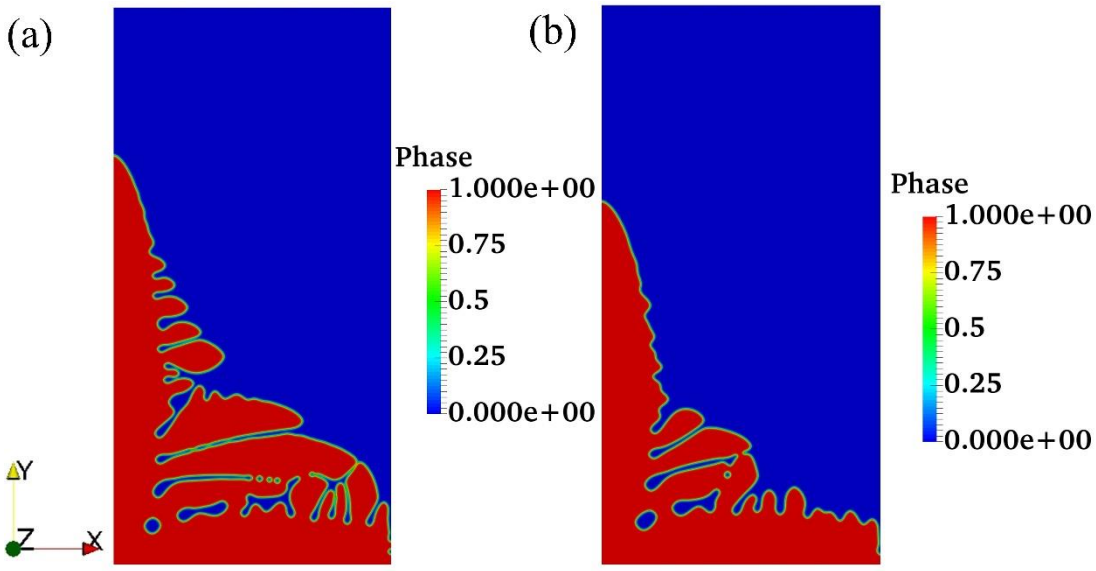

Figure 5.11: Comparison of the dendrite profile for isothermal (1780 K) solidification of Fe-0.108 wt.% C (Fe-0.5 mole% C alloy); (a) Kim's original model; (b) Kim's modified model as per Steinbach's formulation.

Effect of cooling rate on secondary dendrite arm spacing (validation)

Figure 5.12 shows the evolution of the secondary dendrite arms for the Fe-0.1 wt.% C alloy at different time instants obtained in the present work and the comparison of secondary dendrite arm spacing data as a function of cooling rate with literature [139]. **Figure 5.12a** and **5.12b** show the phase-field profile of the growth of secondary dendrite arms and their coarsening behaviour at two different time instants (t_1 and t_2) which is in good agreement as shown in literature [139]. The solid phase is represented by when the phase-field variable takes the value of 1 (colour code "red") while the liquid phase is represented as the value 0 (colour code "blue"). The interface region surrounding the growing solid is quite wide because of the coarser mesh size used though there is evidence of entrapped inter-dendritic liquid in between successive secondary arms. Some secondary arms grow preferably while some arms stop moving forward thereby giving rise to coarsening of the selected arms. **Figure 5.12c** shows the comparison of the secondary dendrite arm spacing data between literature and the present work as a function of cooling rates. It is to be noted that the model results reported in literature by Kim et al. [139] agreed well with the experimental data. The predicted behaviour of secondary dendrite arm spacing with cooling rate follows the

similar quantitative trend as reported [139]. Also the secondary dendrite arm spacing variation falls in the similar range as predicted by Suzuki et al. in **fig. 2.10** [46]. The modelled secondary dendrite arm spacing depends on the thermodynamic parameters used in the system [139] like equilibrium partitioning coefficient, liquidus slope etc. In the present work, both the liquidus slope and the equilibrium partitioning coefficients along with the phase-field mobility were put as a function of temperature as opposed to constant values used in literature [139]. Also, the initial temperature taken in the work was a few degrees below the liquidus temperature. That is why maybe there is a difference in the secondary dendrite arm spacing values shown in the **Figure 5.12c** as compared to that in literature [139]. Also, the predicted exponent value of 0.45 was close to that of 0.48 as obtained in literature [139].

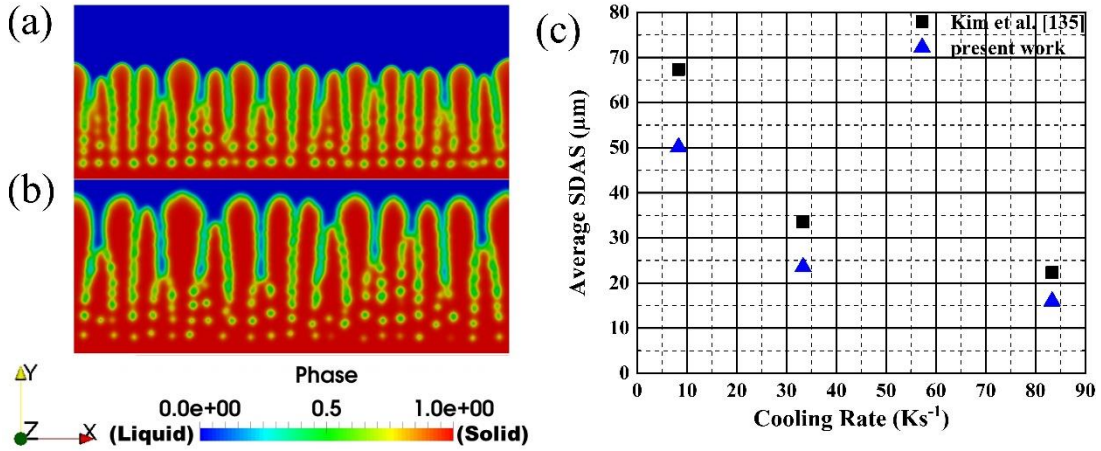

Figure 5.12: Evolution of secondary dendrite arms for Fe-0.1 wt.% C alloy; (a) phase-field profile at time t_1; (b) phase-field profile at a later time t_2; (c) prediction of SDAS as a function of cooling rate and comparison with Kim et al. [139].

5.1.3 Wedge Mould Casting Experiments of Binary Alloys and Complex Ternary Alloy

a) Chemical composition

In order to understand the effect of cooling rate on the dendritic solidification structure, the following alloys in **table 5.1** were cast in the wedge mould. The 1st alloy had chemical composition of Fe-0.12 wt.% C since the modelled secondary dendrite arm spacing data was available for Fe-0.1 wt.% C alloy. But the solidification structure couldn't be resolved for the Fe-0.12 wt.% C alloy. Hence the 2nd alloy had higher carbon content of 0.26 wt.%. Other than carbon, manganese is the most common alloying element in steels (considering sulphur and phosphorous to be impurities). The 3rd alloy was also a binary alloy with chemical composition of Fe-5.8 wt.% Mn. The higher manganese content was chosen to give a wider solidification range. The 4th alloy had chemical composition similar to that of one of the industrial (with bulk fluid flow) slab samples. This sample was selected to enable comparison between the solidification structure of the industrial sample with that of the wedge mould cast ingots of similar chemistry.

Table 5.1: Chemical composition of the wedge mould cast grades.

Cast No.	C, wt.%	Mn, wt.%
1	0.12	0.0
2	0.26	0.0
3	0.0	5.8
4	0.149	0.995

b) Solidification structure and dendrite arm spacing measurements

Figure 5.13 shows the dendritic solidification structure at the centre of step_3 for Fe-5.8 wt.% Mn alloy. Both primary and secondary dendrite arms can be seen. In the previous section on solidification of two-component system, formation of primary and

secondary dendrite arms has already been shown for solidification of Fe-C alloys. In **Figure 5.13** secondary dendritic arms were seen to grow parallel to the mould wall (which was parallel to the left / right side of the image) and perpendicular to the primary heat extraction direction across the mould wall. As soon as the liquid steel comes in contact with the mould walls, it will start to solidify. Since the primary heat extraction direction was perpendicular to the mould walls, the S/L interface from the both surfaces would move towards each other perpendicular to the mould walls. Assuming equal heat extraction behaviour on the both the surface, both the interfaces will meet at the centreline. The marked centreline (white broken line) in **Figure 5.13** shows the demarcation line where the primary dendrite arms growing from the opposite sides meet each other. The marked centreline is not exactly at the image centre. This is because the original image was cropped to remove the defocussed areas. Similar phenomenon (in **Figure 5.4c)** of the movement of the S/L interface against the heat extraction direction was shown earlier for single component system as well. In **Figure 5.4c**, the tip of the primary dendrites moved towards each other against the heat flow direction and at a certain time instant they would meet exactly at the centre of the domain.

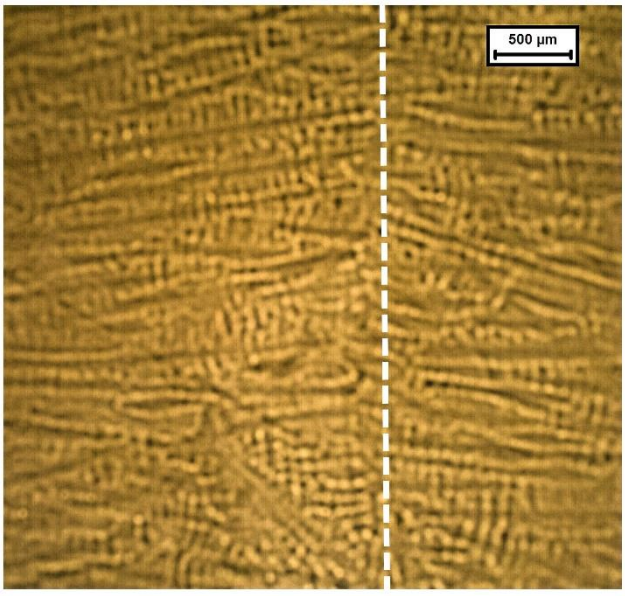

Figure 5.13: Dendritic solidification structure at the centre of step_3 for Fe-5.8 wt.% Mn alloy.

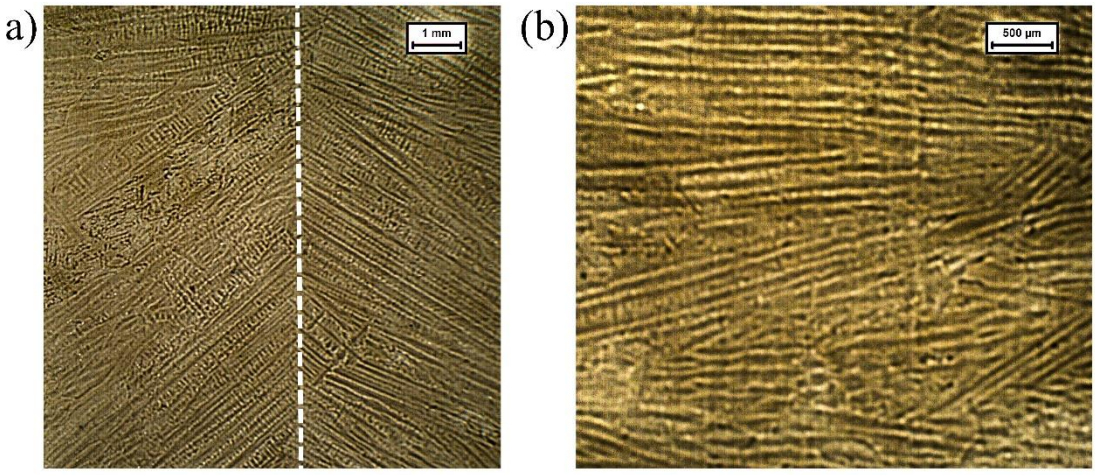

Figure 5.14: Dendritic solidification structure of step_4 for Fe-5.8 wt.% Mn alloy; (a) at the centre; (b) close to the surface.

Figure 5.14 shows the dendritic solidification structure of the step_4 for the same alloy. The marked centreline as shown in **Figure 5.14a** is much more prominent than that in **Figure 5.13**. The primary dendrite arms growing from opposite walls appear to meet along a straight line at the centreline. Fluid is not perfectly quiescent during ingot solidification. The inclined nature [157] of the primary dendrites is because of the presence of some degree of convection that is present during ingot solidification. This alters the concentration as well as thermal gradients which causes the dendrites to grow in upward inclined fashion. **Figure 5.14b** shows the solidification structure at a distance away from the surface. It can be seen that majority of the primary dendrite arms are observed to grow opposite to the primary heat extraction direction i.e. perpendicular to the mould wall. Similar fully columnar dendritic structure was observed for Fe-11 wt.% Mn alloy by Lu et al. [158]. **Figure 5.15** shows the solidification structure at the centre of step_5 of the ternary cast alloy with composition Fe-0.149 wt.% C-0.995 wt.% Mn. The secondary dendrite arms were coarser than that of Fe-5.8 wt.% Mn alloy.

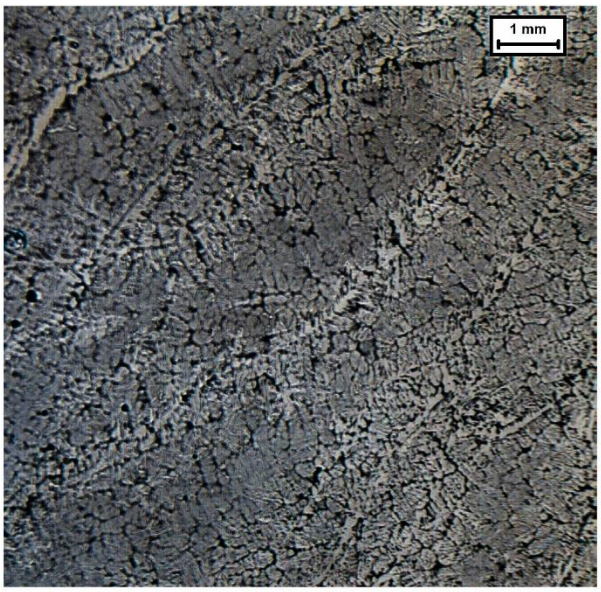

Figure 5.15: Solidification structure at the centre of step_5 of the ternary alloy Fe-0.149 wt.% C-0.995 wt.% Mn.

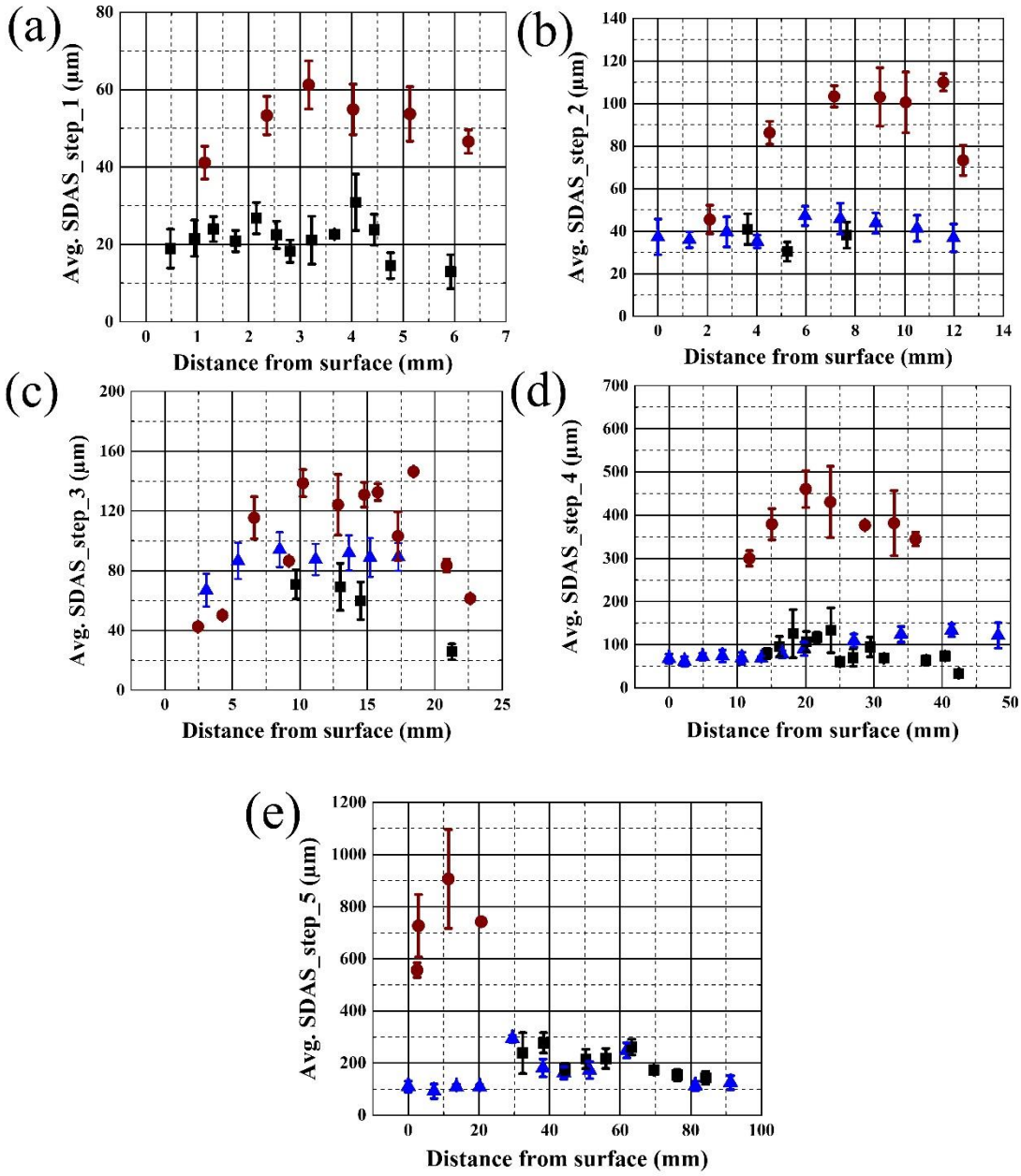

Figure 5.16: Variation in average (avg.) secondary dendrite arm spacing (SDAS) for the wedge mould cast alloys: Fe-5.8 wt.% Mn (▲), Fe-0.26 wt.% C (●) and Fe-0.149 wt.% C-0.995wt.% Mn (■)

The dendrite arm spacing measurements were performed from one surface towards the opposite end. Step_5 was the thickest section with a width of about 90 mm while step_1 was the thinnest section with a width of about 6 mm. **Figure 5.16** shows the variation in the secondary dendrite arm spacing for the analysed alloys. For each of the steps (i.e. from step_1 to step_5), the secondary dendrite arm spacing increased from surface towards the centre. This was because the cooling rate decreased from

surface towards the centre. The secondary dendrite arm spacing depends on the local solidification time [30] or the cooling rate. For the Fe-0.1 wt.% C alloy, the solidification model in the present work has shown (**Figure 5.12c**) that with increase in cooling rate the secondary dendrite arm spacing decreases. SDAS values for the 5th step of the Fe-5.8 wt.% Mn alloy were in the similar range to that obtained by Lu et al. [159] in directional solidification experiments for Fe-5 wt.% Mn alloy. **Figure 5.17** show the Fe-C and Fe-Mn equilibrium phase-diagrams as obtained from Thermo-Calc2019a software. From the Thermo-Calc2019a software [10], the difference between liquidus and solidus temperature (i.e. the equilibrium melting range) for the Fe-5.8 wt.% Mn alloy was found to be 9 K whereas for the Fe-0.26 wt.% C alloy it was 38.5 K. Thus the height of the two-phase (solid + liquid) region (i.e. the equilibrium melting range) from the equilibrium phase-diagram for Fe-0.26 wt.% C alloy is almost 4 times larger than that for the Fe-5.8 wt.% Mn alloy. That is why the solidification time interval for the Fe-0.26 wt.% C alloy would be much more than that for the Fe-5.8 wt.% Mn alloy. For the Fe-0.149 wt.% C-0.995 wt.% Mn ternary alloy, the difference between liquidus and solidus temperature was found to be 27.6 K. With decrease in the carbon content, the height of the two-phase region will decrease as can be seen from **Figure 5.17a**.

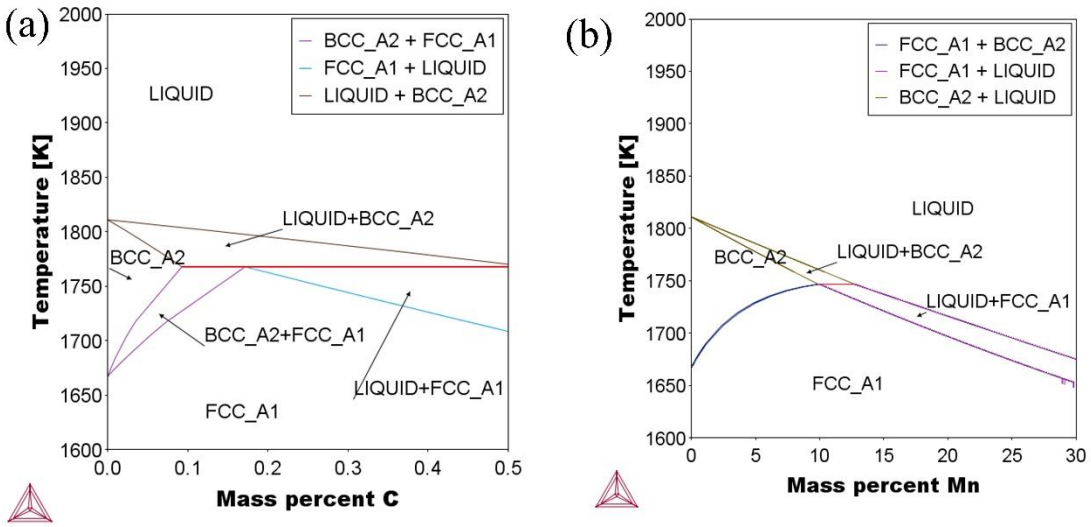

Figure 5.17: Binary alloy phase-diagram; (a) Fe-C phase diagram; (b) Fe-Mn phase diagram.

Since the height of the two-phase region for the Fe-0.26 wt.% C alloy is highest among the three alloys, it can be seen that for all the steps the SDAS values for Fe-0.26 wt.% C alloy is higher than the other two alloys. Also, the standard deviation of SDAS for the Fe-0.26 wt.% C alloy was higher than the other two alloys. Higher solidification time interval range means higher local solidification time and hence coarser will be the secondary dendrite arms. Secondary dendrite arm spacing also depends [80] on the casting process parameters like casting speed, melt superheat, alloy type etc. Higher casting speed will increase the heat extraction rate leading to finer dendrite arm spacing. On the other hand higher melt superheat will lead to higher heat input thereby delaying the heat extraction rate and hence leading to coarser dendrites. Not much difference in the secondary dendrite arm spacing could be observed between the Fe-5.8 wt.% Mn binary alloy and Fe-0.149 wt.% C-0.995 wt.% Mn ternary alloy. This may because of the fact that the Fe-5.8 wt.% Mn binary alloy was cast with 10°C higher superheat than that of the ternary alloy which would delay the heat extraction across the mould walls. Also, higher melt pouring time for the binary alloy would delay the heat extraction rate compared to the ternary alloy.

c) Segregation Ratio

Figure 5.18 shows the segregation ratio (C_{max}/C_{min}) of step_3 for the wedge mould cast binary alloys: Fe-5.8 wt.% Mn and Fe-0.26 wt.% C. The maximum and minimum concentrations were determined across zones of 1 mm each (say 0 – 1 mm, 1 – 2 mm and so on) from the line scanning raw data. It has already been shown that the solidification structure was fully columnar dendritic at the centre of step_3 of Fe-5.8 wt.% Mn alloy. In micro scale, the S/L interface advances perpendicular to the mould wall. In macro scale, this advancing micro-scale S/L interface can be viewed as the solidification front advancing perpendicular to the mould wall. As the front moves, it keeps on rejecting more solute with the progress of solidification. This rejected solute will get continuously pushed by the solidification front in the direction of the front movement towards the centre. For both the samples, the highest peak was observed close to the centre indicating centreline macrosegregation in **Figure 5.18**. Also, both the peaks were spread over a distance of 5 mm. The zones of positive segregation is due to the accumulation of inter-dendritic solute rich liquid [71]. All these high-intensity peaks were followed by zones of solute depleted liquid. The equilibrium

partitioning coefficient of Mn in δ-phase is about 0.724 [160] while in γ-phase it is 0.82. The equilibrium partitioning coefficient of carbon in δ-phase is about 0.18 [160] while in γ-phase it is 0.38. This shows the high segregating tendency of carbon compared to manganese.

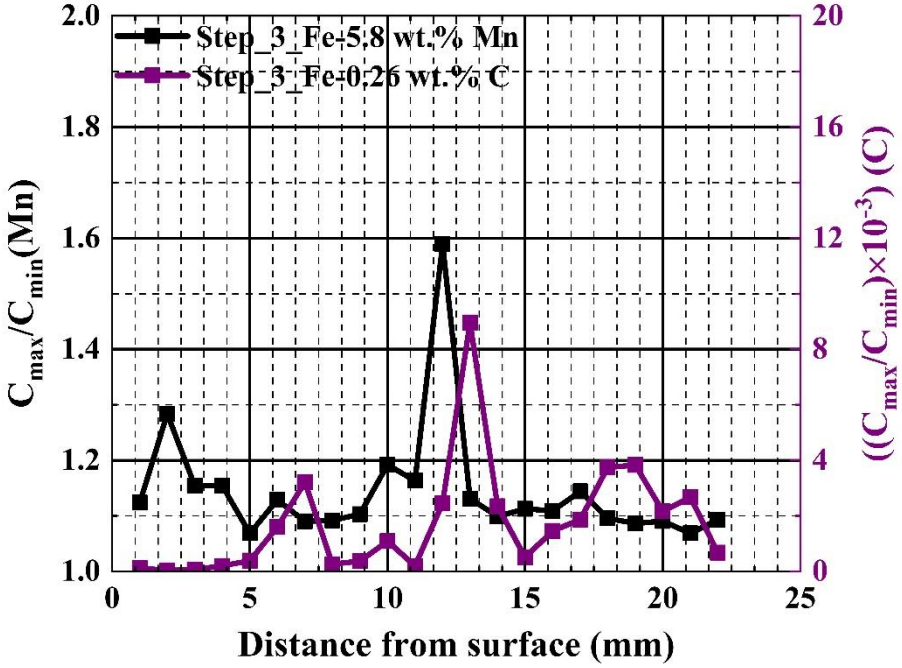

Figure 5.18: Segregation ratio (C_{max}/C_{min}) of step_3 for the wedge mould cast binary alloys: Fe-5.8 wt.% Mn and Fe-0.26 wt.% C (note that scales for manganese and carbon are different).

Figure 5.19 shows segregation ratio (C_{max}/C_{min}) of all the steps for the ternary wedge mould cast alloy Fe-0.149 wt.% C-0.995 wt.% Mn alloy. For all the steps, segregation ratio of manganese can be seen to increase from surface towards the centre. This shows the evidence of macrosegregation in the cast samples in the absence of fluid flow. Presence of bulk fluid flow will promote mixing due to convection and hence reduces macrosegregation. For the step_5 (**Figure 5.19e**), the composition variation extended over a distance of 90 mm while for step_4 it extended over a distance of 45 mm and so on for the rest of the samples. Step_3 of the ternary alloy showed evidence of macrosegregation while that for the Fe-5.8 wt.% Mn alloy showed only centreline macrosegregation. This may be because the equilibrium melting range for the Fe-Mn alloy was about 9 K while that for the ternary alloy was about 27.6 K. The diffusion

coefficients [160] of manganese in both δ-phase and γ-phase are almost similar which is 10,000 times slower than that in liquid phase. On the other hand, the diffusion coefficients of carbon in both δ-phase and γ-phase is only 10 times slower than that in liquid phase. Moreover, the diffusion coefficient of carbon in solid phase is almost 1000 times larger than that of manganese in solid phase. Hence the diffusion of manganese during solid-state transformation will be lesser compared to that in carbon. Thus it is expected that whatever segregation of manganese takes place during solidification is maintained till room temperature. Hence the macrosegregation pattern was better represented by the segregation plot for manganese than that of carbon. For the step_5, the increased segregation ratio of carbon close to the centre extended over a distance of 30 mm.

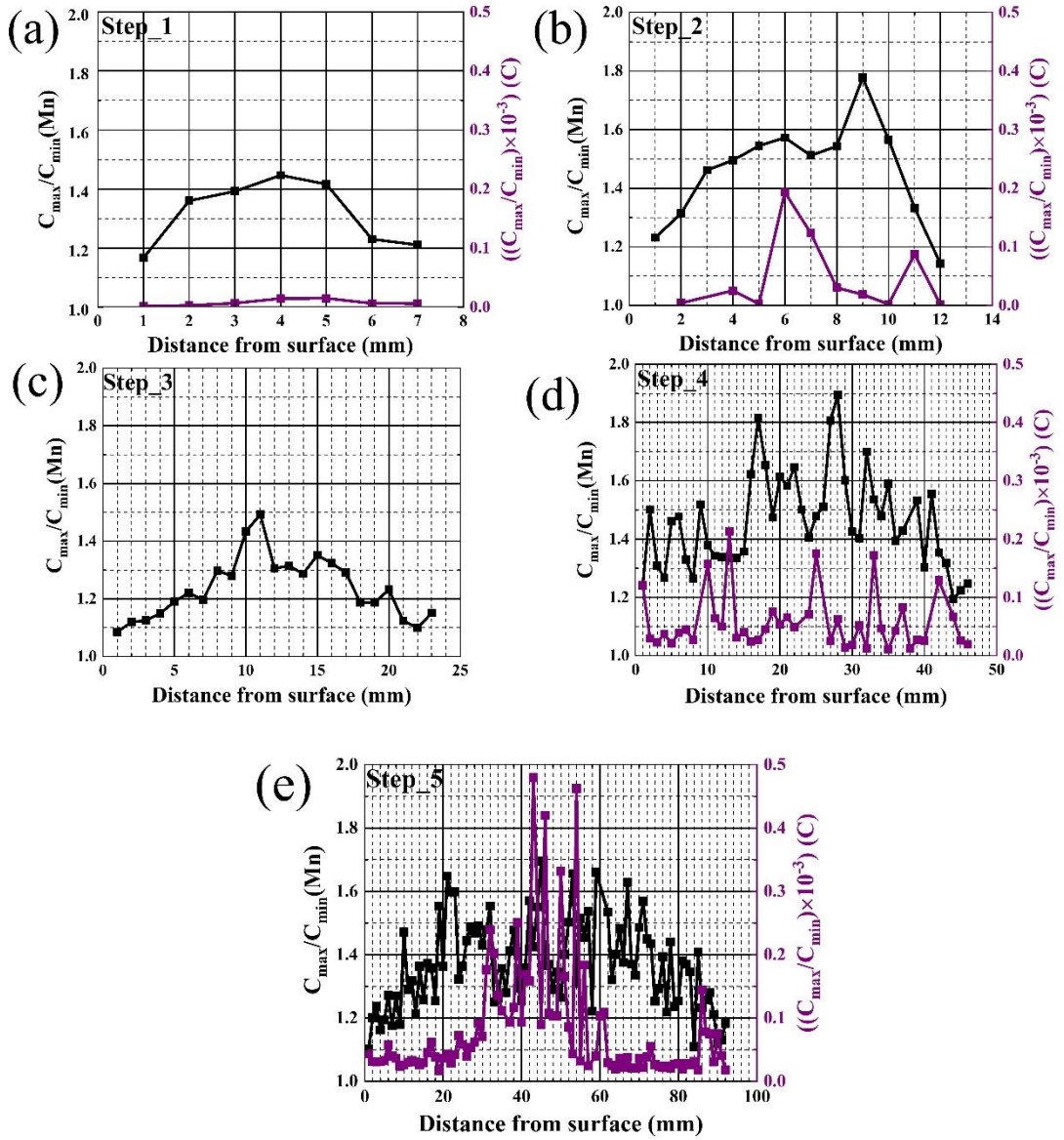

Figure 5.19: Segregation ratio (C_{max}/C_{min}) with increase in thickness of the solidified material for the ternary wedge mould cast alloy: Fe-0.149 wt.% C-0.995 wt.% Mn alloy; (a) step_1; (b) step_2; (c) step_3; (d) step_4; (e) step_5.

5.2. SOLIDIFICATION COUPLED with FLUID FLOW

In this section the numerical modelling results deal with how the binary alloy solidification model was coupled with fluid flow through step by step modifications. Then the results related to how the interface growth direction changes due to bulk flow are shown. At the end through fit function analysis, separate fit functions – one for the flow velocity dominated regime and other for the growth speed dominated regime, have been proposed and their significance to industrial casting conditions have also been discussed.

5.2.1 Fluid Flow Effect on Solidification of Two Component System (binary alloy)

Initially, the effect of fluid flow on isothermal solidification of Fe-0.108 wt.% C (Fe-0.5 mole% C) alloy at 1780 K was considered. **Figure 5.20** shows the fluid flow profile over the growing dendrite. The flow vectors enter the left wall of the domain. Then facing the growing solid obstacle in the shape of a dendrite, they rise up and after reaching the tip of the primary dendrite arm they follow the path towards the exit on the right wall. The magnitude of the flow vectors close to the tip of the primary arm reaches a maximum as the growing tip approaches the upper wall. It can be seen that there are no flow vectors inside the solid dendrite. The maximum fluid velocity close to the dendrite tip was found to be 0.67 m/s. The interface growth direction of the primary tip was found to be perpendicular to the bottom wall i.e. no change in growth direction was observed due to fluid flow compared to the case of pure solidification.

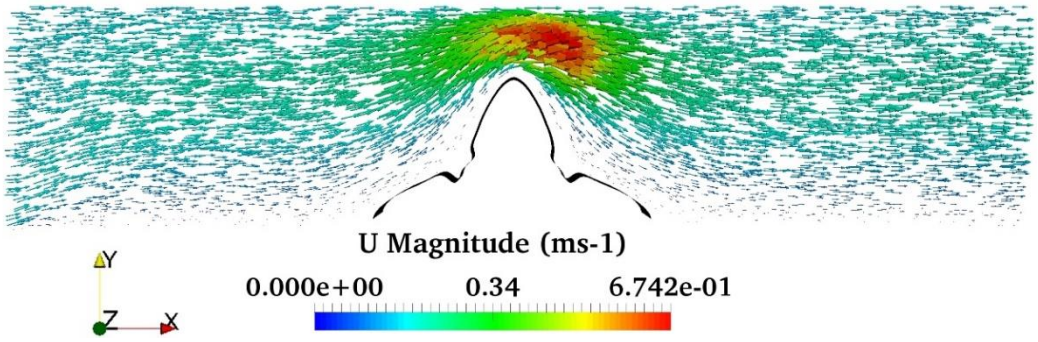

Figure 5.20: Fluid flow profile for isothermal solidification of Fe-0.108 wt.% C (Fe-0.5 mole% C) at 1780 K.

Figure 5.21 shows the effect of fluid flow on the growth of Fe-0.108 wt.% C (Fe-0.5 mole% C) dendrite under isothermal conditions at same time instants after a step modification. The firm black line in **Figure 5.21a** shows the growth direction of the main primary dendrite arm in absence of fluid flow. The firm yellow line in **Figure 5.21b** shows the growth direction of the main primary dendrite arm in presence of fluid flow. The left portion of the primary dendrite arm is the upstream direction whereas the right portion is the downstream direction. The other dendrite arms growing at the bottom wall and approaching the side walls are the upstream arm and the downstream arm respectively. It can be seen that due to fluid flow, the growth direction of the main primary dendrite arm got inclined towards the incoming fluid flow. Also, the distribution of the secondary dendrite arms on both sides of the main primary dendrite arm was symmetric in absence of fluid flow. Due to fluid flow, the growth of secondary dendrite arms on the upstream side was found to be higher than on the downstream side. These results qualitatively agree with literature [14,16,57]. But the growth rates of the upstream arm and the downstream arm were found to be similar both in the absence and presence of flow as can be seen from **Figure 5.21a** and **Figure 5.21b** respectively.

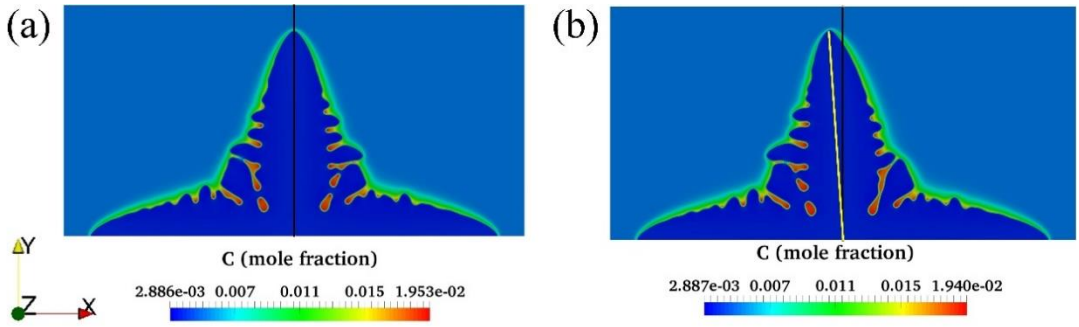

Figure 5.21: Effect of fluid flow on the growth of Fe-0.108 wt.% C (Fe-0.5 mole% C) dendrite under isothermal conditions at same time instants; (a) without flow; (b) with fluid flow.

Figure 5.22 shows the effect of fluid flow on the interface growth direction for an isothermal solidification of Fe–0.15 wt.% C binary alloy at an undercooling of 24.3 K. This particular alloy was taken so that the flow profile can be validated qualitatively with that obtained by Natsume et al. [57]. **Figure 5.22a** shows the growth of a solid in the form of dendrite in absence of fluid flow. The primary arm grows (shown by the black line) in the direction of maximum anisotropy i.e. perpendicular to the base of the domain. The image is symmetric with respect to the black line. **Figure 5.22d** shows the concentration profile along the white broken line with and without flow. The rejected solute build-up layer ahead of the moving interface is symmetric on both sides of the primary arm. The fluid flow profile (similar to that obtained by Natsume et al. [57]) at a time instant during the process of solidification is shown in **Figure 5.22c**.

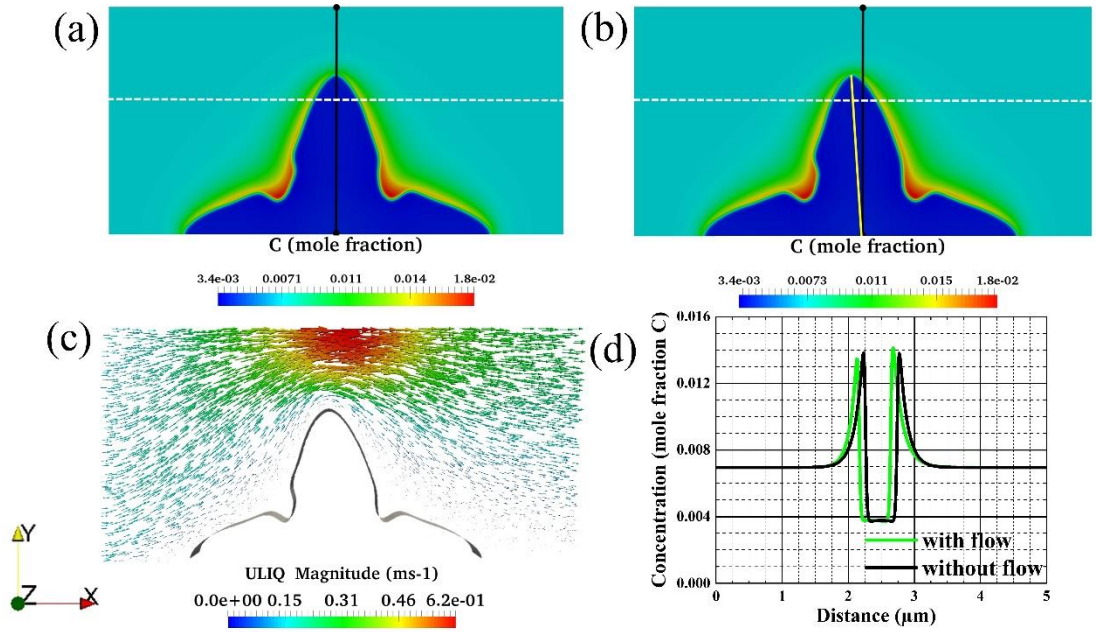

Figure 5.22: Effect of fluid flow on the interface growth direction for an isothermal solidification of Fe – 0.15 wt.% C binary alloy; (a) absence of fluid flow; (b) presence of fluid flow; (c) fluid flow profile; (d) concentration profile.

The flow vectors enter from the left wall of the domain. Then facing the growing solid obstacle, they rise up and after reaching the tip of the primary arm they follow the path towards the exit on the right wall. The magnitude of the flow vectors close to the tip of the primary arm reaches a maximum as the growing tip approaches the upper wall. **Figure 5.22b** represents the growth of the solid in presence of fluid flow. The growth direction of the primary arm is shown by the yellow line which is tilted with respect to the original growth direction in absence of fluid flow. Thus the growing solid bends towards the upstream direction of fluid flow. The angle between the original growth direction and deviated growth direction is the bending angle θ (as shown in the **equation 1.1**). This is because the incoming fluid on its way towards the exit takes away the rejected solute from the upstream side of the primary arm to the downstream side thereby creating a washing effect as pointed out by previous researchers [12,161]. This washing effect is responsible for asymmetrical solute build-up on either side of the primary dendrite as evident from **Figure 5.22d**. and thus defines the growth direction. The increased peak on the downstream side shows the enrichment of the solute, whereas there is depletion of solute on the upstream side. The higher the speed of the flow, the higher will be the asymmetry in the concentration profile and hence

the dendrite deflection angle. This reduces the undercooling on the downstream side and hence promotes growth of the solid phase on the upstream side. These results qualitatively agree with what observed in literature [14,16,57]. Since the growth of the solid phase was favoured in the upstream direction, the growth rate of the upstream arm was found to be higher than the downstream arm.

Also, the change in the growth direction being an instantaneous phenomenon, it is more relevant to speak of the flow velocity close to the tip rather than the incoming melt velocity. In case of multi-dendrite growth, even if the input melt flow speed is same, the flow velocity near the dendrite tips will depend on the growth pattern of the multiple dendrites and thus will contribute to the solute profile. During a stable continuous casting operation, the input liquid jet stream will have a stable velocity but the flow velocity in front of the moving solidification front at various depths from the meniscus will be different and thus will contribute differently to the solute profile at various stages of the casting operation. It is therefore imperative to study the influence of the flow velocity near the dendrite tip on the dendrite bending angle rather than the initial melt velocity at the entry point.

a) Transient effect of fluid flow on the dendrite growth

During solidification at a particular undercooling, it is known [16] that the growth speed of the dendrite tip initially remains high and then it gradually decreases with time due to decrease in thermodynamic driving force, thereby achieving almost a steady-state value. It is therefore quite important to study the time-dependent behaviour of dendrite growth direction in presence of fluid flow for a particular undercooling. For a constant inlet melt flow speed of 0.15 m/s, simulations were performed at five different levels of undercooling of 24.3 K, 19.3 K, 14.3 K, 9.3 K, and 6.3 K respectively. For each level of undercooling, the dendrite bending angle, the maximum flow velocity at the dendrite tip and the average growth speed of the tip of the primary arm were calculated at different time instants. **Figure 5.23** shows the 2D contour plot of the variation in dendrite bending angle with maximum fluid flow velocity at the tip and the growth speed as the axes for the whole set of simulation data points (shown as symbols). The bending angle is represented by the sine value of the angle (θ) instead of the value of the angle itself. This is because the sine value gives

the displacement between the tip and seed crystal position in the flow direction. Similar growth speeds at high undercooling have also been reported by Natsume et al. [57]. Two distinct features can be seen from **Figure 5.23** – one being the dependency on the maximum flow velocity and the other being the dependency on the growth speed. At a constant tip growth speed it can be seen that with increase in the maximum flow velocity at the tip, the bending angle increases. The initial steep increase in the bending angle decreases afterward and have a tendency to saturate towards the end. This situation may be correlated with the initial period of the continuous casting of steel when the liquid steel undercooling is relatively high. The liquid steel jet tends to wash away the rejected solute from the advancing solidification front as a result of which the bending angle may increase. Also reducing the casting speed i.e., inlet flow speed will reduce the bending angle.

At a constant maximum flow velocity, it can be seen that with decrease in the tip growth speed, the bending angle increases [57]. The increase in the bending angle is quite steep at lower growth velocities. This is because the fluid passing the dendrite tip has much more time to sweep away the rejected solute from the upstream side of the dendrite tip to the downstream side and thereby contributing to higher bending angle. However, in this growth speed dominant regime, the solute is not washed away to further distances and instead creates a trail of asymmetrical solute boundary layer. Thus this might be the point where diffusion tries to gain importance over bulk convection and may contribute to macrosegregation in the cast product. In the present work thus an attempt has been to separate out the two effects – flow velocity effect and growth speed effect on the bending angle. This information on bending angle might be useful for casting operators in finding out the linkage between the dendrite growth direction and the casting parameters at various stages of the casting and thereby take corrective action.

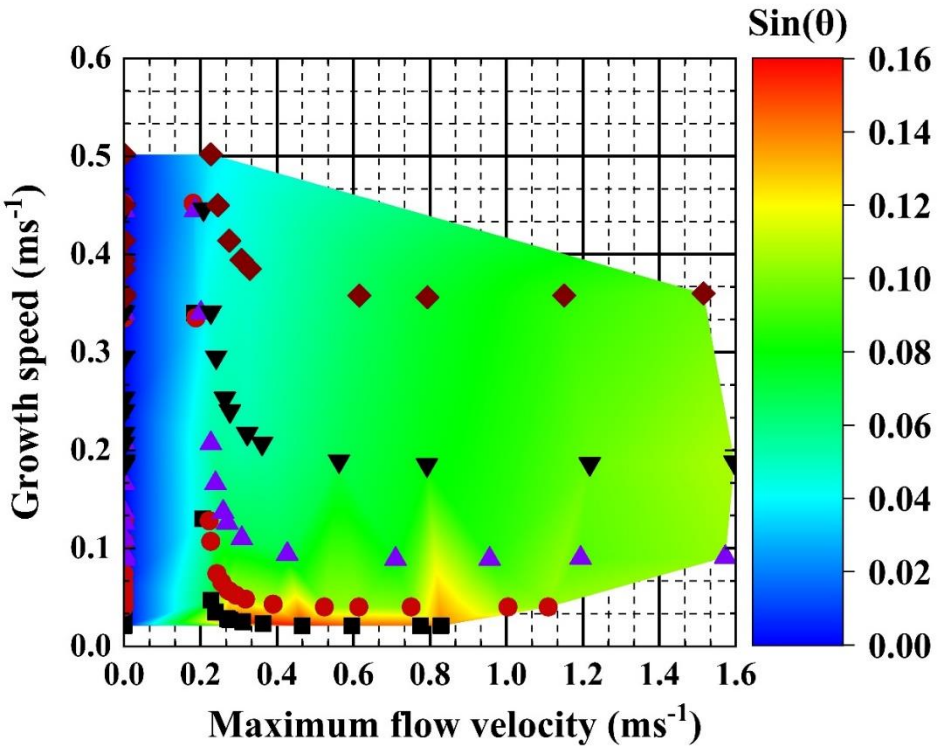

Figure 5.23: Variation of the bending angle in a Fe-0.15 wt.% C alloy as a function of maximum fluid velocity and dendrite growth speed. The symbols in the graph indicate different degrees of undercooling :(■) undercooling of 6.3 K, (●) undercooling of 9.3 K, (▲) undercooling of 14.3 K, (▼) undercooling of 19.3 K and (◆) undercooling of 24.3 K.

b) Fit Function Analysis

The objective here is to propose two independent correlations of predicting the dendrite bending angle – one based on the flow velocity and the other based on growth speed. The empirical dependence of deflection angle θ for steel ingots put forward by Takahashi et al. [9] is given as

$$\theta = 22.49\vec{V}^{-0.177} \log \frac{\left(0.00372 \times \vec{V}^{2.08}\right)}{v_{solidification}} \tag{5.1}$$

where θ is in degrees, $\vec{V}$ is the flow velocity of the bulk liquid in cm/s and $v_{solidification}$ is the solidification rate in cm/s. The flow velocity close to the moving front can be at times higher than the reported flow velocities of the incoming bulk fluid. The relation shows a logarithmic dependence on solidification rates and liquid flow velocity. The relation proposed by Okano et al. [8] has a resemblance with that of Takahashi. For both the relations, the dendrite bending angle is not mathematically defined at extremely low flow velocities and solidification rates because of the logarithmic dependence. Since the relations consider only the flow magnitudes, it is expected that the bending angle will always be positive. But in some cases, the predicted bending angle may turn out to be negative for the relations. Also, it is often challenging to carry out high-temperature experiments to measure the dendrite bending angle and relate to the industrial fluid flow conditions which involves cost and effort. Thus it can be quite useful to have simple bending angle relations with sound theoretical links that can be used to predict the bending angle from wide range of flow velocities and growth speeds. In future, these relations can also be fine-tuned based on industrial conditions. A theoretical relation developed for one particular alloy system can be extended to other systems - binary (e.g. Fe-Mn, Fe-Ni, Fe-Al, Al-Cu etc.) or even ternary systems (Fe-C-Mn, Fe-C-Al etc.). In this section, by revisiting these [8,9] bending angle formulae the authors have made an attempt to improve the mathematical basis with the obtained phase-field method based modelling results by incorporating the anisotropy in interface energy. **Figure 5.24** below shows the surface fitted (using MATLAB R2018a software) with the data points in the flow velocity dominated regime and the corresponding fit function (with 95% confidence limit) is given as

$$sin\theta = \left(1 - e^{-0.7551\vec{V}^{0.6}}\right)\left(e^{-1.851{v_{tip}}^{0.01}}\right) \tag{5.2}$$

where $\vec{V}$ is the maximum fluid velocity at the tip (m/s), v_{tip} is the tip growth speed (m/s). R^2 value for the relation was 0.99. The above relation (**equation 5.2**) is similar to that of Takahashi [9] relation (**equation 5.1**) in the sense that bending angle is directly proportional to the flow velocity but inversely proportional to growth speed of the front. Here it has been assumed that the growth speed of the solidification front in macro scale is synonymous to the tip growth speed in micro scale. The higher

exponent value of the flow velocity signifies the dominant effect of flow. The fitted surface shows that the bending angle increases with the flow velocity in an exponential manner and most of the data points lie close to the surface. The fitted surface moves towards a saturation level at very high flow velocities. The fitted equation shows that the bending angle is proportional to $\left(1 - e^{-0.7551\vec{V}^{0.6}}\right)$ which has a resemblance to that of Takahashi [9] where the bending angle is proportional to $log\vec{V}^{2.08}$. The exponent of the flow velocity may differ for different alloy systems.

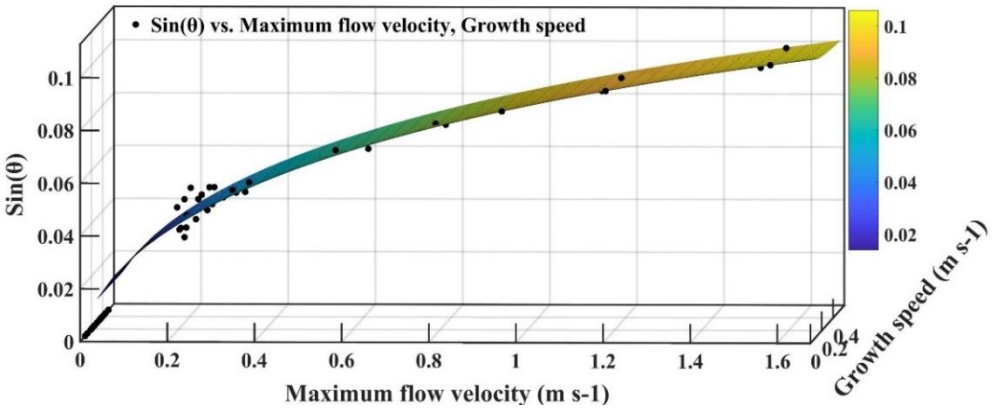

Figure 5.24: Simulated and fitted dendrite deflection angle in a Fe- 0.15wt.% C alloy in the fluid flow dominated regime. The black dots represent the simulated data points.

For the 2nd set of data points in the growth speed dominated regime, using the corresponding flow velocities and growth speeds, the bending angle values were first estimated from the previous fit function and then it was subtracted from the actual obtained bending angle values for those points. This was done to remove the base effect of the flow velocity on the bending angle for this set of data points so that the remaining effect would be the contribution from the growth speed. The corresponding fit function for the growth speed dominated regime after removing the effect of flow velocity (with 95% confidence limit) is given as

$$sin\theta = \left(1 - e^{-0.3505\vec{V}^{0.01}}\right)\left(e^{-8.753{v_{tip}}^{0.5}}\right) \tag{5.3}$$

where $\vec{V}$ is the maximum fluid velocity at the tip (m/s) and v_{tip} is the tip growth velocity (m/s). The R^2 value for the relation was 0.80. Higher exponent value of tip growth speed signifies the dominating effect of growth speed compared to flow velocity in this regime. The corresponding fitted surface shows the additional effect of growth speed on the bending angle on top of the fluid flow effect. Decrease in undercooling, decreases the thermodynamic driving force and hence decreases the growth speed of the interface. Since the growth speed decreases, the fluid flow will have more time to wash away the rejected solute and hence the bending angle will increase with decrease in undercooling. The second correlation (**equation 5.3**) gives solely the effect of growth speed on bending angle after removing the effect of flow velocity on bending angle. This particular fit function can be useful in predicting the bending angle in low growth speed regimes. In this case, also most of the data points were found to lie close to the surface. At very low growth speed, the bulk solute transport will be dominated by the diffusion which gives rise to high solute build-up ahead of the interface. Growth speed tending to very high values will give very low bending angle i.e., the interface will tend to grow as if it is a case of solidification without flow. Thus the combined fit function for the whole set of data points can be written as

$$sin\theta = \left(1 - e^{-0.7551\vec{V}^{0.6}}\right)\left(e^{-1.851{v_{tip}}^{0.01}}\right) + \left(1 - e^{-0.3505\vec{V}^{0.01}}\right)\left(e^{-8.753{v_{tip}}^{0.5}}\right) \quad (5.4)$$

Thus from the above equation, it can be seen that the total bending angle is the contribution from the flow velocity along with an additional contribution from growth speed. The above fit equation is mathematically defined for limiting cases i.e. cases of extremely high velocity or growth speed as well as extremely low velocity and growth speed. Obviously at zero velocity, the equation gives zero bending angle. **Figure 5.25** shows the fitted surface (fit function being **equation 5.4**) for the entire data set with a R^2 value of 0.95.

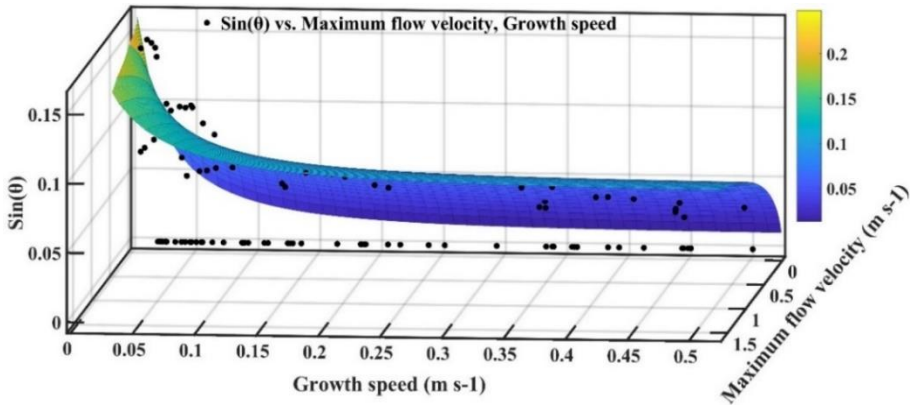

Figure 5.25: Dependency of bending angle during solidification of a Fe- 0.15 wt.% C alloy as a function of maximum flow velocity and growth speed. The black dots represent the simulated data points.

5.3 SUMMARY

In this chapter, the developed solidification models were validated separately for single component and two component systems with literature. Line scanning measurements showed that the segregation ratio in absence of bulk fluid flow increased from surface towards the centre for the ternary alloy. It was shown that due to fluid flow, the interface growth direction changed in a transient manner as a function of flow velocity and tip growth speed under different degrees of undercooling. At the end, separate fit functions relating bending angle to flow velocity and growth speed were proposed.

CHAPTER 6: APPROACH TO MICRO-MACRO COUPLING

In this chapter, the developed micro scale flow coupled model was coupled with the macro scale bulk flow profile of the continuous casting mould. Afterwards, the modelled bending angles were compared with that of the experimentally measured bending angles.

6.1 SOLIDIFICATION with FLUID FLOW

In the following sections, the chemical composition and casting process parameters of the collected slab samples have been mentioned. The section on the fluid flow profile gives an idea of the flow direction and magnitude of flow within the mould region. Thereafter an attempt has been made to correlate the experimentally measured dendrite deflection angles in the slab samples with that of the proposed micro scale fluid flow coupled solidification model taking input from the macro scale fluid flow profile and growth speed of the solidification front. Finally, a discussion on the effect of solute washing ahead of the moving front will be outlined, based on the analysis of chemical composition measurements in the slab samples.

6.1.1 Chemical Composition of Industrial Grades

Table 6.1 shows the chemical composition of the collected steel slab samples from the conventional slab caster. Samples A, B and D were low carbon grades whereas sample C was an ultra-low carbon grade. All the samples had similar manganese contents. The grades were selected to have minimal variation in the concentration of the elements other than carbon. **Figure 6.1** shows the relative position of the samples with respect to carbon content in the equilibrium phase diagram as determined by ThermoCalc software. All the samples will solidify in δ-ferrite mode. From sample C to A, B and then to sample D in the above diagram, it can be seen that the carbon

content increases. It is qualitatively expected that with increase in the solute carbon content the dendrite bending angle will increase [7].

Table 6.1: Chemical composition of the industrial slab samples used in this study.

Sample ID	Chemical Composition (wt.%)							
	C	Mn	P	S	Si	Nb	Mo	Ti
A	0.075	0.35	0.012	0.009	0.001	0.0	0.001	0.001
B	0.082	0.55	0.012	0.01	0.002	0.0	0.003	0.0
C	0.003	0.452	0.041	0.008	0.005	0.007	0.003	0.01
D	0.133	0.684	0.015	0.008	0.003	0.0	0.002	0.0

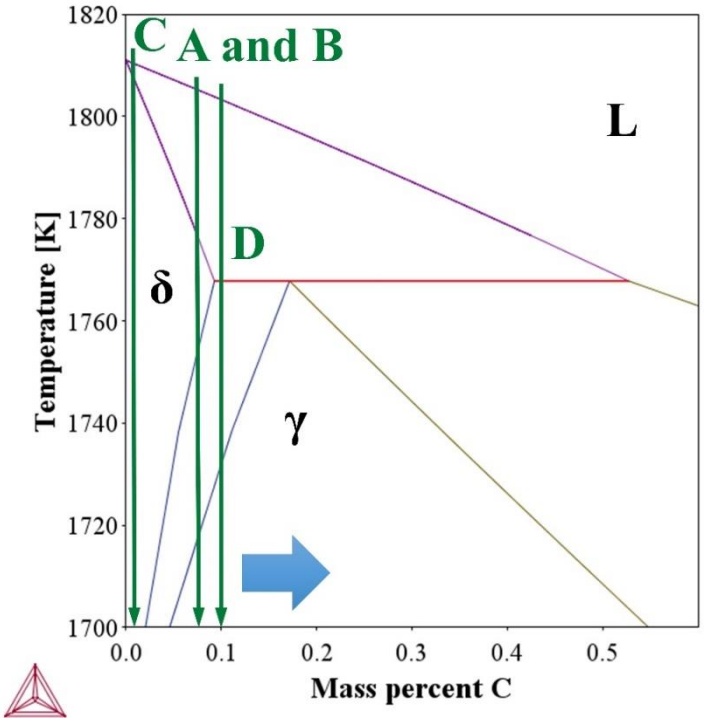

Figure 6.1: Carbon content of the collected steel slab samples in equilibrium phase diagram as determined by ThermoCalc.

6.1.2 Casting Process Parameters

Table 6.2 shows the casting process parameters of the collected slab samples. The total argon flow rates were similar for all the samples. All the samples had stable casting speed except sample D which had a wide variation in casting speed. This was due to the fact that sample D was collected during the ramp-up period, i.e. with continuous increase in casting speed. Sample A was taken from a slab having a casting speed of 1.7 m/min and width of 1300 mm. Sample B and C were taken from slabs having similar casting speeds but the sample B was from a slab having the highest width of 2100 mm. All the samples were cast under the influence of EMBR [54] and the thickness of all the slabs was 225 mm. The main objective of using EMBR nowadays in most of the industrial slab casters is to stabilize the turbulent flow within the mould region and reduce the meniscus fluctuations through the application of electromagnetic forces. Samples A, B and D were cast under the influence of single-ruler EMBR [54] which had a single layer of horizontal rectangular shaped magnetic field across the entire mould width. The sample C was cast under the influence of double-ruler EMBR [54] (also called FC-mould) which had two horizontal magnetic fields across the entire mould width – one above the SEN nozzle port and one below the SEN nozzle port. The author have not found enough literature where the dendrite bending angle in industrial steel slab samples under the influence of EMBR have been reported.

Table 6.2: Casting process parameters of the collected slab samples.

Sample ID	Caster	Casting Speed (m/min)	Superheat (°C)	Width (mm)	SEN depth (mm)	EMBR Current (A)
A	CC 1	1.7	23	1300	210	318.03
B	CC 1	1.25	21	2100	197	418
C	CC 2	1.19	42	1900	258	-500 (bottom) , 299 (top)
D	CC 1	0.76 – 1.55	16	1600		42.964 - 518

6.1.3 Dendrite Arm Spacing Measurements

The formulae [162,163] to calculate the solidified steel shell thickness growing over a mould wall in a conventional slab caster are given as

$$S = kt^{0.5} \tag{6.1}$$

$$t = z/v_c \tag{6.2}$$

where *S* is the solidified steel shell thickness in mm, *k* is the solidification coefficient in mm/min$^{0.5}$, *t* is the solidification time in min, *z* is the vertical distance from the meniscus along the casting direction in mm and v_c is the casting speed in m/min. *k* was determined from the examination of break out shells from the industrial caster. **Figure 6.2** below shows the schematic of solid steel shell growing on the mould wall during continuous casting process showing the meniscus and the casting direction. The higher the shell thickness, the higher is the vertical distance downwards from the meniscus. The approximate value of the constant *k* for both the conventional casters at Tata Steel in IJmuiden, The Netherlands was found to be *k* = 27. Though the cooling rates at the wide face walls and narrow face walls are adjusted accordingly to have uniform shell thickness on all the four walls, it has been reported [164] that the shell thickness on the wide face may be few mms more than that on the narrow face. This is because the two oppositely directed flows may impinge the shell along the narrow face wall and prevent the shell growth. From the above mentioned shell thickness formulae, the calculated values of the shell thickness for the samples A, B and C at the mould exit (taking mould length as 900 mm) was found to be about 20 – 25 mm [163,165]. Hence the dendrite arm spacing and the dendrite bending angle measurements for the slab samples were performed up to about 30 mm from the slab surface taking into account that the shell thickness on the wide face may be few mms higher.

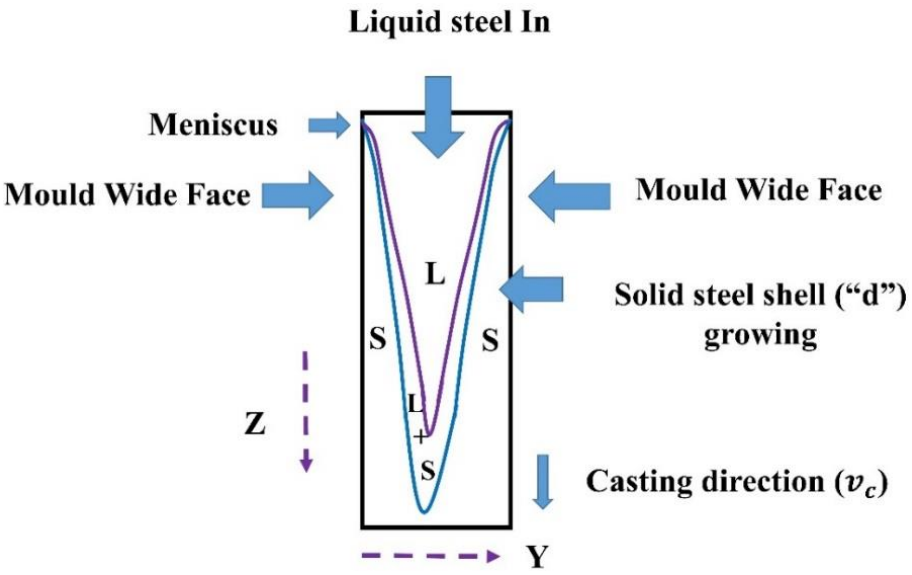

Figure 6.2: Schematic of solid steel shell growing on the mould wall during continuous casting process.

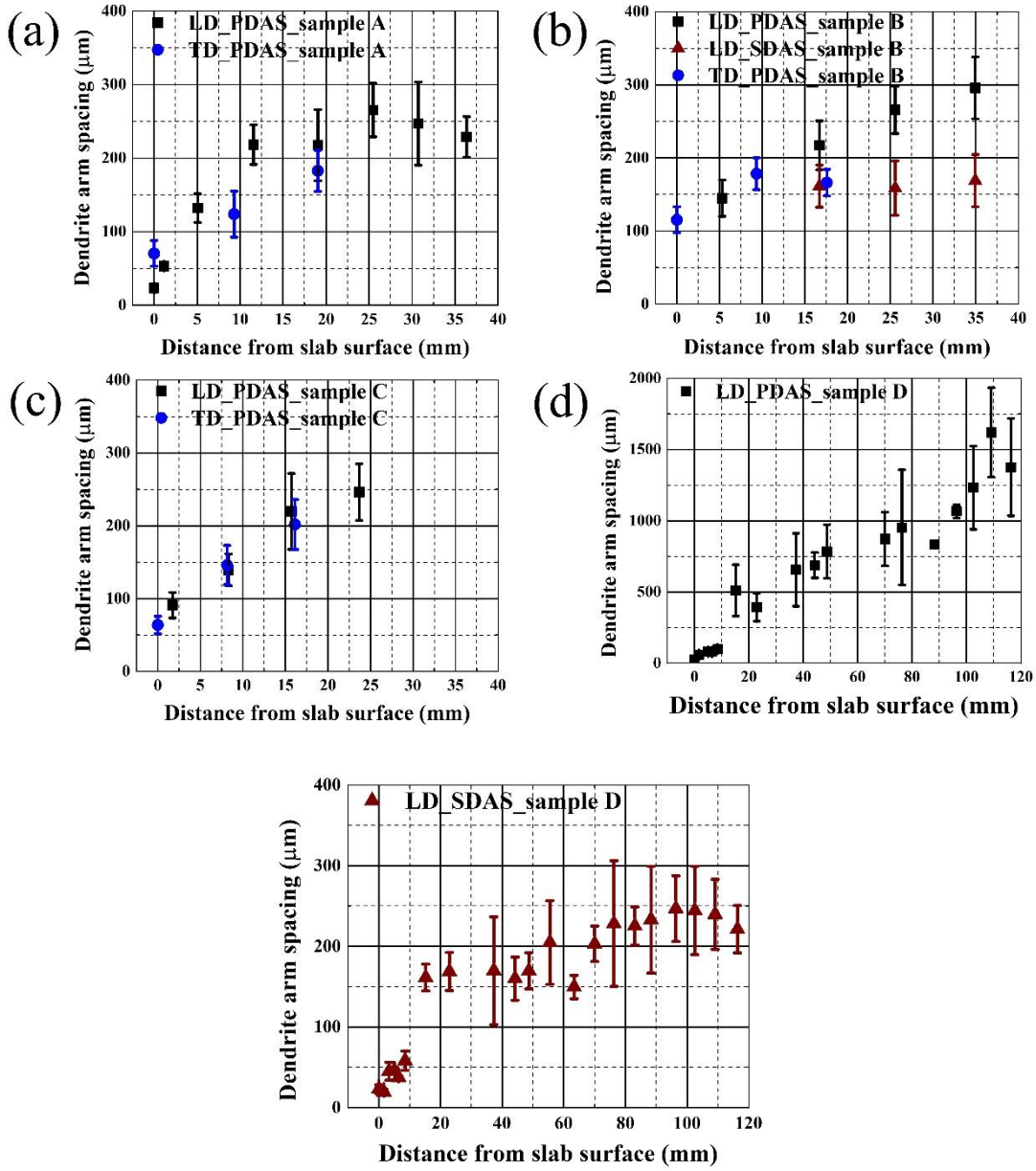

Figure 6.3: Variation in the dendrite arm spacing for the collected slab samples; (a) sample A; (b) sample B; (c) sample C; (d) primary dendrite arm spacing for sample D; (e) secondary dendrite arm spacing for sample D.

Figure 6.3 (a – e) shows the variation in dendrite arm spacing of the steel slab samples in longitudinal (LD) and transverse direction (TD) directions respectively. For the three samples (A, B and C) cast with stable casting speeds, the primary dendrite arm spacing along LD varied from 0 to 300 μm up to 35 mm inwards from the slab surface. Similar variation of PDAS in steel slab samples were also observed by others [74,166]. But the variation in the PDAS along LD was almost linear for samples B and C

respectively, while for sample A and D a change in the slope was observed at about 10 mm from the surface. For sample A, the initial variation in PDAS along LD was quite steep. For the sample D which was cast with a variable casting speed, the PDAS varied from 0 to 125 µm up to 10 mm from the surface along LD after which an abrupt increase in the PDAS to about 600 µm was observed at 20 mm. The PDAS varied from about 24 µm at the surface to as high as 1.8 mm at the slab centre for sample D. This much higher primary dendrite arm spacing at the centre may be due to higher equilibrium melting range of 30.1 K (for sample D) which would delay the solidification time. There may also be additional effect due to wide variation in casting speed. While calculating the equilibrium melting range, it was assumed that the slab samples were a ternary system i.e. Fe-C-Mn alloys. The SDAS in sample D along LD varied from about 23 µm at the surface to 300 µm at the slab centre. The change in slope for SDAS variation can also be seen for sample D along LD. It is worthwhile to mention that close to the slab centreline in sample D, the SDAS varied from 200 µm to 300 µm which was in the similar range to that observed at the centre of the step_5 of the ternary wedge mould cast alloy which had similar composition and similar equilibrium melting range of 27.6 K. Thus it can be said that both the slab centre of sample D and the centre of the step_5 of the ternary wedge mould alloy experienced similar cooling behaviour. Also, along TD the variation in PDAS for samples A, B and C were found to be in same range to that along LD indicating similar heat transfer behaviour.

6.1.4 Fluid Flow Profile

The fluid flow profiles of the industrial caster shown in this section were provided by Tata Steel in IJmuiden, The Netherlands. **Figure 6.4a** shows the average fluid flow profile (parallel to wide face i.e. along $z - x$ plane) within the mould region with single ruler EMBR for the CC1 caster as reported by Kholmatov [167]. The casting direction is along z axis while x axis represents the width direction. The casting speed was 1.7 m/min (similar to that of sample A in **table 6.2**) and the mould width was 1300 mm. The slab thickness was 225 mm and the EMBR current strength was 475 A. The SEN depth was 210 mm and superheat was 20°C. Flow vectors represent the fluid flow direction. The liquid steel exits the SEN port at high velocity which decreases towards the narrow face. One part of the flow after exiting the nozzle port is directed

downwards. It hits the narrow face wall and travels downwards. Some part of this flow after traversing downwards may change its direction and travel upwards towards SEN port bottom. The other part of the flow exiting the nozzle part after hitting the narrow face walls travels upwards towards the meniscus. Thus at one point, a transition in the flow direction [168] (from downward directed flow to upward meniscus directed flow) may take place as one goes downwards along the casting direction. Similar flow pattern in continuous casting mould has also been reported [169–172] with EMBR. It seems from **Figure 6.4b**, that at about 1/4th quarter distance (from the narrow face) the flow velocity increases from 0.06 m/s close to the surface to about 0.3 m/s in the zone of liquid steel jet. Further downwards, the velocity again decreases to about 0.1 m/s.

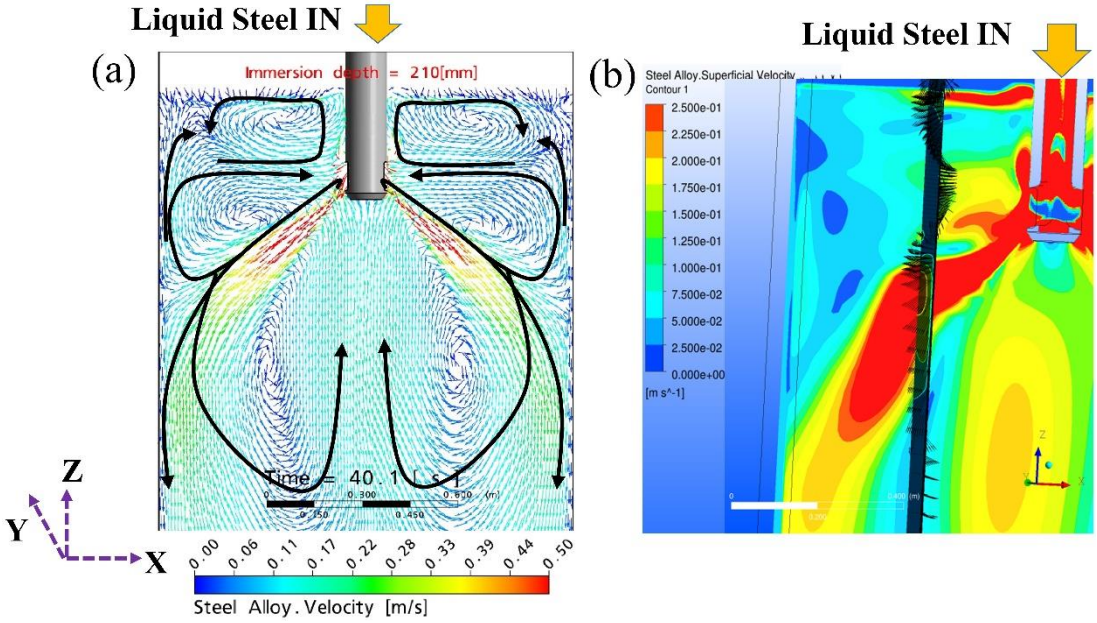

Figure 6.4: Fluid flow profiles as provided by Tata Steel in IJmuiden, The Netherlands; (a) Simulated fluid flow profile for CC1 caster at 1.7 m/min [167]; (b) velocity contours and flow vectors on a plane parallel to the narrow face for CC1 caster at 1.7 m/min [167].

Figure 6.4b shows the velocity contours and flow vectors on a plane (shown in black colour) parallel to narrow face. The position of the plane corresponds to the sample cutting position in the steel slab samples. Towards the meniscus, the flow is directed towards the narrow face while at a little lower position the flow is directed towards the SEN port. At a further lower position, the flow vectors can be seen to be moving

out of the plane and directed towards the narrow face while some vectors are seen to have a trend of upward-directed flow. Thus going downwards along the *z* direction parallel to the narrow face, it seems that at one point in the casting direction, there occurs a change in the flow direction. Having the fluid flow profile and growth speed of the front, one can translate it into the dendrite deflection angle which will give an idea of the solute washing effect across a section of a slab.

6.1.5 Dendrite Bending Angle Measurements

a) Measurement along LD i.e. *y* – *z* Plane

Figure 6.5 shows the variation of the dendrite growth direction from slab surface towards the slab center for sample A. Sample A had casting process parameters similar to the simulated fluid flow profile shown in **Figure 6.4**. Near the surface, all primary dendrites (shown as white broken lines) were found to be oriented in the same downward direction (assumed to be positive in the present work). At a little distance away from the slab surface, the primary dendrites undergo a change in growth direction from downwards to upwards. Some primary dendrites were seen to follow their original downward growth direction, while other dendrites were seen to have an upward growth direction. At a further distance away, all the primary dendrites were oriented in the upward direction, contrary to what was observed at the surface. Thus, it seemed that the observed change in the dendrite growth direction might be due to a change [168] in the fluid flow direction ahead of the moving front as shown in the **Figure 6.4**. The present experimental measurement validates the flow direction transition. Also, the magnitude of the dendrite bending angle along LD will give an estimate of the velocity component along the casting direction (i.e. along *z*).

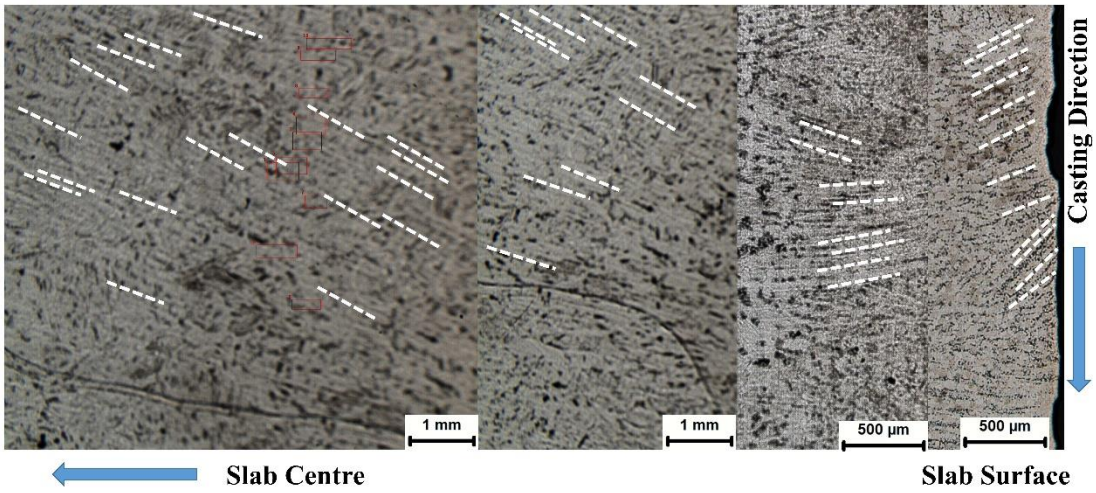

Figure 6.5: Variation in dendrite growth direction from the slab surface (right) towards the slab center (left) for sample A.

Figure 6.6a shows the dendrite growth direction for the sample C at a distance away from the surface and **Figure 6.6b** shows the dendrite growth direction close to the slab surface (casting direction downwards same as in **Figure 6.5)**. At the surface (**Figure 6.6b)**, some of the primary dendrites were inclined in the downward direction while the rest (marked as white / blue dashed lines) were inclined in the upward direction. Thus they show a tendency of transition in the growth direction from downwards to upwards. At a further distance away from the surface, most of the primary dendrites (marked as white dashed lines) were oriented upwards.

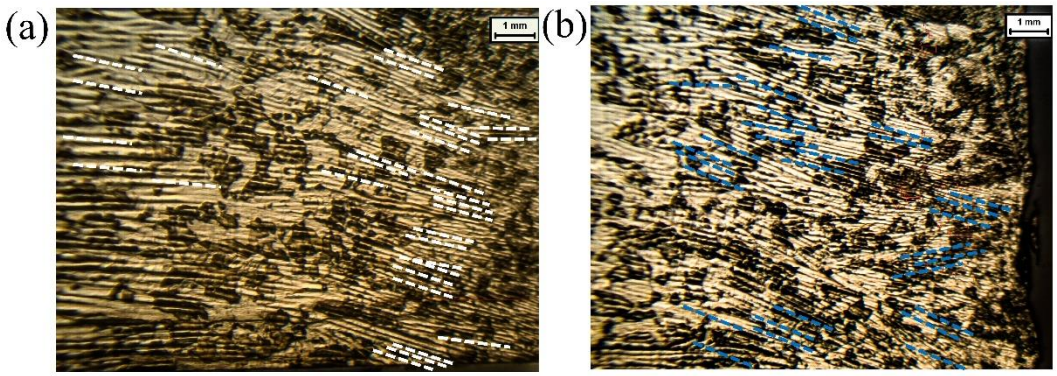

Figure 6.6: Dendrite growth direction for sample C; (a) away from the slab surface; (b) close to the slab surface.

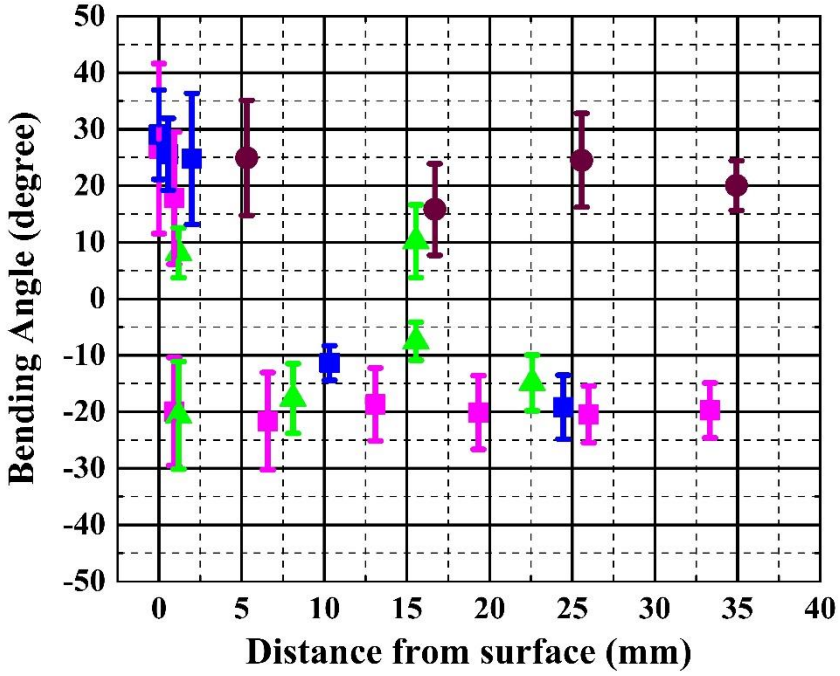

Figure 6.7: Variation in the dendrite bending angle for the slab samples along LD: Sample_A_1.7 m/min_1300 mm_LD (■), Sample_B_1.25 m/min_2100 mm_LD (●), Sample_C_1.19 m/min_1900 mm_LD (▲) and Sample_D_0.76 - 1.5 m/min_1600 mm_LD (■).

The contribution of the dendrite bending angle along LD will be dominantly from the *z* component of the velocity i.e. velocity component along the casting direction. **Figure 6.7** shows the variation in the dendrite bending angle for all the slab samples along LD up to a distance of about 30 mm. Okano et al. [8] obtained dendrite bending angles of similar magnitude close to the slab surface for steel slabs of 1890 mm wide, 260 mm thick and cast at 0.6 m/min but without EMBR. For sample A close to the surface, the dendrite bending angle was positive i.e. all the primary dendrites were oriented along the same direction (i.e. downward direction). Standard deviation of the bending angle was quite high at surface. This is may be because of the surface velocity fluctuations [173,174] of the liquid steel close to the meniscus. At a little distance away from the surface i.e. towards the centre, the bending angles were found to be both positive and negative indicating the transition phase of the flow direction. At a further distance away from the surface, the dendrite bending angle was negative indicating all the primary dendrites were oriented in a direction opposite to what they were at the slab surface. Thus the flow direction within the mould at this point was in

opposite direction to what was close to the meniscus. The mean value of the bending angle was almost constant after about 5 mm from the surface. Similar transition of the bending angle was observed for sample D as well which was cast under variable casting speed. The dendrite bending angle of sample B showed an interesting pattern. All the dendrite bending angles were found to be positive up to 35 mm from the surface i.e. no change in the growth direction was observed. It is to be noted that compared to sample A, the sample B was cast at a lower casting speed of 1.25 m/min and at a much higher mould width of 2100 mm. It is reported [175] that increase in mould width enables the liquid steel jet to hit the narrow face walls at lower positions. Though the sample B was cast at a lower casting speed than sample A, but much higher mould width for sample B provides relatively higher flow rate through the SEN nozzle as calculated from the formula mentioned by Thomas et al. [173]. Also, the EMBR current strength for sample B was 418A while that for the sample A was 318A. Higher EMBR current strength forces the liquid steel jet to bend downwards [176] and hit the narrow face walls at lower position. Thus one would expect the flow transition in sample B to happen at further distance away from the narrow face i.e. at higher value of shell thickness. The sample C was cast at a casting speed of 1.19 m/min. Also, sample C was an ultra-low carbon grade while the other samples had higher carbon content. It has been reported [7,13] that higher solute content causes more asymmetrical solute profile and higher deflection of the dendrites. Thus may be because of lower solute content, the mean values and the spread of the bending angle was found to be least for sample C among all the slab samples. In general, the spread of the dendrite bending angle across the mean value was found to be higher at the surface and decreased away from surface i.e. towards the centre. This may be because of the fact that the bulk fluid flow becomes more uniform and the velocity magnitude decreases in the casting direction towards the mould exit as shown in **Figure 6.4a**. The transition in the bending angle for sample A and D occurred at about 5 – 10 mm from the surface.

b) Measurement along TD i.e. *x* – *y* Plane

Figure 6.8a shows the dendrite growth direction for the sample B at a distance away from the surface and **Figure 6.8b** shows the dendrite growth direction close to the slab surface. At the surface, some of the primary dendrites (marked as white broken lines)

were inclined in the downward direction while the rest were inclined in the upward direction. Thus they show a tendency of transition in the growth direction from downwards to upwards. At a further distance away from the surface, most of the primary dendrites (marked as white broken lines) were oriented upwards.

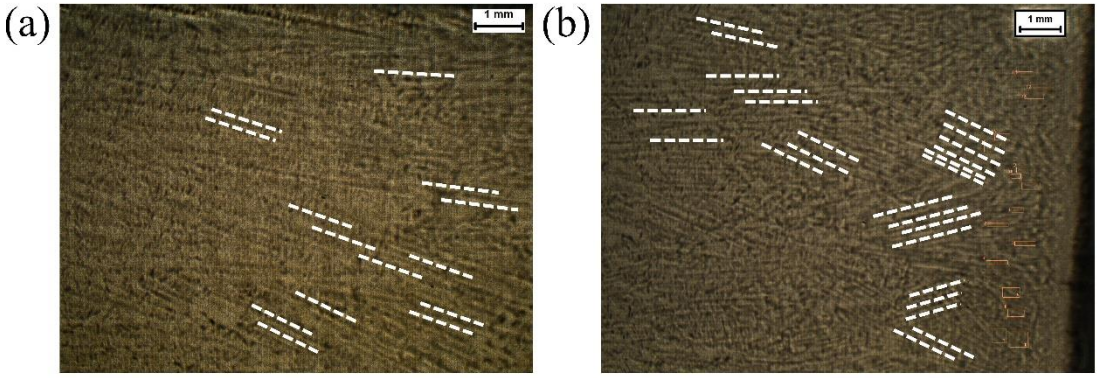

Figure 6.8: Dendrite growth direction for sample B; (a) away from the slab surface; (b) close to the slab surface.

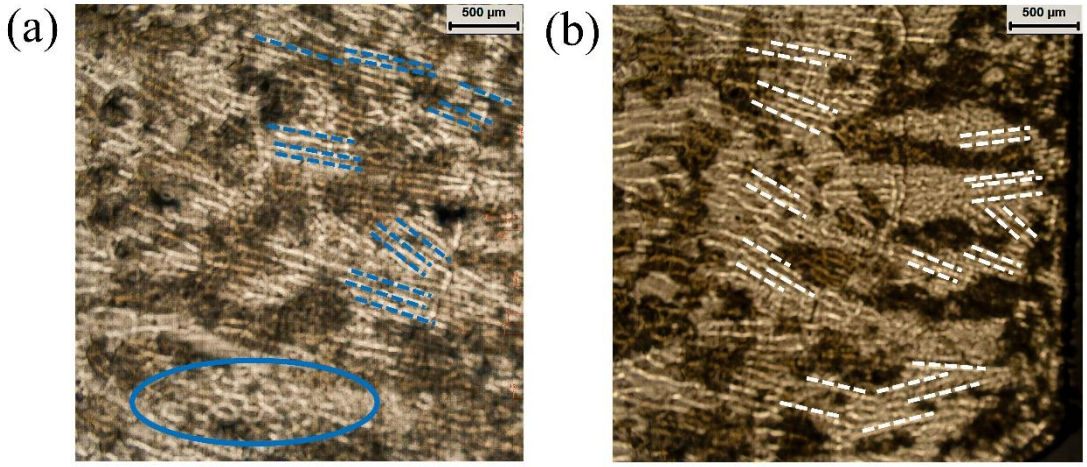

Figure 6.9: Dendrite growth direction for sample C; (a) away from the slab surface; (b) at the slab surface.

Similarly, **Figure 6.9a** shows the dendrite growth direction for the sample C at a distance away from the surface and **Figure 6.9b** shows the dendrite growth direction

close to the slab surface. The primary dendrites are marked as white / blue dashed lines. An interesting feature of this image is the presence of honeycomb-like structure as encircled in the **Figure 6.9a**. Since dendrites grow in 3D form on the wide face walls, analysing the sample along the *x* – *y* plane means some dendrites growing along the *z* (casting) direction will get cut through. Group of oval-shaped structures encircled in **Figure 6.9a** signifies group of dendrites growing along the casting direction being cut through.

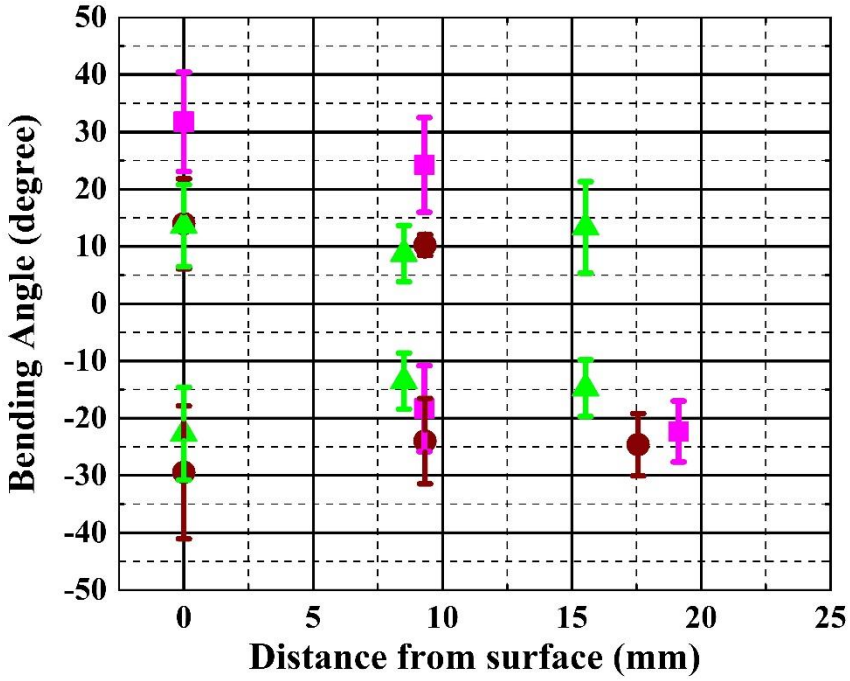

Figure 6.10: Variation in the dendrite bending angle for the slab samples along TD: Sample_A_1.7 m/min_1300 mm_TD (■), Sample_B_1.25 m/min_2100 mm_TD (●) and Sample_C_1.19 m/min_1900 mm_TD (▲).

The contribution of the dendrite bending angle along TD will be dominantly from the *x* component of the velocity i.e. velocity component along the mould width direction. Dendrite bending angle along TD was measured for samples A, B and C respectively. For sample A away from the surface, the dendrite bending angle changed sign from positive to negative indicating a possible transition in the flow direction similar to what was observed along LD. Though both sample B and C showed both positive and negative bending angle up to 15 mm from the surface, but the proportion of the positive angle decreased away from the surface indicating the possibility of flow

transition. Comparatively lower bending angle values of sample C to that of sample B may be due to lower content of sample C. In the **Figure 6.10** also, the spread and mean values of the dendrite bending angle were higher at the surface and decreased away from surface.

6.1.6 Micro-Macro Coupling

It is very challenging to simultaneously measure the fluid flow profile and flow magnitude as well as the growth speed of the solidification front within a continuous casting mould at liquid steel temperatures. Literature [173,174] is available for experimental measurements of surface velocity fluctuations in the mould. Till date, the researchers have relied upon qualitative fluid flow profile estimation through several numerical models [23,175,177]. A theoretical relation of the experimental dendrite bending angle with the simulated flow velocity and growth speed within the continuous casting mould would be of benefit to the casting technologist in controlling the casting process parameters. In this section, an attempt has been made in linking the proposed fit function of dendrite deflection angle with the simulated fluid velocity and growth speed through micro-macro coupling. The fit function derived in **equation 5.4** represents the dependency of the micro scale interface growth direction as a function of flow velocity and the tip (or interface) growth speed in micro scale. The macro scale fluid flow profile in a continuous casting mould at a typical casting speed has been shown in **Figure 6.4** which gives an idea of the magnitude of the flow velocity and flow direction at each point within the mould. **Figure 6.11** shows the schematic of two different (macro scale) shell thickness profiles (**S_1** at a casting speed v_{C1} and **S_2** at a casting speed v_{C2}, $v_{C2} > v_{C1}$) along the casting direction, growing over the mould wall with time. Going downwards along the casting direction, the shell thickness will increase according to **equation 6.1**. The higher the casting speed, the lower will be the shell thickness [98] at a particular point as can be inferred from **equation 6.1** and **equation 6.2** respectively. The flow vectors (shown in blue colour in **Figure 6.11**) can be seen to hit the growing shell (shown in purple colour) at different points. Thus the growing shell in macro scale can be viewed as the moving solidification front. By differentiating **equation 6.1**, the expression of the shell growth rate [178] as a function of casting speed and vertical distance from the meniscus (z) is given as

$$v_{shell} = \frac{dS}{dt} = \frac{k\sqrt{v_c}}{2\sqrt{z}} \tag{6.3}$$

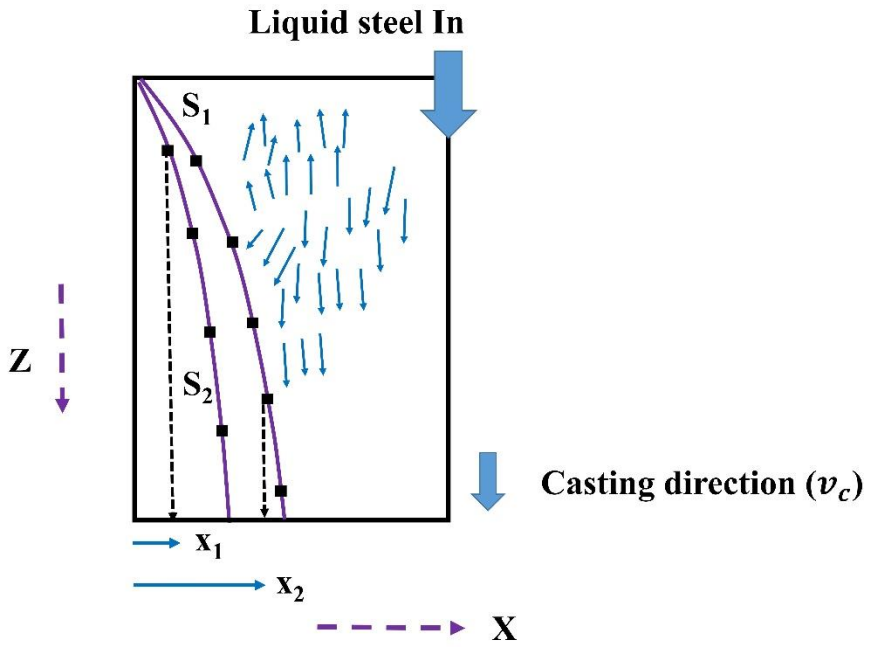

Figure 6.11: Macro scale shell thickness profiles (S_1 and S_2) growing over mould wall during continuous casting process.

The projection of various points (shown in black colour) on the growing shell thickness on *x* axis gives the value of shell thickness "S" from the slab surface. The projection (shown as black broken line) of two such points on the *x* axis gives the shell thickness values of x_1 and x_2 respectively. Thus each and every point on the growing shell for different casting speeds can be translated as distance from the slab surface towards the centre along the *x* axis. For each such point on the shell, the average macro growth speed of the moving front and the macro scale fluid flow profile can be derived from simulations. These macro scale values can be plugged into the proposed fit function (**equation 5.4**) to estimate the interface growth direction which will give an idea of the degree of solute washing. The higher the change in the interface growth (or bending angle), the higher will be the solute washing effect. These results can be then be validated with the composition profile measurements across slab surface thickness.

From the CFD flow profile as modelled by Kholmatov [167], flow velocity data for CC1 caster was retrieved for the following casting parameters - casting speed of 1.7

m/min, SEN depth 210 mm, EMBR current strength of 237 A and casting width of 1300 mm. These parameters were similar to that of sample A (**table 6.2**). A plane at 1/4th quarter distance from the narrow face wall was selected similar to that of the sample cutting position. **Figure 6.12** shows the $y - z$ plane parallel to narrow face. Solid steel shell is growing from both the wide face walls. Several vertical lines along the thickness direction (i.e. y direction) and specific distances from the slab surface were selected. In **Figure 6.12**, two vertical (black broken lines) were drawn at different distances from one of the mould wide face wall. The purple line indicates the liquidus line and the brown line indicates the solidus line. Going downwards along the black broken line (i.e. along the casting direction), the initial zone will be of 100% liquid. Below the liquidus line, the solid fraction will increase continuously and at the solidus line, the solid fraction will be 100%. At any vertical distance from the top, the distance of the solidus line from the mould wide face wall (along y direction) is the solid steel shell thickness. For example, the dendrite bending angle for sample A was measured at 6.5 mm from the surface. The corresponding vertical distance from the meniscus for a shell thickness of 6.5 mm was estimated from the CON1D model developed by B G Thomas et al. [121]. The CON1D model developed by B G Thomas et al. [121] gives the modelled shell thickness profile as a function of casting process parameters. The model is available with Tata Steel in IJmuiden, The Netherlands. Thus the vertical distance from the meniscus corresponding to shell thickness of 6.5 mm was estimated as 220 mm. It may be appropriate to say that the dendrites growing at 6.5 mm from the surface will get deflected due to the flow velocity in the two-phase region (S +L) region rather than the flow velocity in the fully liquid zone. For a quick calculation, in the present work the dendrite deflection was assumed to be a function of flow velocity in the fully liquid zone. The vertical line along the casting direction that showed 100% liquid at 220 mm from the meniscus was selected. Going downwards along that vertical line, at 220 mm from the meniscus the magnitude of the velocity components were found out from the available numerical model. The average solidification rate for the shell thickness of 6.5 mm was determined from the CON1D [121] model. For the present study, the macro scale solidification rate (or shell growth rate) at a particular distance from the CON1D model has been assumed to be same as the micro scale interface growth speed growing at the same distance. The corresponding growth rate and flow velocity were put into the proposed fit function (**equation 5.4**) as well as the relation proposed by Takahashi et al. [9] (**equation 5.1**). Then the deflection (or

bending) angles were estimated. These estimated deflection angles were then compared with the experimentally measured ones.

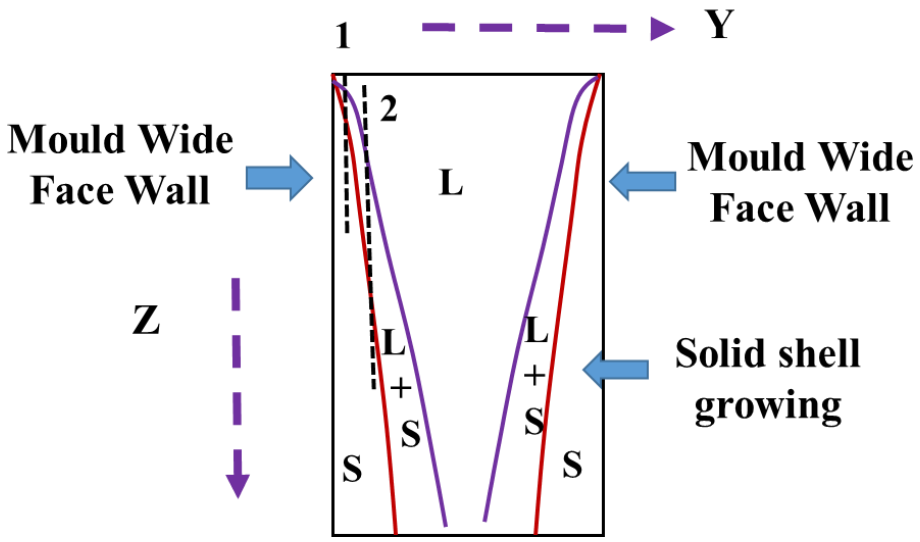

Figure 6.12: Schematic of solid shell growing over mould wall and estimation of flow velocity along vertical direction.

Figure 6.13a shows the variation of solidification rate (from CON1D) and velocity magnitude (from flow profile [167]) with distance from the meniscus for the casting process parameters corresponding to sample A. The solidification rate was highest close to the meniscus and steadily decreased with distance from the meniscus along the casting direction. The range of solidification rates in **Figure 6.13a** were similar to that of the reported [179] dendrite growth rates in the continuous casting process. The velocity magnitude close to the surface was low and then it increased up to a certain distance from the meniscus. The point where this increase in velocity occurs may be because it lies close to the liquid steel jet exiting the SEN port. Going further downwards the flow velocity was found to decrease. Xu et al. [171] simulated that at a depth of 35 mm from the meniscus the horizontal component of the velocity along the width direction varied from 0.17 to 0.07 m/s at about 1/4th quarter distance from the narrow face for a slab caster with casting parameters similar to sample A. The vertical component of the velocity along the casting direction at a distance away from the narrow face wall varied from 0.05 to 0.35 m/s.

From the CFD flow profile as modelled by Singh [180], flow velocity data for CC2 caster was retrieved for these casting parameters - casting speed of 1.2 m/min, double ruler EMBR current of -500 A / 300 A and casting width of 1700 mm. These parameters were similar to that of sample C (**table 6.2**) except the mould width which was 1900 mm for sample C as compared to 1700 mm mould width in the model [180]. **Figure 6.13b** shows the variation of solidification rate (from CON1D) and velocity magnitude (from flow profile [180]) with distance from the meniscus corresponding to sample C. The solidification rate decreased with distance from the meniscus along the casting direction. The fluid flow profile corresponding to the casting process parameters of sample B and D were not available with Tata Steel Research and Development in IJmuiden, The Netherlands. Hence the bending angles could not be modelled from the proposed fit function for those samples.

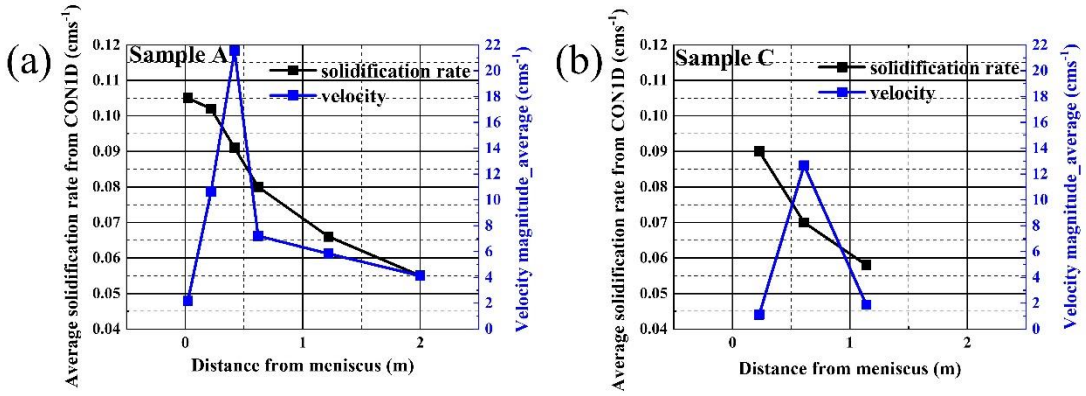

Figure 6.13: Variation of solidification rate and velocity magnitude with distance from meniscus; (a) sample A; (b) sample C.

Figure 6.14a shows the comparison of experimentally measured bending angles with that obtained from the Takahashi correlation and the proposed fit function for sample A and **Figure 6.14b** shows that of sample C respectively. At a specific distance from the meniscus, the modelled growth speed of the solidification front and the flow velocity ahead of the front were assumed to be constant. The modelled values were then put into the fit function to obtain the modelled bending angle. It can be seen that the estimated bending angles from the proposed (in the present work) correlation agrees well (within the experimental error) to experimental data while the data from Takahashi relation does not. At relatively low flow velocities, Takahashi relation

predicts low bending angles with values even close to zero and also negative in one of the case as shown in the figures. In this way, the experimentally measured dendrite growth direction can be useful in understanding the fluid flow direction existing within a continuous casting mould. Also, the variation in the magnitude of the measured dendrite bending angles will give an estimate of the flow magnitude within the mould. Hence an experimentally validated theoretical fit function can be useful to predict the fluid flow profile. The accuracy of the fit function depends on the governing equations used to model the flow profile and shell growth behaviour. It is to be noted that the fit function has been developed for a conventional slab caster but the same may not be applicable for a thin slab caster where the flow magnitude is relatively higher than conventional slab caster.

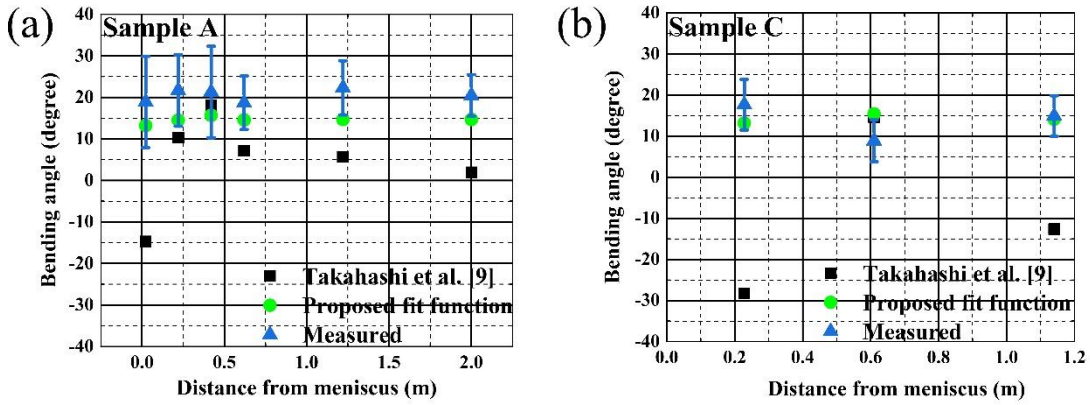

Figure 6.14: Comparison of experimentally measured bending angle with Takahashi [9] correlation and proposed fit function; (a) sample A; (b) sample C.

6.1.7 Segregation Ratio of Industrial Slab Samples

Okano et al. [8] reported the dendrite deflection in continuous cast steel samples but did not relate the deflection with the composition. **Figure 6.15** shows the segregation ratio plots of manganese and carbon with distance from the slab surface for the industrial slab samples listed in **table 6.1**. Samples A, B and C were cast under stable casting speed while sample D was cast under variable casting speed. Sample C being an ultra-low carbon grade, the carbon content was too low to detect in EPMA. Hence the plot contains only the segregation ratio of manganese. The corresponding

equilibrium melting ranges (from Thermo-Calc software) for samples A, B, C and D were found to be 29.4 K, 32.9 K, 1.8 K and 30.1 K respectively. The slab centre for all the samples was at 112.5 mm distance from the surface. Sample D was scanned up to the slab centre. Both sample B and sample C were scanned up to 60 mm from the surface while sample A was scanned up to 30 mm from the surface. It is to be noted that the segregation ratio scales shown in **Figure 6.15** are different to that shown for the wedge mould samples in **Figure 5.19**. Samples A, B and C showed no evidence of macrosegregation up to the distance as shown in **Figure 6.15** since the segregation ratio of both manganese and carbon remained almost constant. Segregation ratio plot for the step_5 of the ternary wedge mould cast alloy in **Figure 5.19** showed evidence of macrosegregation since it showed continuous increase of segregation ratio from surface towards the centre. The equilibrium melting range of the ternary wedge mould alloy (27.6 K) was similar to that of the slab samples A, B and D. In spite of the fact that the diffusion of carbon being much higher than that of manganese, both of carbon and manganese showed similar behaviour (i.e. no evidence of macrosegregation) in the slab samples. This indicates the effect of solute washing due to bulk fluid flow in the slab samples which will sweep away the rejected solute to further distance. This phenomenon was absent in the wedge mould casting where there was presence of only local flow. Due to this washing effect, dendrite deflection was observed in the slab samples. The observed peaks representing high segregation ratio in **Figure 6.15** correspond to zones of positive microsegregation. This may be because of the deformation induced flow[80] that takes place when the strand passes through the secondary cooling zone. The deforming action of the rolls on the solid shell causes squeezing action on the shell thereby affecting the dendrite movement leading to formation of zones of solute rich inter dendritic liquid [75]. The observed segregation ratio in the slab samples follows similar behaviour as obtained by El-Bealy [75]. Since in the present work segregation ratio was defined as the ratio of maximum to minimum concentration, the observed segregation ratio corresponding to the microsegregation peaks varied between 2 to 3.

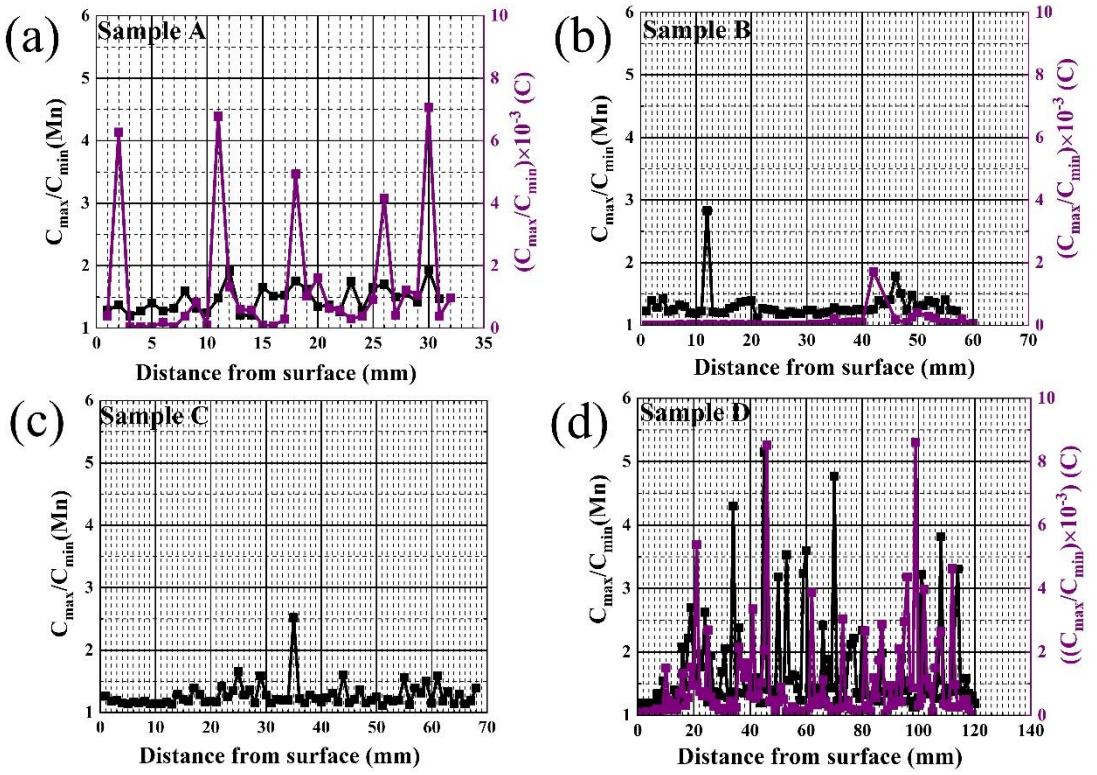

Figure 6.15: Segregation ratio (C_{max}/C_{min}) with distance from the slab surface for industrial slab samples; (a) sample A; (b) sample B; (c) sample C; (d) sample D. Note: the difference in *x*-axis lengths.

6.2 SUMMARY

Dendrite arm spacing measurements in the industrial slab samples showed that both the primary and secondary dendrite arm spacing increased away from the slab surface. The primary dendrites growing at the slab surface showed a change in the growth direction at a certain distance away from the surface indicating the change in flow direction. This change in the growth direction was a validation of the change in flow profile observed in the modelled macro scale bulk flow profile. The investigated slab samples were cast under the influence of EMBR. The standard deviation of the mean bending angles decreased away from surface. The modelled bending angles were found to tally well with that of the experimentally measured ones.

CHAPTER 7: CONCLUSIONS and SUGGESTIONS for FURTHER WORK

7.1 CONCLUSIONS

Due to increased demand of advanced high strength steel grades, steelmakers are facing stiff market competition in order to keep up pace with production volume along with product quality. Increased proportion of different alloying elements giving versatile mechanical properties of the finished product is prompting the material science community to look into the intricate relationship of the phenomenon of macrosegregation with the process parameters during a continuous casting process. Only a few available literature resources report that the bulk fluid flow has a washing effect in front of the advancing interface during solidification. But the focus on macrosegregation in steels has been mainly related to the internal flows due to shrinkage and deformation. However, the link between the dendrite evolution phenomenon happening at the micro scale and its effect on the macro scale is not understood completely.

In the present research, an attempt was made to both computationally and experimentally understand the effect of bulk fluid flow on the evolving solute profile build up ahead of the micro scale S/L interface. Afterwards the phenomenon happening at the micro scale was linked to macro scale composition profile in larger sections of the solidified sample through micro-macro coupling approach. A theoretical improved relationship between the preferred interface growth direction and the flow parameters has been proposed with the help of a fluid flow coupled and phase-field method based solidification model for a Fe-C alloy. Lastly, comparison on the effect of fluid flow on macrosegregation in the solidified sample was made through composition profile analysis of the wedge mould ingot cast samples and the industrial samples via continuous casting route.

- An open source fluid flow coupled and phase-field method based model has been developed for binary alloy solidification under isothermal condition to

understand the behaviour of dendrite growth direction due to fluid flow. The model can be extended to other binary or ternary alloys.

- At a particular level on undercooling, the tip growth speed and the flow velocity at the dendrite tip changed with time and hence the bending angle. In this way, an array of deflection angle data along with flow velocity at the tip and tip growth speed were obtained for different levels of undercooling.
- An attempt to separate the effects of flow velocity and growth speed on the bending angle have been made. This can be useful in predicting the preferred interface growth direction under industrial casting conditions by studying at what point of casting and up to what extent both the diffusion and bulk fluid flow interacts with solute layer ahead of the solidification interface.
- Anisotropy in interface energy based separate fit functions dependent on flow velocity at the tip and growth speed have been postulated which are an extension of the empirical correlations proposed by Takahashi et al. [9].
- Through the approach of micro-macro coupling, an attempt was made to correlate the micro scale proposed fit function with that of the macro scale bulk flow profile. The proposed fit function was found to fit better with the experimental deflection angles, compared to the standard empirical Takahashi correlation.
- Among the three wedge mould cast ingots (where there was absence of bulk fluid flow), the secondary dendrite arm spacing of the Fe-C alloy was found to be highest due to greater width of the two phase (solid and liquid) region. With increase in the thickness of the solidified portion, the secondary dendrite arm spacing of ternary wedge mould cast alloy increased.
- The secondary dendrite arm spacing at the centre of the slab sample with highest carbon content was found to be in the similar range to that observed at the centre of step with highest thickness of the ternary wedge mould cast ingot which had similar composition. Thus the idea of replicating solidification structure in industrial samples was conceived through laboratory scale wedge mould casting which could help in development of advanced steel grades in future.
- Good agreement of fluid flow transition between the fluid flow simulations and the experimental measurement of dendrite deflection angles were obtained

for the industrial slab samples from conventional caster. The measured dendrite bending angles showed a transition in the growth direction with distance from the slab surface.

- Line scanning composition measurements of the wedge mould cast ternary alloy showed that the segregation ratio of manganese continuously increased from surface towards the centre. Due to absence of bulk fluid flow, the rejected solute ahead of the interface was not washed away thereby leading to its continuous accumulation ahead of the moving interface. For the slab samples, the segregation ratio of manganese remained almost constant up to several mms of the analysed portion indicating the effect of bulk fluid flow.

7.2 SUGGESTIONS for FUTURE WORK

Investigations on the following topics can be sought as an extension of the present research which will benefit the scientific community further.

- Extending the developed flow coupled micro scale model to ternary system [142] will be more useful for casting technology since most of present advanced high strength steel grades are either ternary or even quaternary systems. This will help in understanding the interface growth direction in presence of more than one solute element. Further to that, one can also study how fluid flow effects the interaction between different solute elements. By studying the varied solute contents, one can gradually incorporate additional solute dependency factors in the proposed fit function.
- Extending the model to ternary or quaternary systems [181] involve additional governing equations for phase-field and solute diffusion which will make the model computationally intensive. Till date, it has been found that not much focus has been given on the improving the computational efficiency of the phase-field method based numerical codes. In reality, the dendrite growth occurs in 3D fashion. Also, it is said that the transport behaviour due to 3D effect [182,183] of fluid flow on the dendrite growth pattern is more compared to the 2D effect because of additional flow around the dendrite. Thus studying

the fluid flow effect in 3D will give a more realistic picture of the interface growth behaviour.

- Analysing slab samples of different casting parameters will give better in-depth understanding of fluid flow behaviour to the casting technologist. Also, the effect of electromagnetic brake can be studied. It will be interesting to see the effect of fluid flow on dendrite deflection of the slab samples along the width direction since the fluid traverses much larger distance along the width direction than along the thickness direction.

REFERENCES

[1] B.G. Thomas, Continuous Casting of Steel, in: Model. Cast. Solidif. Process., New York, 2001: pp. 499–540.

[2] W.S. Association, FACT SHEET Advanced steel applications, 2018.

[3] D. Senk, B. Engl, O. Siemon, G. Stebner, Investigation of solidification and microsegregation of near-net-shape cast carbon steel, Steel Res. 70 (1999) 368–372.

[4] B. Böttger, M. Apel, B. Santillana, D.G. Eskin, Relationship between solidification microstructure and hot cracking susceptibility for continuous casting of low-carbon and high-strength low-alloyed steels: A phase-field study, Metall. Mater. Trans. A Phys. Metall. Mater. Sci. 44 (2013) 3765–3777.

[5] M. Nakagawa, Y. Natsume, K. Ohsasa, Dendrite growth model using front tracking technique with New growth algorithm, ISIJ Int. 46 (2006) 909–913.

[6] L. Arnberg, R.H. Mathiesen, The real-time, high-resolution X-ray video microscopy of solidification in aluminum alloys, JOM. 59 (2007) 20–26.

[7] H. Esaka, F. Suter, S. Ogibayashi, Influence of Carbon Content on the Growth Angle of Steel Dendrites in a Flowing Melt, ISIJ Int. 36 (1996) 1264–1272.

[8] S. Okano, T. Nishimura, H. Ooi, T. Chino, Relation between Large Inclusions and Growth Cast Directions of Columnar Dendrites in Continuously Slabs, Tetsu-to-Hagané. 61 (1975) 2982–2990.

[9] T. Takahashi, K. Ichikawa, M. Kudou, K. Shimahara, The Effect of Fluid Flow on the Macrosegregation in Steel Ingot, Tetsu-to-Hagane. 61 (1975) 2198–2213.

[10] P. Gustafson, A thermodynamic evaluation of the Fe-C system, Scand. J. Metall. 14 (1985) 259–267.

[11] W.J. Boettinger, J.A. Warren, C. Beckermann, A. Karma, Phase-Field Simulation of Solidification, Annu. Rev. Mater. Res. 32 (2002) 163–194.

[12] M.F. Zhu, T. Dai, S.Y. Lee, C.P. Hong, Modeling of solutal dendritic growth with melt convection, Comput. Math. with Appl. 55 (2008) 1620–1628.

[13] S.Y. Lee, S.M. Lee, C.P. Hong, Numerical modeling of deflected columnar dendritic grains solidified in a flowing melt and its experimental verification, ISIJ Int. 40 (2000) 48–57.

[14] M.X. Liu, K. Wang, D. Xia, T. Jiang, Phase field simulation of Al-Si binary dendritic growth and micro-segregation patterns under convection, J. Alloys Compd. 589 (2014) 431–435.

[15] H. Barati, M.R. Aboutalebi, S.G. Shabestari, S.H. Seyedein, Investigation on dendritic solidification and microsegregation in presence of melt convection using phase field simulation, Can. Metall. Q. 50 (2011) 408–415.

[16] L. Du, R. Zhang, Phase-Field Simulation of Concentration and Temperature Distribution During Dendritic Growth in a Forced Liquid Metal Flow, Metall. Mater. Trans. B. 45B (2014) 2504–2515.

[17] L. Qiang, Y. Xiang-Jie, L. Zhi-Ling, Influence of the Melt Flow rate on Dendrite Micro Segregation During Alloy Solidification Simulated by Phase Field Method, J. Appl. Sci. 13 (2013) 2700–2704.

[18] H. Esaka, T. Taenaka, H. Ohishi, S. Mizoguchi, H. Kajioka, Deflection Mechanism of Columnar Dendrite Due to Fluid Flow, J. Jpn. Soc. Microgravity Appl. 6 (1989) 20–25.

[19] K. Murakami, T. Fujiyama, A. Koike, T. Okamoto, Influence Of Melt Flow On The Growth Directions Of Columnar Grains And Columnar Dendrites, Acta Metall. 31 (1983) 1425–1432.

[20] C.J. Greenshields, OpenFOAM, version4.0, OpenFOAM Foundation Ltd., 2016.

[21] B.G. Thomas, Continuous Casting, Encycl. Mater. Sci. Technol. 2nd Ed. (2001) 1595–1598.

[22] S. Louhenkilpi, Continuous Casting of Steel, in: Treatise Process Metall., Elsevier Ltd., 2014: pp. 373–434.

[23] B.G. Thomas, L. Zhang, Mathematical Modeling of Fluid Flow in Continuous Casting, ISIJ. 41 (2001) 1181–1193.

[24] M.M. Wolf, Historical Aspects and Key Technologies, in: Making, Shaping, Treat. Steel, The AISE Steel Foundation, Pittsburgh, 2003: pp. 1–38.

[25] K.C. Mills, A.B. Fox, Z. Li, R.P. Thackray, Performance and properties of

mould fluxes, Ironmak. Steelmak. 32 (2005) 26–34.

[26] R. Singh, B.G. Thomas, S.P. Vanka, Large Eddy Simulations of Double-Ruler Electromagnetic Field Effect on Transient Flow During Continuous Casting, Metall. Mater. Trans. B. 45 (2014) 1098–1115.

[27] D.J. Sosinsky, P. Campbell, R. Mahapatra, W. Blejde, F. Fisher, THE Castrip ® Process – Recent Developments At NUCOR STEEL'S Commercial Strip Casting Plant, Metallurgist. 52 (2008) 691–699.

[28] K.J. Schwerdtfeger, Heat Withdrawal in Continuous Casting of Steel, in: Making, Shaping, Treat. Steel, The AISE Steel Foundation, Pittsburgh, 2003: pp. 1–41.

[29] C. Chow, I. V Samarasekera, High speed continuous casting of steel billets Part 1 : General overview, Ironmak. Steelmak. 29 (2002) 53–60.

[30] M.C. Flemings, Solidification Processing, McGRAW-HILL, United States of America., 1974.

[31] E. Scheil, No Title, Z Met. 34 (1942) 70.

[32] W.A. Tiller, K.A. Jackson, J.W. Rutter, B. Chalmers, The redistribution of solute atoms during solidification of metals, Acta Metall. 1 (1953) 428–437.

[33] W. Jie, Solute redistribution and segregation in solidification processes, Sci. Technol. Adv. Mater. 2 (2001) 29–35.

[34] W. Kurz, D.J. Fisher, Fundamentals of Solidification, Trans Tech Publications, Lausanne, 1984.

[35] M.B. Santillana, Thermo-mechanical properties and cracking during solidification of thin slab cast steel, Universiteit Delft, 2013.

[36] W.W. Mullins, R.F. Sekerka, Morphological Stability of a Particle Growing by Diffusion or Heat Flow, J. Appl. Phys. 34 (1963) 323–329.

[37] W.W. Mullins, R.F. Sekerka, Stability of a Planar Interface During Solidification of a Dilute Binary Alloy, J. Appl. Phys. 35 (1964) 444–451.

[38] R.F. Sekerka, Morphological Stability, J. Cryst. Growth. 3,4 (1968) 71–81.

[39] L.R. Morris, W.C. Winegard, The Cell To Dendrite Transition, J. Cryst. Growth. 6 (1969) 61–66.

[40] R. Trivedi, W. Kurz, Dendritic growth, Int. Mater. Rev. 39 (1994) 49–74.

[41] G.P. Ivantsov, No Title, Dokl. Akad. Nauk SSSR. 58 (1947) 567.

[42] R.T. DeHoff, Thermodynamics in Materials Science, McGraw-Hill, Inc, New York, 1993.

[43] A.A. Shibkov, M.A. Zheltov, A.A. Korolev, A.A. Kazakov, A.A. Leonov, Effect of Surface Kinetics on the Dendritic Growth of Ice in Supercooled Water, Crystallogr. Reports. 49 (2004) 1056–1063.

[44] M. Asta, C. Beckermann, A. Karma, W. Kurz, R. Napolitano, Solidification microstructures and solid-state parallels : Recent developments , future directions, Acta Mater. 57 (2009) 941–971.

[45] V.F. De Felice, K.O. Tveito, M. Založnik, H. Combeau, M.M. Hamdi, Three-dimensional study of macro- and mesosegregation formation in a rectangular cavity cooled from one vertical side, IOP Conf. Ser. Mater. Sci. Eng. (2012).

[46] A. Suzuki, T. Suzuki, Y. Nagaoka, Y. Iwata, On Secondary Dendrite Arm Spacing in Commerical Carbon Steels with Different Carbon Content, J. Japan Inst. Met. Mater. 32 (1968) 1301–1304.

[47] W. Kurz, D.J. Fisher, Dendrite Growth At The Limit Of Stability: Tip Radius And Spacing, Acta Metall. 29 (1981) 11–20.

[48] R. Trivedi, Interdendritic Spacing: Part II. A Comparison of Theory and Experiment, Metall. Trans. A. 15A (1984) 977–982.

[49] Y. Won, B.G. Thomas, Simple Model of Microsegregation during Solidification of Steels, Metall. Mater. Trans. A. 32A (2001) 1755–1767.

[50] M. EL-Bealy, B.G. Thomas, Prediction of Dendrite Arm Spacing for Low Alloy Steel Casting Processes, Metall. Mater. Trans. B. 27B (1996) 689–692.

[51] S. Louhenkilpi, J. Miettinen, L. Holappa, Simulation of Microstructure of As-cast Steels in Continuous Casting, ISIJ Int. 46 (2006) 914–920.

[52] V. Barcellos, V. Gschwenter, H. Kytonen, C. Santos, J. Spim, S. Louhenkilpi, Miettinen, Modelling of Heat Transfer , Dendrite Microstructure and Grain Size in Continuous Casting of Steels, Steel Res. Int. 81 (2010) 461–471.

[53] T. Takahashi, I. Hagiwara, K. Ichikawa, The Washing Effect of Fluid Motion on the Segregation of the Transitional Solidification Layers in Steel Ingots, Mem. Fac. Eng. Hokkaido Univ. 13 (1973) 37–39.

[54] S.-M. Cho, B.G. Thomas, Electromagnetic Forces in Continuous Casting of Steel Slabs, Metals (Basel). 9 (2019) 1–38.

[55] K. Murakami, H. Aihara, T. Okamoto, Growth Direction Of Columnar Crystals Solidified In Flowing Melt, Acta Metall. 32 (1984) 933–939.

[56] S. Luo, W. Wang, M. Zhu, Validation and Simulation of Cellular Automaton Model for Dendritic Growth during the Solidification of Fe – C Binary Alloy with Fluid Flow, ISIJ Int. 56 (2016) 564–573.

[57] Y. Natsume, K. Ohsasa, T. Narita, Investigation of the Mechanism of Alloy Dendrite Deflection due to Flowing Melt by Phase-Field Simulation, Mater. Trans. 43 (2002) 2228–2234.

[58] S. Eckert, D. Räbiger, M. Mathes, G. Zimmermann, E. Schaberger-Zimmermann, The impact of melt flow on the grain orientation in solidifying metal alloys, IOP Conf. Ser. Mater. Sci. Eng. 27 (2011) 1–6.

[59] N. Shevchenko, O. Roshchupkina, O. Sokolova, S. Eckert, The effect of natural and forced melt convection on dendritic solidification in Ga–In alloys, J. Cryst. Growth. 417 (2015) 1–8.

[60] R. Siquieri, J. Rezende, J. Kundin, H. Emmerich, Phase-field simulation of a Fe-Mn alloy under forced flow conditions, Eur. Phys. J. Spec. Top. 177 (2009) 193–205.

[61] H. Takatani, C.-A. Gandin, M. Rappaz, EBSD Characterisation And Modelling Of Columnar Dendritic Grains Growing In The Presence Of Fluid Flow, Acta Mater. 48 (2000) 675–688.

[62] Z.-G. Xu, X.-H. Wang, M. Jiang, L.-P. Li, Investigation on formation of equiaxed zone in low carbon steel slabs, Metall. Res. Technol. 113 (2016) 106.

[63] A. Pichler, Processing of thin multiphase steel grades, Steel Res. Int. 78 (2007) 216–223.

[64] B. Wietbrock, M. Bambach, S. Seuren, G. Hirt, Homogenization strategy and material characterization of high-manganese TRIP and TWIP steels, Mater. Sci. Forum. 638–642 (2010) 3134–3139.

[65] A. Grajcar, M. Kaminska, M. Opiela, P. Skrzypczyk, B. Grzegorczyk, E. Kalinowska-Ozgowics, Segregation of alloying elements in thermomechanically rolled medium-Mn multiphase steels, J. Achiev. Mater.

Manuf. Eng. 55 (2012) 256–264.

[66] D.M. Stefanescu, Science and Engineering of Casting Solidification, 2nd ed., Springer, 2009.

[67] J. Fabricius, J.G.I. Hellström, T.S. Lundström, E. Miroshnikova, P. Wall, Darcy's Law for Flow in a Periodic Thin Porous Medium Confined Between Two Parallel Plates, Transp. Porous Media. 115 (2016) 473–493.

[68] A. Ghosh, Principles of secondary processing and casting of liquid steel, Oxford & IBH, New Delhi, 1990.

[69] M. Wu, A. Vakhrushev, G. Nummer, C. Pfeiler, A. Kharicha, A. Ludwig, Importance of Melt Flow in Solidifying Mushy Zone, Open Transp. Phenom. J. 2 (2010) 16–23.

[70] D.G. Eskin, L. Katgerman, Macrosegregation Mechanisms in Direct-Chill Casting of Aluminium Alloys, Mater. Sci. Forum. 630 (2009) 193–199.

[71] A. Ghosh, Segregation in cast products, in: Segreg. Cast Prod., 2001: pp. 5–24.

[72] E.J. Pickering, Macrosegregation in Steel Ingots: The Applicability of Modelling and Characterisation Techniques, ISIJ Int. 53 (2013) 935–949.

[73] T. Pikkarainen, V. Vuorenmaa, I. Rentola, M. Leinonen, D. Porter, Effect of superheat on macrostructure and macrosegregation in continuous cast low-alloy steel slabs, IOP Conf. Ser. Mater. Sci. Eng. 117 (2016).

[74] S.K. Choudhary, S. Ganguly, A. Sengupta, V. Sharma, Solidification morphology and segregation in continuously cast steel slab, J. Mater. Process. Technol. 243 (2017) 312–321.

[75] M.O. El-Bealy, New macrosegregation criteria for quality problems in continuous casting of steel, Ironmak. Steelmak. 40 (2013) 559–570.

[76] T.J. Piccone, T.T. Natarajan, S.R. Story, J. Bill, D.M. Hreso, Quantitative Methods for Evaluation of Centerline Segregation, Iron Steel Technol. (2016) 98–108.

[77] H. Preßlinger, S. Ilie, P. Reisinger, A. Schiefermüller, A. Pissenberger, E. Parteder, C. Bernhard, Methods for Assessment of Slab Centre Segregation as a Tool to Control Slab Continuous Casting with Soft Seduction, ISIJ Int. 46 (2006) 1845–1851.

[78] D. Zhang, Characterisation And Modelling Of Segregation in Continuously Cast Steel Slab, University of Birmingham, 2015.

[79] D.J. Heath, N. Taylor, Electron Probe Microanalysis, in: 1st ed., John Wiley & Sons Ltd, West Sussex, UK, 2015: pp. 1–34.

[80] R. Nadella, D.G. Eskin, Q. Du, L. Katgerman, Macrosegregation in direct-chill casting of aluminium alloys, Prog. Mater. Sci. 53 (2008) 421–480.

[81] H. Farivar, S. Richter, M. Hans, A. Schwedt, U. Prahl, W. Bleck, Experimental quantification of carbon gradients in martensite and its multi-scale effects in a DP steel, Mater. Sci. Eng. A. 718 (2018) 250–259.

[82] K. Miyazawa, K. Schwerdtfeger, Macrosegregation in continuously cast steel slabs – preliminary theoretical investigation on the effect of steady state bulging, Arch. Eisenhuttenwes. 52 (1981) 415–422.

[83] J.J. Moore, Review of axial segregation in continuously cast steel, Contin. Cast. (Ed), Iron Steel Soc. 3 (1984) 11–20.

[84] J.-O. Andersson, T. Helander, L. Hoglund, P. Shi, B. Sundman, THERMO-CALC & DICTRA, Computational Tools For Materials Science J-O Andersson, Thomas Helander,Lars Hdghmd, Pingfang Shi, Bo Sundman, Calphad. 26 (2002) 273–312.

[85] The OpenFOAM Foundation, (n.d.). https://openfoam.org/.

[86] A. Borgenstam, A. Engstrom, L. HogLund, J. Agren, DICTRA, a Tool for Simulation of Diffusional Transformations in Alloys, J. Phase Equilibria. 21 (2000) 269–280.

[87] Q. Dong, J. Zhang, L. Qian, Y. Yin, Numerical Modeling of Macrosegregation in Round Billet with Different Microsegregation Models, ISIJ Int. 57 (2017) 814–823.

[88] M.T. Rad, C. Beckermann, Validation of a Model for the Columnar To Equiaxed Transition With Melt Convection, in: Nastac. L, Zhang. L, Thomas. B.G., Zhu. M, Ludwig. A, Sababu. A.S., Pericleous. K, Combeau. H, CFD Model. Simul. Mater. Process. 2016, TMS (The Minerals, Metals & Materials Society), 2016: pp. 85–92.

[89] A. Vakhrushev, A. Ludwig, M. Wu, Y. Tang, G. Hackl, G. Nitzl, Coupling the turbulent flow with the solidification processes in OpenFOAM ®, in: Open

Source CFD Int. Conf., 2011: pp. 1–21.

[90] X. Cai, H. Marschall, M. Wörner, O. Deutschmann, Numerical Simulation of Wetting Phenomena with a Phase-Field Method Using OpenFOAM®, Chem. Eng. Technol. 38 (2015) 1985–1992.

[91] X. Cai, H. Marschall, M. Wörner, O. Deutschmann, A Phase Field Method with Adaptive Mesh Refinement for Numerical Simulation of 3D Wetting Processes with OpenFOAM, in: 2nd Int. Symp. Multiscale Multiph. Process Eng., 2014: pp. 116–121.

[92] B. Thomas, Modeling of continuous casting, in: Making, Shaping, Treat. Steel, The AISE Steel Foundation, Pittsburgh, 2003: pp. 1–24.

[93] B. Šarler, R. Vertnik, K. Mramor, A numerical benchmark test for continuous casting of steel, IOP Conf. Ser. Mater. Sci. Eng. 33 (2012) 1–6.

[94] J.H. Ferziger and M. Peric, Computational Methods for Fluid Dynamics, 3rd ed., Springer, Germany, 2002.

[95] ANSYS CFX, (2019). https://www.ansys.com/en-gb/products/fluids/ansys-cfx.

[96] ANSYS Fluent, (2019). https://www.ansys.com/en-gb/products/fluids/ansys-fluent.

[97] M.R. Aboutalebi, M. Hasan, R. Guthrie, Coupled turbulent flow, heat, and solute transport in continuous casting processes, Metall. Mater. Trans. B. 26B (1995) 731–744.

[98] M. Sadat, A. Gheysari, S. Sadat, The effects of casting speed on steel continuous casting process, Heat Mass Transf. 47 (2011) 1601–1609.

[99] S. Sivaramakrishnan, H. Bai, B.G. Thomas, P. Vanka, P. Dauby, M. Assar, Transient Flow Structures in Continuous Cast Steel, in: Ironmak. Conf. Proceedings, Vol. 59, Iron and Steel Society, Pittsburgh, 2000: pp. 541–557.

[100] B.G. Thomas, Continuous Casting: Modeling, in: Dantzig. J, Greenwell. A, Michalczyk. J (Eds.), Contin. Cast. Model. Encycl. Adv. Mater., Pergamon Elsevier Science Ltd., Oxford, UK, 2001: pp. 1–23.

[101] S.-M. Cho, S.-H. Kim, B.G. Thomas, Transient Fluid Flow during Steady Continuous Casting of Steel Slabs: Part I. Measurements and Modeling of Two-phase Flow, ISIJ Int. 54 (2014) 845–854.

[102] M. Rappaz, Modelling of microstructure formation in solidification processes, Int. Mater. Rev. 34 (1989) 93–124.

[103] L. Daming, L. Ruo, Z. Pingwen, A Cellular Automaton Technique for the Modeling of Solidification Microstructure in Multi-Component Alloys, First Int. Multi- Symp. Comput. Comput. Sci. IMSCCS'06. 2 (2006) 800–806.

[104] Stefanescu, Methodologies for Modeling of Solidification Microstructure and Their Capabilities, ISIJ Int. 35 (1995) 637–650.

[105] J. Ni, C. Beckermann, A Volume-Averaged Two-Phase Model for Transport Phenomena during Solidification, Metall. Trans. B. 22B (1991) 349–361.

[106] C. Prakash, Two-Phase Model For Binary Solid-Liquid Phase Change, Part I: Governing Equations, Numer. Heat Transf. Part B Fundam. An Int. J. Comput. Methodol. 18 (1990) 131–145.

[107] C.Y. Wang, C. Beckermann, A Multiphase Solute Diffusion Model for Dendritic Alloy Solidification, Metall. Trans. A. 24A (1993) 2787–2802.

[108] A. Ludwig, M. Wu, Modeling of Globular Equiaxed Solidification with a Two-Phase Approach, Metall. Mater. Trans. A Phys. Metall. Mater. Sci. 33A (2002) 3673–3683.

[109] W.D. Bennon, F.P. Incropera, A continuum model for momentum, heat and species transport in binary solid-liquid phase change systems—I. Model formulation, Int. J. Heat Mass Transf. 30 (1987) 2161–2170.

[110] M. Wu, A. Ludwig, A Three-Phase Model for Mixed Columnar-Equiaxed Solidification, Metall. Mater. Trans. 37A (2006) 1613–1631.

[111] A.M. Shahhosseini, M.N. Srinivasan, Micro-Macro Modeling Of Continuous Cast Steel To Simulate The Effect Of Casting Velocity And Pouring Temperature On Copper Segregation, in: Proc. ASME 2012 Int. Mech. Eng. Congr. Expo., 2012: pp. 1–8.

[112] Q. Dong, J. Zhang, Y. Yin, B. Wang, Three-Dimensional Numerical Modeling of Macrosegregation in Continuously Cast Billets, Metals (Basel). 7 (2017).

[113] H. Yang, L. Zhao, X. Zhang, K. Deng, L.I. Wencai, Y. Gan, Mathematical simulation on coupled flow, heat, and solute transport in slab continuous casting process, Metall. Mater. Trans. B. 29 (1998) 1345–1356.

[114] R.J.A. Janssen, G.C.J. Bart, M.C.M. Cornelissen, J.M. Rabenberg,

Macrosegregation in continuously cast steel billets and blooms, Appl. Sci. Res. 52 (1994) 21–35.

[115] M. Long, D. Chen, Study on mitigating center macro-segregation during steel continuous casting process, Steel Res. Int. 82 (2011) 847–856.

[116] S.K. Choudhary, S. Ganguly, Morphology and Segregation in Continuously Cast High Carbon Steel Billets, ISIJ Int. 47 (2007) 1759–1766.

[117] T. Rec, A. Milenin, Numerical Modeling Of Macrosegregation And Stress-Strain State Distribution In Slab During Continue Casting With Soft Reduction, Arch. Metall. Mater. 55 (2010) 915–919.

[118] R. Pardeshi, A.K. Singh, V.R. Voller, P. Dutta, A Dual Scale Model for Macrosegregation in Alloy Solidification, Numer. Heat Transf. Part A. 59 (2011) 934–953.

[119] M. Rady, E. Arquis, A dual-scale coupled micro / macro segregation model for dendritic alloy solidification, Heat Mass Transf. 42 (2006) 1129–1141.

[120] V.R. Voller, C. Prakash, A fixed grid numerical modelling methodology for convection-diffusion mushy region phase-change problems, Int. J. Heat Mass Transf. 30 (1987) 1709–1719.

[121] Y.A. Meng, B.G. Thomas, Heat-Transfer and Solidification Model of Continuous Slab Casting : CON1D, Metall. Mater. Trans. A. 34B (2003) 685–705.

[122] M. Rappaz, C.A. Gandin, Stochastic Modeling of Grain Structure Formation in Solidification Processes, MRS Bull. 19 (1994) 20–24.

[123] L.-Q. Chen, Phase-Field Models for Microstructure Evolution, Annu. Rev. Mater. Res. 32 (2002) 113–140.

[124] H.K.D.H Bhadeshia, Lecture 3: Solidification, n.d.

[125] C. Karrasch, Solidification Kinetics In Undercooled Pure Iron And Iron - Boron Alloys Under Different Fluid Flow, Ruhr-University Bochum, 2016.

[126] R.S. Qin, H.K.D.H. Bhadeshia, Phase field method, Mater. Sci. Technol. 26 (2010) 803–811.

[127] J.W. Cahn, J.E. Hilliard, Free Energy of a Nonuniform System. I. Interfacial Free Energy, J. Chem. Phys. 28 (1958) 258–267.

[128] D. Lee, J. Huh, D. Jeong, J. Shin, A. Yun, J. Kim, Physical , mathematical , and numerical derivations of the Cahn – Hilliard equation, Comput. Mater. Sci. 81 (2014) 216–225.

[129] J.W. Cahn, A Microscopic Theory For Domain Wall Motion And Its Experimental Verification In Fe-Al Alloy Domain Growth Kinetics, J. Phys. Symp. 38 (1977) 51–54.

[130] S. Allen, J.W. Cahn, A Microscopic Theory for Antiphase Boundary Motion and Its Application To Antiphase Domain Coarsening, Acta Metall. 27 (1979) 1085–1095.

[131] S.L. Wang, R.F. Sekerka, A.A. Wheeler, B.T. Murray, S.R. Coriell, R.J. Braun, G.B. McFadden, Thermodynamically-consistent phase-field models for solidification, Phys. D. 69 (1993) 189–200.

[132] J.Y. Choi, Phase-field investigation on the non-equilibrium interface dynamics of rapid alloy solidification, Iowa State University Ames, 2011.

[133] R. Kobayashi, Modeling and numerical simulations of dendritic crystal growth, Phys. D. 63 (1993) 410–423.

[134] S.G. Kim, W.T. Kim, T. Suzuki, Phase-field model for binary alloys, Phys. Rev. E. 60 (1999) 7186–7197.

[135] S.G. Kim, W.T. Kim, J.S. Lee, M. Ode, T. Suzuki, Large Scale Simulation of Dendritic Growth in Pure Undercooled Melt by Phase-field Model, ISIJ Int. 39 (1999) 335–340.

[136] T. Suzuki, M. Ode, S.G. Kim, W.T. Kim, Phase-field model of dendritic growth, J. Cryst. Growth. 237–239 (2002) 125–131.

[137] J.A. Warren, W.J. Boettinger, Prediction of Dendritic Growth and Microsegregation Patterns in a Binary Alloy using the Phase-Field Method, Acta Metall. Mater. 43 (1995) 689–703.

[138] C. Beckermann, H.J. Diepers, I. Steinbach, A. Karma, X. Tong, Modeling Melt Convection in Phase-Field Simulations of Solidification, J. Comput. Phys. 154 (1999) 468–496.

[139] M. Ode, S.G. Kim, W.T. Kim, T. Suzuki, Numerical Prediction of the Secondary Dendrite Arm Spacing Using a Phase-field Model., ISIJ Int. 41 (2001) 345–349.

[140] M. Ode, T. Suzuki, Numerical Simulation of Initial Microstructure Evolution of Fe-C Alloys Using a Phase-field Model, ISIJ Int. 42 (2002) 368–374.

[141] M. Ode, T. Suzuki, S.G. Kim, W.T. Kim, Phase-field model for solidification of Fe–C alloys, Sci. Technol. Adv. Mater. 1 (2000) 43–49.

[142] M. Ode, J.S. Lee, S.G. Kim, W.T. Kim, T. Suzuki, Phase-field Model for Solidification of Ternary Alloys, ISIJ Int. 40 (2000) 870–876.

[143] A.F. Ferreira, L.D.O. Ferreira, Microsegregation in Fe-C-P Ternary Alloys Using a Phase-Field Model, J. Braz. Soc. Mech. Sci. Eng. XXXI (2009) 173–180.

[144] A.F. Ferreira, A.J. Da Silva, J.A. De Castro, Simulation of the Solidification of Pure Nickel Via the Phase-field Method, Mater. Res. 9 (2006) 349–356.

[145] M. Ode, S.G. Kim, T. Suzuki, Recent Advances in the Phase-field Model for Solidification, ISIJ Int. 41 (2001) 1076–1082.

[146] Y. Sun, Y. Wu, X. Lu, R. Li, J. Xiao, Anisotropy and roughness of the solid-liquid interface of BCC Fe, J. Mol. Model. 21:32 (2015) 1–11.

[147] J. Debierre, A. Karma, F. Celestini, R. Guerin, Phase-field approach for faceted solidification, Phys. Rev. E. 68 (2003) 1–13.

[148] A.F. Ferreira, I.L. Ferreira, J.P. da Cunha, I.M. Salvino, Simulation of the Microstructural Evolution of Pure Material and Alloys in an Undercooled Melts via Phase-field Method and Adaptive Computational Domain, Mater. Res. 18 (2015) 644–653.

[149] L. Du, R. Zhang, L. Zhang, Phase-field simulation of dendritic growth in a forced liquid metal flow coupling with boundary heat flux, Sci. China Technol. Sci. 56 (2013) 2586–2593.

[150] M. Zhu, T. Dai, S. Lee, C. Hong, Modeling of dendritic growth in the presence of convection, Sci. China Ser. E Eng. Mater. Sci. 48 (2005) 241–257.

[151] K. Oguchi, T. Suzuki, Three-dimensional Phase-field Simulation of Free Dendrite Growth of Iron, ISIJ Int. 47 (2007) 277–281.

[152] B.F. Torrence, The Student's Introduction to Mathematica and the Wolfram Language, Cambridge University Press, 2019.

[153] William J.Palm III, Introduction to Matlab for Engineers, 3rd ed., McGraw-

Hill, 2011.

[154] G.F. Vander Voort, Metallography Principles and Practice, McGraw-Hill, New York, 1999.

[155] S. Béchet, L. Beaujard, New reagent for the micrographic detection of the austenitic grain of tempered or quenched-tempered steels, Rev. Métallurgie. 52 (1955) 830–836.

[156] S. Richter, J. Mayer, Sample Preparation for EPMA, 10th Reg. Work. Electron Probe Microanal. Today-Practical Asp. (2012) 121–147.

[157] G.S. Cole, The structure of ingot castings, Can. Metall. Q. 8 (1969) 189–218.

[158] W. Lu, Z.Y. Shen, Y. Yang, Y.H. Zhang, C.J. Song, Q.J. Zhai, Structure Evolution of Fe-Mn Based Alloys under a Near-Rapid Solidification Process, Adv. Mater. Res. 1015 (2014) 3–9.

[159] W. Lu, Y. Yang, K. Xie, C. Song, Q. Zhai, Evolution of the Structure Morphology of Fe-5 wt.%Mn Alloy During Directional Solidification, in: TMS2014 Annu. Meet. Suppl. Proc., 2014: pp. 1015–1022.

[160] C.L.M. Alves, J. Rezende, D. Senk, J. Kundin, Peritectic phase transformation in the Fe-Mn and Fe-C system utilizing simulations with phase-field method, J. Mater. Res. Technol. 8 (2019) 233–242.

[161] L. Arnberg, R.H. Mathiesen, The Real-Time, High-Resolution X ray Video Microscopy of Solidification in Aluminium Alloys, JOM. (2007) 20–26.

[162] K. Miłkowska-Piszczek, M. Dziarmagowski, A. Buczek, J. Pióro, The methods of calculating the solidifying strand shell thickness in a continuous casting machine, Arch. Mater. Sci. Eng. 57 (2012) 75–79.

[163] Y. Meng, B.G. Thomas, Heat-Transfer and Solidification Model of Continuous Slab Casting: CON1D, Metall. Mater. Trans. B. 34B (2003) 685–705.

[164] D. Wu, S. Cheng, Z. Cheng, Characteristics of shell thickness in a slab continuous casting mold, Int. J. Miner. Metall. Mater. 16 (2009) 25–31.

[165] M. Long, Z. Dong, D. Chen, Q. Liao, Y. Ma, Effect of uneven solidification on the quality of continuous casting slab, Int. J. Mater. Prod. Technol. 47 (2013) 216–232.

[166] M.O. El-Bealy, On the Formation of Interdendritic Internal Cracks During

Dendritic Solidification of Continuously Cast Steel Slabs, Metall. Mater. Trans. B. 43 (2012) 1488–1516.

[167] S. Kholmatov, Application of the Ruler-type EMBr on the IJmuiden CC22 caster : a CFD study, 2011.

[168] R. Chaudhary, B.G. Thomas, S.P. Vanka, Effect of Electromagnetic Ruler Braking (EMBr) on Transient Turbulent Flow in Continuous Slab Casting using Large Eddy Simulations, Metall. Mater. Trans. B. 43B (2012) 532–553.

[169] X. Zhang, W. Chen, L. Zhang, A coupled model on fluid flow, heat transfer and solidification in continuous casting mold, Model. Cast. Solidif. Process. - MCSP2017. 14 (2017) 416–420.

[170] K. Jin, S.P. Vanka, B.G. Thomas, Large Eddy Simulations of Electromagnetic Braking Effects on Argon Bubble Transport and Capture in a Steel Continuous Casting Mold, Metall. Mater. Trans. B. 49B (2018) 1360–1377.

[171] L. Xu, E. Wang, C. Karcher, A. Deng, X. Xu, Numerical Simulation of the Effects of Horizontal and Vertical EMBr on Jet Flow and Mold Level Fluctuation in Continuous Casting, Metall. Mater. Trans. B. 49 (2018) 2779–2793.

[172] C.J. Xu, X.J. Zhang, J. Li, Z.Y. Wang, L.W. Zhang, Analysis Of The Effects Of An Electromagnetic Brake (EMBR) On Flow Behaviors In The Large Slab Continuous Casting Mold, METALURGIJA. 55 (2016) 317–320.

[173] R. Liu, B.G. Thomas, J. Sengupta, S.D. Chung, M. Trinh, Measurements of Molten Steel Surface Velocity and Effect of Stopper-rod Movement on Transient Multiphase Fluid Flow in Continuous Casting, ISIJ Int. 54 (2014) 2314–2323.

[174] T. Zhang, J. Yang, P. Jiang, Measurement of Molten Steel Velocity near the Surface and Modeling for Transient Fluid Flow in the Continuous Casting Mold, Metals (Basel). 9 (2019) 1–15.

[175] B.G. Thomas, L.J. Mika, F.M. Najjar, Simulation of fluid flow inside a continuous slab-casting machine, Metall. Trans. B. 21 (1990) 387–400.

[176] K. Cukierski, B.G. Thomas, Flow control with local electromagnetic braking in continuous casting of steel slabs, Metall. Mater. Trans. B. 39 (2008) 94–107.

[177] D.E. Hershey, B.G. Thomas, F.M. Najjar, Turbulent Flow Through Bifurcated

Nozzles, Int. J. Numer. Methods Fluids. 17 (1993) 23–47.

[178] H. Mehrara, B. Santillana, D.G. Eskin, B. R, K. L, A. G, Modeling of primary dendrite arm spacing variations in thin-slab casting of low carbon and low alloy steels, IOP Conf. Ser. Mater. Sci. Eng. 27 (2011) 1–7.

[179] M. Long, L. Zhang, F. Lu, A Simple Model to Calculate Dendrite Growth Rate during Steel Continuous Casting Process, ISIJ Int. 50 (2010) 1792–1796.

[180] M.K. Singh, G. Abbel, Flow Patterns OSF2 - CFD results & Plant Data, 2013.

[181] I. Salvino, L.D.O. Ferreira, A.F. Ferreira, Simulation of Microsegregation in Multicomponent Alloys During Solidification, Steel Res. Int. 83 (2012) 1–10.

[182] J.H. Jeong, N. Goldenfeld, J.A. Dantzig, Phase field model for three-dimensional dendritic growth with fluid flow, Phys. Rev. E. 64 (2001) 1–14.

[183] Y. Lu, C. Beckermann, J.. Ramirez, Three-dimensional phase-field simulations of the effect of convection on free dendritic growth, J. Cryst. Growth. 280 (2005) 320–334.

APPENDIX-A

Figure A.1: Dendritic solidification structure at the centre of step_2 for Fe-5.8 wt.% Mn alloy.

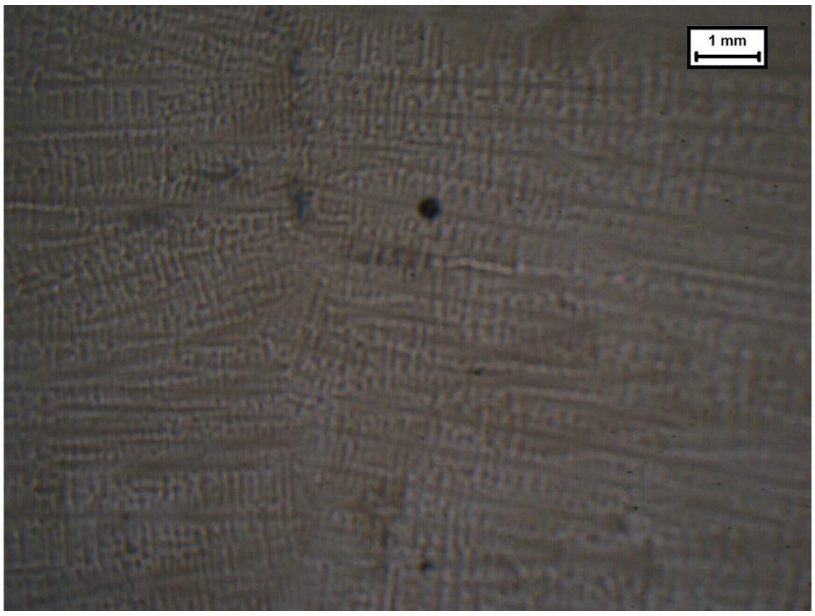

Figure A.2: Dendritic solidification structure at the centre of step_5 for Fe-5.8 wt.% Mn alloy.

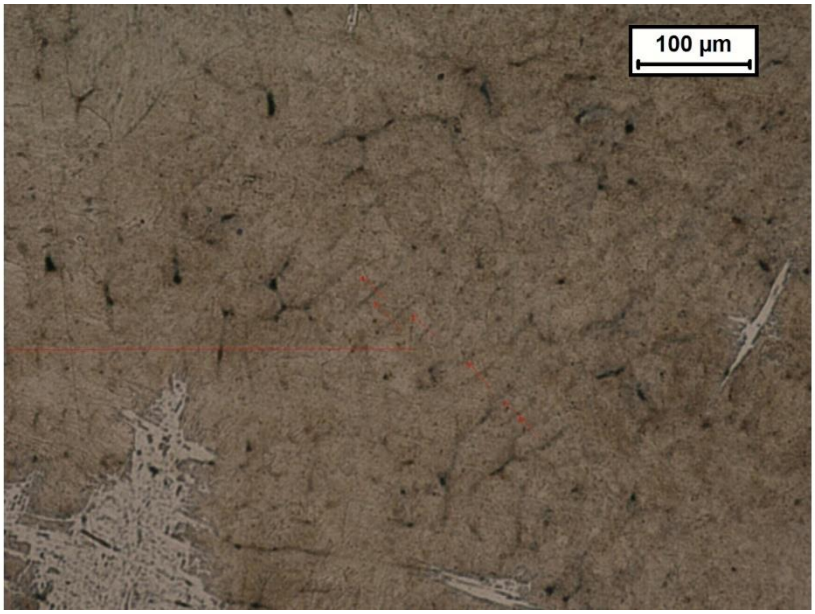

Figure A.3: Solidification structure for step_1 of the ternary alloy Fe-0.149 wt.% C-0.995 wt.% Mn.

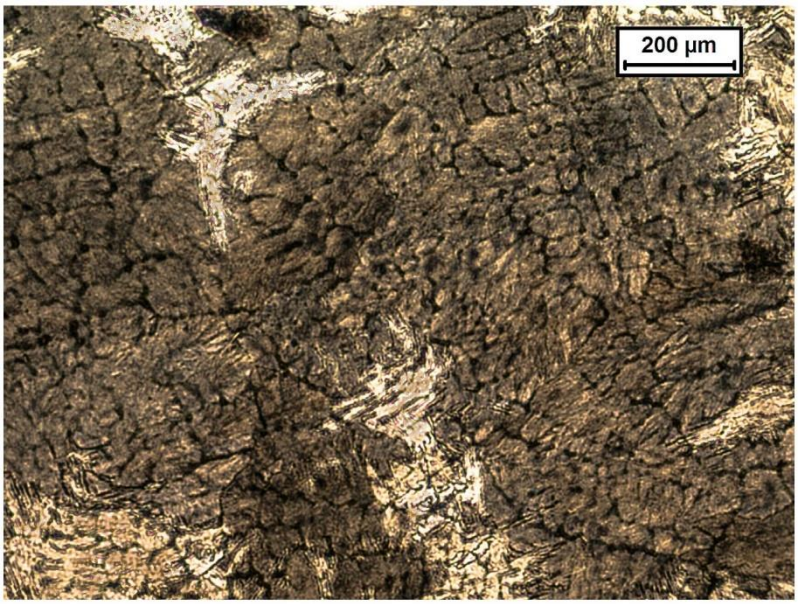

Figure A.4: Solidification structure for step_2 of the ternary alloy Fe-0.149 wt.% C-0.995 wt.% Mn.

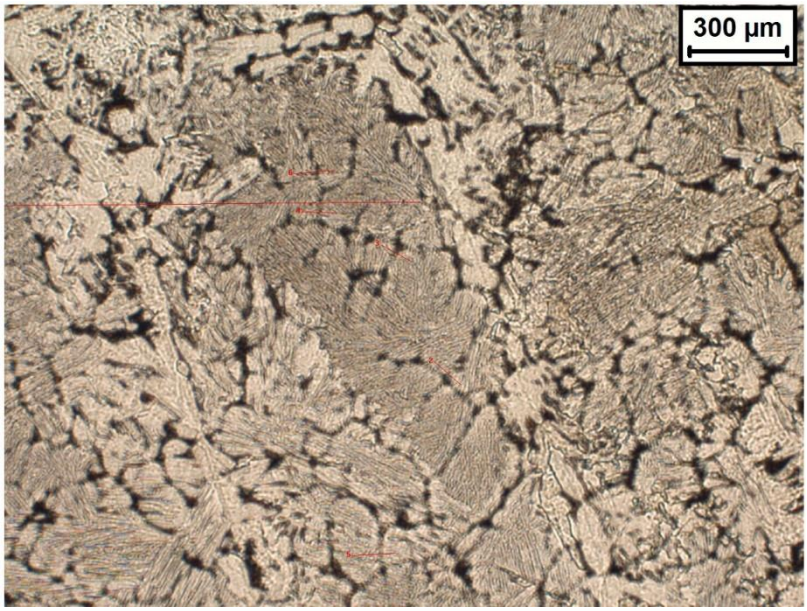

Figure A.5: Solidification structure for step_2 of the ternary alloy Fe-0.149 wt.% C-0.995 wt.% Mn.

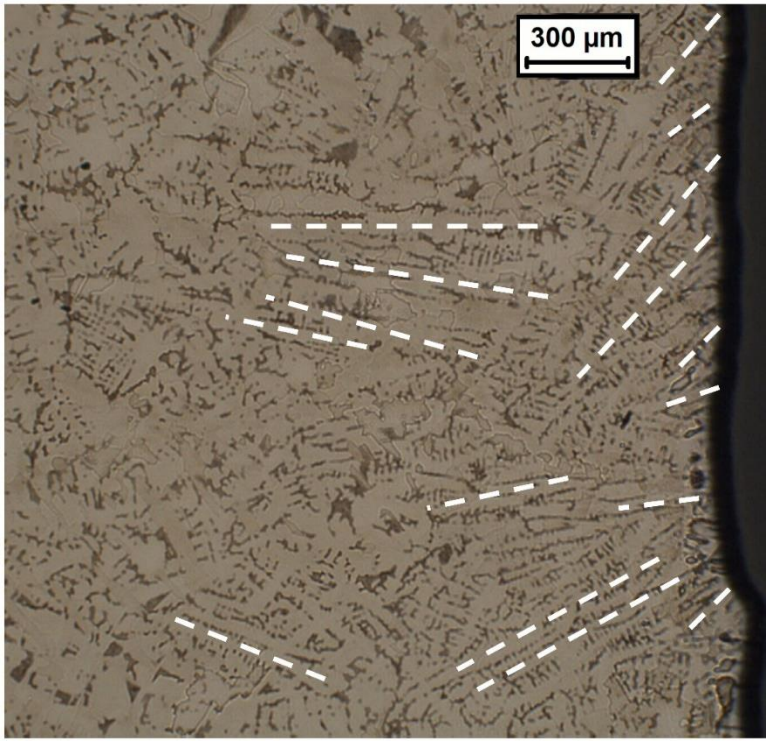

Figure A.6: Variation in dendrite growth direction away from the slab surface for sample D.